INTEGRABLE POINT VORTEX MOTION ON A SPHERE

by

Rangachari Kidambi

A Dissertation Presented to the

FACULTY OF THE GRADUATE SCHOOL

UNIVERSITY OF SOUTHERN CALIFORNIA

In Partial Fulfillment of the

Requirements for the Degree

DOCTOR OF PHILOSOPHY

(Aerospace Engineering)

May 1999

UMI Number: 9933677

UMI
300 North Zeeb Road
Ann Arbor, MI 48103

UNIVERSITY OF SOUTHERN CALIFORNIA
THE GRADUATE SCHOOL
UNIVERSITY PARK
LOS ANGELES, CALIFORNIA 90007

This dissertation, written by

RANGACHARI KIDAMBI

under the direction of his Dissertation Committee, and approved by all its members, has been presented to and accepted by The Graduate School, in partial fulfillment of requirements for the degree of

DOCTOR OF PHILOSOPHY

Dean of Graduate Studies

Date April 23, 1999

DISSERTATION COMMITTEE

Paul K. Newton
Chairperson

Eugene Gutkin

Eckart Meiburg

Fred Browand

Acknowledgements

- Paul Newton, advisor and friend. For giving me a good problem to work on and for giving me the freedom to work on it as I liked. I thank him for a pleasant Ph.D. experience.
- Larry Redekopp, Fred Browand, Eckart Meiburg and Eugene Gutkin for agreeing to serve on my committees.
- Dennis Plocher for helping out with various spock and printer related problems.
- Marrietta Penoliar for drawing some of the figures and drawing them well.
- The Graduate and Engineering Schools for a fellowship and the Department of Aerospace Engineering for a teaching assistantship.
- Peiji Chen for advice on software related problems.
- Sudhir for his cheerful presence, Shashi for a lot of things going back a long way and Nitin for his help at all times and also for giving me an opportunity to open my mind to new things.

Contents

List Of Figures

Abstract

This dissertation is concerned with integrable point vortex motion on a sphere. First, we solve the equations governing the relative motion of three point vortices of arbitrary strength moving on the surface of a sphere of radius R. The system is more general than the corresponding one in the plane [5, 9, 10, 43, 73, 87, 88, 98, 101] and reduces to it in the limit $R \to \infty$, as long as the three vortices remain sufficiently close to each other during the course of their motion. We use cartesian coordinates in which the vector $\vec{x}_i$ points from the center of the sphere to the vortex with strength Γ_i. An important conserved quantity is the center of vorticity vector, $\vec{c} = (\sum \Gamma_i \vec{x}_i)/(\sum \Gamma_i)$, which, with no loss of generality, we align with the z-axis. Based on the size of this vector relative to the radius of the sphere, we classify the motion into one of five types: super-radial, radial, sub-radial, degenerate, or a limiting super-radial case. This categorization allows us to draw several conclusions about the qualitative motion of the vortices.We then fully characterize all fixed and relative equilibria on the sphere. For fixed equilibria, the vortices must lie on great circles (geodesics). If the strengths are equal, they form an equilateral triangle. Otherwise, the triangle shape is specified once the strength of the vortices is given. The relative equilibria are classified as either degenerate ($\vec{c} = 0$) or non-degenerate ($\vec{c} \neq 0$). For each type, the shape of the vortex triangle is described and the frequency of rotation is computed. As in the planar problem, it is possible to introduce trilinear coordinates and study the motion in a phase plane, which allows us to locate all the equilibria, as well as to characterize more complex relative dynamics.

We then describe self-similar vortex collapse on the sphere, stating necessary and sufficient conditions for collapse to occur, computing the collapse times and vortex trajectories on the route towards collapse. Collapse trajectories occur in pairs, called 'partner states', which have two distinct collapse times $\tau^- < \tau^+$. The collapse time that is achieved for a given configuration depends on the sign of the parallelpiped volume formed by the vortex position vectors, hence depends on whether the vortices $(\Gamma_1, \Gamma_2, \Gamma_3)$ are arranged in a right-handed or left-handed sense. From a given collapsing configuration, one can obtain the partner state by reversing the signs of the Γ_i's, or alternatively by using a discrete symmetry associated with the initial configuration that leaves all relative distances unchanged, but reverses the sign of the parallelpiped volume. In the plane, there is only one collapse time associated with a given configuration — the partner state is one that expands self-similarly [5].

The instantaneous streamline patterns that can occur are then considered. After stating some general results based on the spherical topology. we categorize all possible instantaneous streamline patterns and describe their stagnation point structure for the cases of two and three vortices. For the case of two vortices, the only non-degenerate patterns that can arise are a figure eight (lemniscate) or a limacon, which are homotopically equivalent. For the case of three vortices, there are 12 topologically distinct primitives. from which an additional 23 patterns can be produced via continuous deformations on the sphere (homotopies). All possible streamline patterns that arise from three vortex motion can be obtained via linear superposition of the primitives and their homotopic equivalents. In this sense. the primitives can be viewed as the 'building blocks' for the general instantaneous flow topology. The equations of motion and streamline patterns in the stereographic plane are obtained using the projected equations of motion in Hamiltonian form. We describe streamline patterns for three vortex fixed equilibria and relative equilibria as seen in both a fixed and a rotating frame of reference. Dynamical bifurcations of the streamline patterns are studied for a collapsing and special periodic solution. although to generally understand this problem would require more extensive computation. We conclude with a discussion of the relevance of the three vortex topological classification scheme and the bifurcation of streamline topologies for understanding global atmospheric weather patterns (spherical isobars) and large scale mixing phenomena.

Finally. we examine vortex motion on the sphere with solid boundaries. This problem is more relevant to oceanographic flows than atmospheric ones. where the boundaries model the effect of coastlines and shores. For highly symmetric domains. we show that known solutions in the plane. obtained by the method of images. can be used to generate solutions on the sphere by stereographic projection. We explicitly compute the particle and vortex motion for several domains on the sphere. including a spherical cap, a longitudinal wedge, channel and rectangle.

Chapter 1

Introduction

A variety of coherent vortical structures are observed in the Earth's atmosphere and oceans [93]. These range from tropical cyclones and the winter polar vortex in the atmosphere, to eddies and rings in the large scale ocean circulation. A striking feature of these vortices is their relative persistence in the presence of adverse effects like vorticity gradients, dissipation and wave dispersion, a prime example being the raging storm on Jupiter - the 'Great Red Spot', now visible for more than 300 years [59].

Coherent structures are a characteristic feature of quasi-geostrophic and two dimensional turbulence. In the last 20 years they have been generated and extensively studied in the laboratory and in analytical and numerical simulations. Flierl [33] showed theoretically the instability of geostrophic vortices and the appearance of dipolar and tripolar structures. McWilliams [63] showed that an initially random vorticity field generates monopoles and dipoles over time. Legras *et al* [57] found a tripolar vortex arising in an evolving two dimensional flow. The importance of such vortex triples and their emergence in physical systems has also been documented in [17] and [26]. These structures have also been studied experimentally by van Heijst *et al* [102], Kloosterziel and van Heijst [53] and Hopfinger *et al* [46]. Another aspect that has received extensive attention is the interaction of these structures especially the merger of vortices, supposed to be key to understanding the dynamics of QG and 2 - D turbulence [30, 41, 78].

It is not only of intrinsic interest to understand the dynamics of these structures, but also of importance in environmental engineering applications. This is because, in general, these structures move around transporting momentum, heat, biota and pollutants. The strong localised quality and persistence of these structures has naturally led to their being modeled mainly as solitons [62] or vortices. It is with the latter model that we will be concerned in this study. In particular, a large number of analytical and numerical studies have focused on understanding the genesis and motion of tropical cyclones [2, 4, 20, 38, 50, 91]. A result of these studies is that the basic mechanism behind the familiar northwestward (southwestward) movement of cyclonic (anticyclonic) vortices is essentially nonlinear and inviscid (Hopfinger and van Heijst [47]). The study of these structures in oceanography is more recent and dates back to the MODE programme

(1978) [65]. Of course, the emergence and evolution of such structures has been much studied in the context of 2 - D turbulence. However, most of these are not directly applicable to the geophysical case, as they deal with plane geometries and don't consider rotation and stratification effects.

1.1 Literature Survey

Let us first consider the classical 2 - D hydrodynamic problem on the sphere i.e given an initial vorticity distribution $\omega(\theta, \phi, 0)$, find a stream-function ψ such that $\Delta\psi = -\omega(\theta, \phi, t)$. The vorticity is advectively conserved, according to Kelvin's Theorem [89]:

$$\frac{D\omega}{Dt} = 0. \tag{1.1}$$

Since we are interested in modeling eddies, $\omega(\theta, \varphi, 0)$ can be considered to be made of two parts - ω_e representing the vorticity of the eddy and ω_b representing the background or ambient vorticity. A common, though not the only, choice for ω_b is the planetary vorticity, $f = 2\ \Omega\ \cos\theta$ where Ω is the Earth's angular velocity and θ the co-latitude. Similarly, ω_e can be modeled in a variety of ways - by point vortices, by singular (but not point vortices) and by nonsingular vortices. In every case, the equation to be solved is (1.1): the models differ only in the choice of initial conditions. Thus, we have a range of possibilities :

1. $\omega_e = \sum_{i=1}^{N} \Gamma_i \delta(\phi_i - \phi)\delta(\theta_i - \theta)$, $\omega_b = -\sum_{i=1}^{N} \Gamma_i / 4\pi R^2$. The problem being studied is point vortex motion on a stationary sphere. ψ is the familiar logarithmic function of the distance from the vortex [14]. This is the class of problems we will be studying.

2. $\omega_e = \sum_{i=1}^{N} \Gamma_i \delta(\phi_i - \phi)\delta(\theta_i - \theta)$, $\omega_b(0) = 2\Omega\cos\theta$. This problem is of finding the point vortex motion on a sphere which is in solid body rotation. This is more complicated than the previous case. A more detailed description will be given below.

3. $\omega_e = 0$, $\omega_b(0) \neq 0$. Polvani and Dritschel [82] use this model, but in their case ω_b does not correspond to the Earth's rotation. Thus, solutions are obtained for $\Delta\ \psi = -\omega$ where ω is piecewise constant, being $\omega_b = \omega_N$, north of some latitude θ_0 and $\omega_b = \omega_S$ to the south. The northern vortex patch is supposed to model the wintertime polar vortex and the patch configuration produces a zonal flow peaking at θ_0 rather than the traditional solid body rotation. Stability of the interfacial Rossby waves is one of the concerns of this study and the results are applied to explain the ribbon like features in Saturn's atmosphere.

4. $\omega_e = \omega_s$, $\omega_b(0) = 0$. ω_s is a singular vorticity distribution, but not due to a point vortex. The singular vorticity distribution generates a background vorticity field for $t > 0$ unlike in the point vortex case . Thus, in this case, $\omega_b \neq 0$ for $t > 0$. We are not aware of any studies with such a model.

5. $\omega_e = \omega_{ns}$, $\omega_b \neq 0$. The vortices have a nonsingular vorticity distribution ω_{ns}, i.e. they are actually vortex patches. The governing equations for interacting patches of constant vorticity on a stationary sphere are derived in [52]. Some numerical studies on such patches are reported in [26, 27, 28, 29].

The full equations governing fluid motions on a rotating planet are quite complicated and a variety of approximate equations have been used. One such set of equations, for homogeneous, inviscid flows, are the shallow water equations from which we can derive the conservation of potential vorticity (PV):

$$\frac{D}{Dt}\left(\frac{\omega + f}{H}\right) = 0 \tag{1.2}$$

(1.2) is the starting point for most analyses of vortex motion on rotating planets. ω is the radial component of the relative vorticity, f the local planetary or ambient vorticity and H the fluid depth. One can readily see the effects of geometry, rotation, stratification and topology in the problem, from (1.2). Thus, the spherical geometry enters through ω and f, the rotation through f and the stratification, topographic and surface effects through H. In contrast, in traditional 2-D vortex dynamics, $f = 0$ and $H =$ constant. (1.2) holds in the stratified case also, but with H having the interpretation of a height over which there is an arbitrary but constant density difference, $\Delta\rho$ ($H = -\Delta\rho\ \frac{\partial z}{\partial \rho}$) [21].

To isolate the various effects, a variety of studies have been made in which one or the other term has been neglected or accounted for, in an approximate manner. We look at a few of these below -

1. The well-known geostrophic flow, with attendant vertical rigidity of fluid columns, is recovered in the Ro $<<$ 1 limit ($\omega << f$ which is assumed constant). Here, the Rossby number, Ro $= U/\Omega L$ where U and L are typical velocity and length scales in the problem.

2. If surface waves and bottom topography are not allowed, we have $H =$ const. and the equation describes 2-D motions of a thin spherical layer of fluid in the rigid cap approximation. This is similar to the situation described by (1.1) except that , in this case, ω_b is not a function of time. This model has been used by Klaytskin and Reznik [54] to obtain a point vortex solution on a rotating sphere such that the vortices translate along circles of latitude with constant velocity U. The main results of this study are that eastward and westward travelling vortices generate fundamentally different velocity fields. ψ in this case is a first order Legendre function.

3. A much studied form is the quasi - geostrophic PV equation. Many different versions of the equation have been used among which are the non - divergent and divergent barotropic

models (on the sphere and on the β - plane), n - layer baroclinic models and other models considering the effect of topography on eddy propagation. We look at a few of these below.

(a) Non - divergent QG on the β - plane (also known as the rigid lid approximation) :

All the studies surveyed till now, studied the problem on a spherical geometry. However most of the geophysical literature does not deal with spherical geometry. Instead, the dynamics is studied on the β- plane, which is the simplest possible dynamical model of the sphericity of the Earth's surface. The equation that has been studied the most in this context is the non - divergent quasi-geostrophic equation

$$\frac{\partial \Delta \psi}{\partial t} + J(\psi, \Delta \psi) + \beta \frac{\partial \psi}{\partial x} = 0 \tag{1.3}$$

i. Bjerknes and Holmboe [13] were among the earliest to study vortex motion on a β - plane in the context of low Rossby number flows i.e they were looking at the linearised version of (1.3). They predicted westward motion. Flierl [34] showed that the westward motion occurs at a speed that is dependent on the scale of motion and hence the vortex disintegrates.

ii. For non - negligible Rossby number, (1.3) has been studied by Rossby [86] and Adem [2]. They predict that an isolated cyclonic vortex would drift in a north-westward direction.

iii. Recent studies using this model include Chan and Williams [20], Korotaev and Fedotov [55], Reznik and Dewar [85] and Smith and Ulrich [94]. Initial vortex streamfunctions range from algebraic to algebraic - exponential (this simulates a hurricane profile) and algebraic - Gaussian. Many of these studies are concerned with the motion of tropical cyclones.

iv. The effect of topography in the rigid lid approximation is examined by Carnevale *et al* [19] and Grimshaw *et al* [42] . In the first work, the effect of bottom topography on modon propagation is studied. The modon, which is a dipole, is modelled by two point vortices. In the second, the authors examine the evolution of an eddy placed on a topographic slope on an f plane.

(b) Divergent QG equation :

In this approximation, surface effects are allowed and the potential vorticity is given by

$$PV = \Delta \psi - \frac{\psi}{R_d^2} + f \tag{1.4}$$

where R_d is the radius of deformation. The second term describes the stretching of vortex lines, an effect not possible in the strictly 2 - D divergent model.

i. (1.4) is used by Tribbia [100] and Verkley [103] to study modon propagation on a sphere. Modons are exact solutions originally found by Stern [96] on the β - plane. The modon streamfunction has a dipolar shape, is confined within a circle and vanishes outside. More recently, Neven has studied modon propagation on a sphere in a variety of contexts - modons in shear flow [69], baroclinic modons [70] and quadrupole modons [71]. Though, in these studies, the β - plane approximation is not made, the authors look for modon solutions which just propagate along a latitude and are not free to move around on the entire sphere.

ii. There is a large literature using (1.4) on the β - plane. Zabusky and McWilliams [106] use a modulated point vortex model where the circulation around each point vortex can change with time. Morikawa and Swenson [67] studied the stability of a ring of vortices on an f - plane ($\beta = 0$). Friedlander [38] has extended their analysis to the β - plane and investigates the stability of a ring of cyclones and anti - cyclones. In all cases, the vortex streamfunctions are modified Bessel functions of the second kind. Such vortices are known as geostrophic vortices.

iii. Reznik [84], Sutyrin [97], Nycander and Sutyrin [76] and Shapiro and Ooyama [92] use this model to study cyclone motion on a β - plane. In [84], ψ is written as the sum of a regular (ψ_r) and a singular part ψ_s which is made up of the streamfunctions of all the vortices, each being proportional to the modified Bessel function. Results are obtained for the motion of a high intensity vortex (one whose strength greatly exceeds the local planetary vorticity) and the results are used to explain the northwestward motion of a cyclone.

iv. The generation and evolution of the dipolar modon on a β - plane has been the subject of many studies. An extensive review of these solutions and their applicability to modeling eddies in geophysical flows can be found in [35]. More recently, modon dynamics has been studied on the γ - plane which takes quadratic corrections to f into account [72].

(c) Stratified models :

A variety of studies have been made in the stratified case also. Prominent among these are those using n - layer models, where the density is constant in each layer. Each layer has a different streamfunction and the PV is conserved for each layer. Some two layer studies are by Gryanik [44], Hogg and Stommel [48], Yano and Flierl [104], Davey *et al* [23] and Young [105]. In particular, [105] is a very interesting study of the interaction of a small number of baroclinic vortices. Finally, Shapiro [91] has used a three layer model to study hurricane evolution on the β - plane. Point vortex motion in a two layer model on the sphere is currently being studied by Jamaloodeen and Newton [49].

There is one final point worth mentioning, before we go on to consider point vortex models. (1.2) indicates that the β - effect (expressed in $f = f_0 + \beta y$) and the topographic effect (expressed by H) have similar dynamical consequences [47]. This dynamical similarity has been exploited by a number of investigators [18. 32. 61] to study vortex motion on a β - plane in the laboratory. Since. in a lab, f = const.. the topography is varied instead. to simulate the β - effect. The experiments confirm the general tendency of northwestward (southwestward) drift of cyclonic (anticyclonic) vortices.

1.2 Point Vortices

With this brief background, we now consider the role of point vortex models in these problems. A point vortex can be visualised as a vortex line in an infinitesimal thin layer of fluid so that the only component of vorticity is normal to the flow plane.This idea can be extended to the case when the fluid motion is on a differentiable manifold. Again, the point vortex is pictured as a vortex line in an infinitesimal layer of fluid covering the manifold so that the only component of vorticity is along the local normal. Studies of point vortex motions on manifolds. and especially compact surfaces like a sphere, are interesting for the following reasons :

1. They generalise the planar motions. Indeed. one would expect these motions on manifolds to approach those in the plane whenever the vortices are close to being in a tangent plane.

2. New qualitative features of the motion, which were absent in the planar case, may emerge due to the presence of inherent length scales in the geometry of the surface.

3. As mentioned earlier, there exist a variety of intense vortical structures in the earth's atmosphere and oceans. Such eddies have been modeled as point vortices by Bogomolov [16]. The point vortex model is useful in understanding what role the spherical geometry plays in the motion of these eddies. One is no longer confined to latitudinal neighborhoods, which is the case in the β - plane approximation.

In the case of a stationary sphere, all the vorticity is concentrated at points and instead of an infinite number of degrees of freedom, we have only a finite number. $\frac{D\omega}{Dt} = 0$ is automatic since the vortices move with the local fluid velocity and the background vorticity is a constant. Thus, the problem is reduced to finding a stream function which satisfies

$$\Delta\psi = -\sum_{i=1}^{N} \Gamma_i \delta(\phi_i - \phi)\delta(\theta_i - \theta) + \frac{\sum_{i=1}^{N} \Gamma_i}{4\pi R^2}$$

where Δ is the Laplace - Beltrami operator on the sphere. The background vorticity ω_b is in general a non-zero constant because the Stokes' Theorem stipulates that $\int \omega dA = 0$ for all possible ω distributions on a compact closed surface, and in particular on a sphere.

The set of ODEs governing the motion of the vortices on a sphere was first given by Bogomolov [14, 15]. [14] also contains an analysis of the motion of three identical point vortices on the sphere, hence generalises the planar results in Novikov [73]. Hally [45] derived the equations of motion on an arbitrary manifold. He also examined the stability of vortex streets on a sphere. Kimura and Okamoto [52] described the equations governing the motion of vortex patches on a sphere. The papers by Polvani and Dritschel [82] and DiBattista and Polvani [25] although not primarily focused on point vortices, do contain sections which describe aspects of point vortex motion. In particular, in [82], the equations are given in vector form, the form that leads to much simplicity in analysis and one that we use a lot in our work. In [25], point vortex and finite area vortex pairs on a rotating sphere are studied in an effort to model atmospheric blocking phenomena.

The case of point vortex motion on a rotating sphere is rather complicated. We now have a varying background vorticity field which interacts with the vortices, affects their trajectories and is itself affected by them. Thus, the motion of the vortices cannot be described by a system of ODEs but instead one must now solve in addition, partial differential (for the motion of the continuous background vorticity field) and integro-differential (for the stream function ψ) equations. Bogomolov [16] obtained a 1-term solution for the motion of a single vortex on a rotating sphere and it was seen to exhibit the familiar northwestward (southwestward) motion characteristic of cyclones (anticyclones). Various point vortex studies on the β - plane were refered to earlier. However there are few studies investigating point vortex motion on the entire sphere.

On the other hand, independent of any geophysical considerations, point vortex models have been studied and used in a variety of contexts for more than 125 years. It was known to Kirchhoff that the point vortex equations form a Hamiltonian system; Poincare showed that the motion of three vortices in the unbounded plane was integrable. However, ideas from non-linear dynamical systems have been applied to these systems extensively only in the last 20 years. Motivated mostly by advances in dynamical systems and computational techniques, the focus has by and large been on the dynamics of point vortices in the plane [5, 6, 8, 9, 10, 31, 43, 73, 74, 75, 77, 87, 88, 98, 101], both integrable [5, 9, 10, 31, 43, 73, 75, 77, 87, 88, 98, 101] and non-integrable [6, 8, 74] configurations.

Point vortices are attractive for modeling eddies because the conservation of vorticity is automatic, making them more amenable to mathematical analysis. However, the model is not very useful if one is interested in how the eddies form and deform, how they affect and are affected by wave motions and how they interact with other eddies. Experiments have shown that cyclonic and anticyclonic vortices (generated in the lab) behave very differently as do vortices with differing core vorticity distributions like the sink vortex and the stirring vortex (these have different net angular momenta). The point vortex model does not make any distinctions between all these cases. Finite sized vortices can support waves on their cores: point vortices, having no structure. are incapable of these. Finally. point vortices interact very differently than distributed vortices - two isolated point vortices can never touch but two patches can.

Our general goal in this work is to study the effects of spherical geometry on the motion of point vortices.In general, of course. both the curvature of the sphere as well as its rotation will influence the dynamics. However. in this work we ignore the effects of rotation and thus focus exclusively on how the spherical geometry influences the vortex motion. The motion of N point vortices on a stationary sphere for N = 1,2 is fairly simple. A single vortex doesn't move: two vortex motion is summarised in Appendix I. The motion of three vortices, though more complex, is still integrable and hence we can study the dynamics analytically. This is the content of Chapter 2. The work therein generalises that in Aref [5], Gröbli [43] and Synge [98] and thus is of more geophysical significance. In Chapter 3, we describe the mechanism of finite time collapse of three vortices, in particular the phenomenon of partner states. Chapter 4 deals with streamline topologies in point vortex flows on a sphere. In the last chapter, we consider point vortex motion in bounded domains on a sphere: explicit solutions are provided for some special domains using the image method. Appendix II contains some of the Mathematica and Fortran programs that were used to draw some of the figures in this work. Finally, there is by now a very extensive and complete literature on the three vortex problem in the plane [5, 6, 8, 9, 10, 43, 73, 74, 75, 77, 87, 88, 98, 101] and whenever possible, we make connections to this literature at the appropriate times. In some sense, parts of this work can be viewed as a generalization of [5, 7, 43, 73, 98] to the sphere.

Chapter 2

Motion of three vortices

In this chapter, we study the motion of three vortices on a sphere. It will be shown that this is the most general integrable point vortex motion. Three vortex interaction is the simplest case in which the inter-vortical distances can vary with time. Hence, understanding the relative motion of three vortices is the key to understanding the relative motions of a larger number of vortices.

This chapter is organized as follows. We first write the general equations of motion for N-vortices on a sphere of radius R, both in cartesian and spherical coordinates. We emphasize the Hamiltonian structure of the equations, the conserved quantities and Poisson bracket structure. The most important conserved quantity is the center of vorticity vector $\mathbf{c} = \mathbf{M}/\sigma$, where $\mathbf{M} = \sum_{i=1}^{N} \Gamma_i \mathbf{x}_i$ is the moment of vorticity and $\sigma = \sum \Gamma_i$ is the total vorticity. In §2.2 we re-formulate the equations in a more geometric way by writing the equations that govern the length of the three sides of the triangle formed by connecting the vortices with chords through the sphere. This formulation allows us to classify all motions into one of five states which we call: super-radial, sub-radial, radial, degenerate, and limiting super-radial. In the plane, this classification is not possible because there is no inherent length scale analogous to the radius of the sphere. In §2.3 we study all equilibrium configurations, separating the discussion into the fixed equilibrium states and the relative equilibrium states. In §2.4 we use trilinear coordinates introduced in [5, 98] for the planar problem to reduce the general motion to level curves in a phase plane. This allows us to describe more general motions of the three vortices. In §2.5 we describe a special periodic solution where we can work out the details of the absolute motion. The special case in which the vortices collapse in finite time is studied in Chapter 3. For those interested in a quick survey of the main results, we have organized them in a series of propositions. Proposition 2.1 covers the fixed equilibria, while proposition 2.2 describes all relative equilibria. Proposition 2.3 locates all the equilibria in the phase plane.

2.1 Equations of Motion

Written in vector form, the system of 3N equations governing the motion of N vortices on the surface of a sphere of radius R is given by, [82]:

$$\dot{\mathbf{x}}_\mathbf{i} = \frac{1}{4\pi R}\sum_{j\neq i}^{N}\frac{\Gamma_j(\mathbf{x_j}\times\mathbf{x_i})}{(R^2-\mathbf{x_i}\cdot\mathbf{x_j})} \tag{2.1}$$

$\mathbf{x_i} = (x_i, y_i, z_i)$ represents the vector from the center of the sphere to the ith vortex, with strength Γ_i. The denominator can be more compactly written as $(R^2 - \mathbf{x_i}\cdot\mathbf{x_j}) \equiv \frac{l_{ij}^2}{2}$ where $l_{ij} = |\mathbf{x_i} - \mathbf{x_j}|$ is the chord distance between the two vortices. Since the vortices are constrained to lie on the surface of a sphere of radius R, it is clear that the above formulation has a redundancy in it, as the constraint:

$$\begin{aligned} I &= \sum\Gamma_\alpha|\mathbf{x}_\alpha|^2 \\ &= R^2\sum\Gamma_\alpha = const. \end{aligned}$$

has not been used.

Although the cartesian representation of the equations makes the analysis more transparent, one can also write the equations in spherical coordinates, which has distinct advantages in understanding the general structure of the problem. The equation for the ith vortex is given by, [15, 52]:

$$\dot{\theta}_i = -\frac{1}{4\pi R^2}\sum_{j\neq i}^{N}\frac{\Gamma_j\sin(\theta_j)\sin(\phi_i-\phi_j)}{1-\cos(\gamma_{ij})} \tag{2.2}$$

$$\sin(\theta_i)\dot{\phi}_i = \frac{1}{4\pi R^2}\sum_{j\neq i}^{N}\frac{\Gamma_j(\sin(\theta_i)\cos(\theta_j)-\cos(\theta_i)\sin(\theta_j)\cos(\phi_i-\phi_j))}{1-\cos(\gamma_{ij})} \tag{2.3}$$

where $\cos(\gamma_{ij}) \equiv \cos(\theta_i)\cos(\theta_j) + \sin(\theta_i)\sin(\theta_j)\cos(\phi_i - \phi_j)$. Note that the denominator $R^2(1 - \cos(\gamma_{ij})) = l_{ij}^2/2$. Figure 2.1(a) shows the angles locating the ith vortex. Because the constraint that the vortices lie on the surface of the sphere of radius R has been explicitly used in this formulation, the system has been reduced to 2N equations. One advantage of this formulation is that the equations can be written in Hamiltonian form. The Hamiltonian is given by:

$$H = \frac{1}{4\pi R^2}\sum_{i<j}\Gamma_i\Gamma_j\ln(l_{ij}^2) \tag{2.4}$$

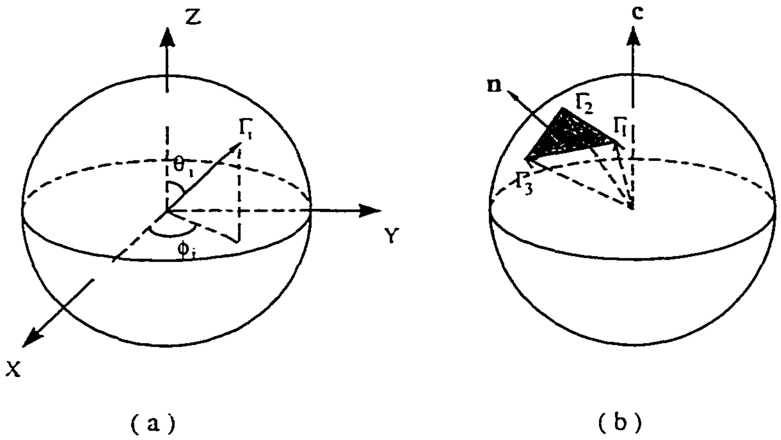

Figure 2.1: (a) Location of point vortex Γ_i in spherical coordinates. (b) Geometry of the 3 vortex problem.

One can then introduce the conjugate variables $P_i \equiv \sqrt{|\Gamma_i|}\cos(\theta_i)$ and $Q_i \equiv \sqrt{|\Gamma_i|}\phi_i$ which puts the system in standard Hamiltonian form:

$$\begin{aligned} \dot{P}_i &= \frac{\partial H}{\partial Q_i} \\ \dot{Q}_i &= -\frac{\partial H}{\partial P_i} \end{aligned}$$

By introducing the Poisson bracket:

$$[f,g] = \sum_i^N \frac{1}{\Gamma_i}\left(\frac{\partial f}{\partial\cos(\theta_i)}\frac{\partial g}{\partial\phi_i} - \frac{\partial f}{\partial\phi_i}\frac{\partial g}{\partial\cos(\theta_i)}\right)$$

we can write the equations more compactly:

$$\begin{aligned} \frac{\partial\cos(\theta_i)}{\partial t} &= [\cos(\theta_i), H] \\ \frac{\partial\phi_i}{\partial t} &= [\phi_i, H] \end{aligned}$$

It can then be easily verified that, in addition to the Hamiltonian, one has the following conserved quantities:

$$\begin{aligned} Q &= \frac{1}{R}\sum_{i=1}^N \Gamma_i x_i \equiv \sum_{i=1}^N \Gamma_i \sin(\theta_i)\cos(\phi_i) \\ P &= \frac{1}{R}\sum_{i=1}^N \Gamma_i y_i \equiv \sum_{i=1}^N \Gamma_i \sin(\theta_i)\sin(\phi_i) \end{aligned}$$

$$S = \frac{1}{R}\sum_{i=1}^{N}\Gamma_i z_i \equiv \sum_{i=1}^{N}\Gamma_i \cos(\theta_i)$$

There are three integrals in involution:

$$\begin{aligned} [H, P^2 + Q^2] &= 0 \\ [H, S] &= 0 \\ [P^2 + Q^2, S] &= 0 \end{aligned}$$

making the three vortex problem on the sphere (as in the plane [5, 6, 43, 73, 98]) integrable. It follows from the conservation of Q,P and S that the center of vorticity vector:

$$\mathbf{c} = \mathbf{M}/\sigma \tag{2.5}$$

is also a conserved quantity which will be important for understanding the relative dynamics in the three vortex problem. Because of the symmetries inherent in the problem (as long as the sphere is non-rotating), it is always possible to orient the axes so that the vector c is aligned with the z axis, hence its intersection with the sphere is the North Pole. This will be our convention throughout this chapter.

There is one further point worth making concerning the *four* vortex problem. It is straightforward to show that:

$$\begin{aligned} [P, Q] &= S \\ [Q, S] &= P \\ [S, P] &= Q \end{aligned}$$

In addition, we also have that $[H, P] = 0$ and $[H, Q] = 0$. Therefore, if we choose the values $(Q, P, S) = (0, 0, 0)$, then we have 4 integrals in involution, namely (H, Q, P, S). The condition that all three quantities are zero is equivalent to requiring that the center of vorticity vector $\mathbf{c} = 0$. Hence, if we restrict ourselves to the case where the center of vorticity is zero, the four vortex problem is integrable. This special degenerate case of the four vortex problem on the sphere is analogous to the planar case considered in [31]. In that case, the condition for integrability is also $\mathbf{c} = 0$. However, as shown in [31], it follows that $\sum_{i=1}^{4}\Gamma_i = 0$, a condition not required on the sphere.

As a final comment, notice that the equations for the vortex motion in the plane can be written in vector form as:

$$\dot{\mathbf{X}}_i = \sum_{j\neq i}^{N} \frac{(\Gamma_j/2\pi)\hat{e}_z \times (\mathbf{X_i} - \mathbf{X_j})}{l_{ij}^2}$$

where $\mathbf{X_i} = \hat{e}_x x_i + \hat{e}_y y_i$ is the vector locating the i vortex (for example, see [89]). On the sphere, we can rewrite (2.1) as:

$$\dot{\mathbf{x}}_i = \sum_{j \neq i}^{N} \frac{(\Gamma_j/2\pi)(\mathbf{x_j}/R) \times (\mathbf{x_i} - \mathbf{x_j})}{l_{ij}^2}$$

which directly mimics the planar equations (and the Biot-Savart law [89]), since the vector $\mathbf{x_j}$ $/R$ is the unit normal on the sphere located at the vortex with strength Γ_j. This formulation carries over in a straightforward way to general curved surfaces by replacing $\mathbf{x_i}$ $/R$ with $\hat{n}_j$, the unit normal located at vortex Γ_j.

2.2 Geometrical Formulation

The equations for the relative dynamics of the vortices can be easily derived from the original system (2.1):

$$\frac{d({l_{12}}^2)}{dt} = \frac{\Gamma_3 V}{\pi R}[\frac{1}{l_{23}^2} - \frac{1}{l_{31}^2}] \tag{2.6}$$

$$\frac{d({l_{23}}^2)}{dt} = \frac{\Gamma_1 V}{\pi R}[\frac{1}{l_{31}^2} - \frac{1}{l_{12}^2}] \tag{2.7}$$

$$\frac{d({l_{31}}^2)}{dt} = \frac{\Gamma_2 V}{\pi R}[\frac{1}{l_{12}^2} - \frac{1}{l_{23}^2}] \tag{2.8}$$

V is the volume of the parallelopiped formed by the vectors $\mathbf{x_1}$, $\mathbf{x_2}$,$\mathbf{x_3}$, i.e.

$$V = \mathbf{x_1} \cdot (\mathbf{x_2} \times \mathbf{x_3})$$

Notice that the sign of V can be positive or negative depending on whether the vectors form a right or left handed coordinate system. In [5, 98], this is taken care of by introducing σ_{ijk} which indicates the orientation of the triangle spanned by the three vortices. For us, it is more useful to allow the quantity V to take on both positive or negative values. If $V = 0$, the three vortices lie on a great circle. In fact, a similar system of equations can be derived for the separations in the N-vortex problem and is given by

$$\frac{d({l_{ij}}^2)}{dt} = \frac{1}{\pi R} \sum_{k=1}^{N}{}'' \Gamma_k V_{ijk}[\frac{1}{l_{jk}^2} - \frac{1}{l_{ki}^2}]$$

where the $''$ means the summation excludes k = i and k = j.

Other geometric quantities that are useful in visualizing and understanding the relative motion of the three vortices are the area $A(t)$ of the plane triangle formed by the three vortices and the normal vector $\mathbf{n}$ pointing from the center of the sphere through the plane spanned by the three vortices:

$$\begin{aligned} \mathbf{n} &= (\mathbf{x_1} - \mathbf{x_2}) \times (\mathbf{x_2} - \mathbf{x_3}) \\ &= \mathbf{x_1} \times \mathbf{x_2} + \mathbf{x_2} \times \mathbf{x_3} + \mathbf{x_3} \times \mathbf{x_1} \end{aligned}$$

Some of these quantities are shown in figure 2.1(b). The equations for $A(t), V(t)$ in terms of l_{ij} are:

$$A \equiv \pm\frac{1}{4}(2l_{12}^2l_{23}^2 + 2l_{23}^2l_{31}^2 + 2l_{31}^2l_{12}^2 - l_{12}^4 - l_{23}^4 - l_{31}^4)^{1/2} \tag{2.9}$$

$$V \equiv \pm\frac{1}{2}(16R^2A^2 - l_{12}^2l_{23}^2l_{31}^2)^{1/2} \tag{2.10}$$

The volume V can also be written in terms of A, R, and $\bar{a}$, where $\bar{a}$ is the radius of the circle in which the vortex triangle is inscribed:

$$\begin{aligned} V &= \pm 2A\sqrt{R^2 - \bar{a}^2} \\ &= \pm 2AR\sqrt{1 - \frac{\bar{a}^2}{R^2}} \end{aligned}$$

Again, in all these cases, the $\pm$ sign depends on the orientation of the vortices. In the limiting case where $\bar{a}/R$ is small, it is easy to see that the leading term is given by $V \sim 2AR$, in which case our equations agree with the planar equations studied by Aref and Synge [5, 98].Hence when $\bar{a}/R$ is small, we expect the motion to correspond to the planar motion. This means that the closer the vortices are to a great circle, the more the dynamics should differ from the planar case.

Two useful alternative ways of writing the volume V are:

$$\mathbf{c} \cdot \mathbf{n} = V = \mathbf{x_i} \cdot \mathbf{n}$$

Then a simple constraint on the spherical flow is given by:

$$(\mathbf{c} - \mathbf{x_i}) \cdot \mathbf{n} = 0$$

which says that the vector $(\mathbf{c} - \mathbf{x_i})$ must lie in the plane of the triangle. This constraint forms the basis of a useful classification scheme that we describe in §2.2.2.

Equations (2.6) - (2.8) have the 2 invariants:

$$C_1 = \sum_{i<j} \Gamma_i \Gamma_j l_{ij}^2 \tag{2.11}$$

$$C_2' = \frac{1}{4\pi R^2}\sum_{i<j}\Gamma_i\Gamma_j \ln(l_{ij}^2)$$

The second quantity can more usefully be written as:

$$C_2 = \exp(\frac{4\pi R^2 C_2'}{\Gamma_1\Gamma_2\Gamma_3}) = (l_{12}^2)^{1/\Gamma_3}(l_{23}^2)^{1/\Gamma_1}(l_{31}^2)^{1/\Gamma_2} \tag{2.12}$$

Other useful formulas are given by:

$$\begin{aligned}
||\mathbf{c}||^2 &= R^2 - C_1/\sigma^2 \\
||\mathbf{n}|| &= 2A \\
\mathbf{c}\cdot\dot{\mathbf{n}} &= \dot{V} \\
\dot{A} &= \frac{V}{16\pi RA}\sum\frac{l_{ij}{}^2 - l_{jk}{}^2}{l_{ki}{}^2}(\Gamma_i + \Gamma_k) \\
\dot{V} &= \frac{1}{8\pi}[2R\sum\frac{l_{ij}{}^2 - l_{jk}{}^2}{l_{ki}{}^2}(\Gamma_i + \Gamma_k) - \frac{1}{R}\sum l_{ij}^2(\Gamma_i - \Gamma_j)] \\
\dot{\mathbf{n}} &= \frac{1}{4\pi R}\sum[\frac{\Gamma_i + \Gamma_j}{l_{ij}^2} - \frac{\Gamma_i + \Gamma_k}{l_{ki}^2}]l_{jk}^2\mathbf{x}_i
\end{aligned}$$

In the last three identities, the summation is made over cyclic permutations of i, j, k from 1 to 3, where $i \neq j \neq k$. Finally, another important quantity governing the vortex motion is the harmonic mean of the vortex strengths, $h = \frac{1}{3}\sum\frac{1}{\Gamma_i}$. The geometric mean $g = (\Gamma_1\Gamma_2\Gamma_3)^{\frac{1}{3}}$, although not as important, also appears in some equations.

2.2.1 Symmetries

The structure of the equations of motion give rise to the following discrete symmetries:

1. **If $\Gamma_1, \Gamma_2, ..., \Gamma_n; \mathbf{x}_1, \mathbf{x}_2, ..., \mathbf{x}_n$ satisfies the equations of motion, then so does $-\Gamma_1, -\Gamma_2, ..., -\Gamma_n; -\mathbf{x}_1, -\mathbf{x}_2, ..., -\mathbf{x}_n$.**

2. **If $\Gamma_1, \Gamma_2, ..., \Gamma_n; \mathbf{x}_1, \mathbf{x}_2, ..., \mathbf{x}_n; t$ satisfies the equations of motion, then so does $-\Gamma_1, -\Gamma_2, ..., -\Gamma_n; \mathbf{x}_1, \mathbf{x}_2, ..., \mathbf{x}_n; -t$.**

3. **If $\Gamma_1, \Gamma_2, ..., \Gamma_n; \mathbf{x}_1, \mathbf{x}_2, ..., \mathbf{x}_n; t$ satisfies the equations of motion, then so does $\Gamma_1, \Gamma_2, ..., \Gamma_n; -\mathbf{x}_1, -\mathbf{x}_2, ..., -\mathbf{x}_n; -t$.**

4. **The equations (2.1) are invariant with respect to cyclic or anti-cyclic permutations of all indices.**

By making use of these symmetries it will be sufficient to consider only the two cases: $\Gamma_1, \Gamma_2, \Gamma_3 > 0$; $\Gamma_1, \Gamma_2 > 0, \Gamma_3 < 0$. The invariance of (2.1) to cyclic and anti-cyclic permutations is easily verified. Cyclically permuting the indices corresponds to exchanging the positions of the vortices but respecting the right hand rule. Anti-cyclically permuting the indices corresponds to exchanging the positions of the vortices in such a way as to change to the left hand rule. Although this permutation does not affect the system (2.1), it does have the important effect on (2.6)-(2.8) of changing V to $-V$.This change is important and will be described in more detail in Chapter 3 when we analyse the collapsing states.

2.2.2 Geometric classification scheme.

As a first step towards classifying all motions on the sphere, we make use of the fact that $\mathbf{c}$ is a conserved quantity and that $(\mathbf{c} - \mathbf{x}_i)$ must always lie in the plane spanned by the three vortices. There are then 5 distinct families of motions, based on the relative size of $||\mathbf{c}||$ as compared to the radius of the sphere.

1. **Super-radial states:**$||\mathbf{c}|| > R$.

   For this case, shown in figure 2.2, the tip of the vector $\mathbf{c}$, (labeled c^*) lies outside the sphere. Since the vector $\mathbf{c}$ is conserved, the point c^* remains fixed in the plane P spanned by the three vortices. At any fixed time, the vortices must lie on a curve which is a slice of the sphere by the plane P. The plane can, of course, twist and tilt, but always passes through the point c^*. Shown in figure 2.2(b) are the family of curves achieved by tilting P downwards without twisting it. From these figures, we can conclude:

   (i) No fixed latitude states are possible.

   (ii) The only great circle states are the family where $\mathbf{c}$ lies in P, hence $\mathbf{c}$ and $\mathbf{n}$ are perpendicular.

   (iii) No collapse is possible.

   (iv) Because $C_1 < 0$ these states are only possible if $\Gamma_1, \Gamma_2 > 0, \Gamma_3 < 0$.

2. **Sub-radial states:** $||\mathbf{c}|| < R$.

   For this case, shown in figure 2.3, the point c^* lies inside the sphere. The plane P slices the sphere on curves shown in figure 2.3(b). From this, we can conclude:

   (i) Only one fixed latitude state is possible, where $\mathbf{c}$ is parallel to $\mathbf{n}$, hence $\mathbf{c}$ is perpendicular to the plane P. This fixed latitudinal state gives the smallest radius $\bar{a}$.

   (ii) The only great circle states are the family where $\mathbf{c}$ lies in P, hence $\mathbf{c}$ and $\mathbf{n}$ are perpendicular.

   (iii) No collapse is possible.

3. **Radial states:** $||\mathbf{c}|| = R$.

   This case is shown in figure 2.4. The point c^* lies on the sphere, and the slices of the sphere

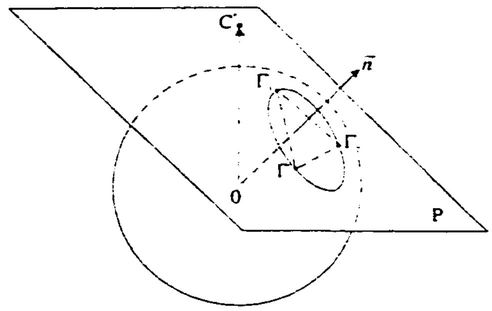

(a)

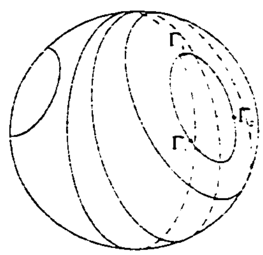

(b)

Figure 2.2: Super-radial states : (a) c^* lies outside the sphere. (b) family of intersections of P with the sphere as the plane swings down.

are shown in figure 2.4(b). From these. we conclude that:

(i) No fixed latitudinal states are possible.

(ii) The only great circle states are the family where $\mathbf{c}$ lies in P, hence $\mathbf{c}$ and $\mathbf{n}$ are perpendicular.

(iii) Collapse is possible only at the point c^* (i.e. the North Pole).

(iv) These states are possible only if $C_1 = 0$

4. **Degenerate states:** $||\mathbf{c}|| = 0$.

This case is the most symmetric and is shown in figure 2.5. The plane P must pass through the center of the sphere, which means the vortices must lie on the curves shown in figure 2.5(b). From this, we can conclude:

(i) No fixed latitudinal states are possible.

(ii) All states are great circle states, hence $\bar{a} = R$.

(iii) No collapse is possible.

(iv) $C_1 = \sigma^2 R^2$ for this case.

5. **Limiting super-radial states: $||\mathbf{c}|| = \infty$**

   This final case is a limiting case of the super-radial states where $c^* = \infty$. For this to hold, we must have $\sigma = 0$. The plane P cuts the sphere as shown in figure 2.6 so that $\mathbf{M}$ is perpendicular to $\mathbf{n}$. We can conclude that:

   (i) No fixed latitudinal states are possible. All states must lie on so called 'vertical latitudes' shown in figure 2.6(b).

   (ii) Great circle states are only possible if $\mathbf{M}$ lies in P.

   (iii) No collapse is possible.

The dynamics associated with these five states are described in the remainder of the chapter.

2.3 Equilibria

We define equilibria as vortex motions in which the inter-vortical distances stay fixed. Fixed equilibria are given by the fixed points of the system (2.1) whereas relative equilibria are given by the fixed points of the system (2.6)-(2.8). We will refer to cases where $\mathbf{c} = 0$ as 'degenerate', and where $\mathbf{c} \neq 0$ as 'non-degenerate'.

2.3.1 Fixed Equilibria

We start the section by summarizing all possible fixed equilibrium states for three vortices on the sphere.

Proposition 2.1 (Fixed Equilibria). *1. A necessary and sufficient condition for fixed equilibria is $\sum_{i=1}^{3} \Gamma_i(\Gamma_j + \Gamma_k)\mathbf{x}_i = 0$, $i \neq j \neq k$, which implies that all fixed equilibrium states lie on great circles.*

2. If $\Gamma_1 = \Gamma_2 = \Gamma_3$, then the fixed equilibria form equilateral triangles and are degenerate great circle states.

3. If the vortex strengths are not all equal, then the fixed equilibria are non-degenerate great circle states with positions and strengths that satisfy the condition:

$$\Gamma_1 \tan(\alpha_1) = \Gamma_2 \tan(\alpha_2) = \Gamma_3 \tan(\alpha_3)$$

The normal vector $\mathbf{n}$ is perpendicular to $\mathbf{c}$. If $\Gamma_1, \Gamma_2, \Gamma_3 > 0$, the triangle is acute. If $\Gamma_1, \Gamma_2 > 0, \Gamma_3 < 0$, the triangle is obtuse.

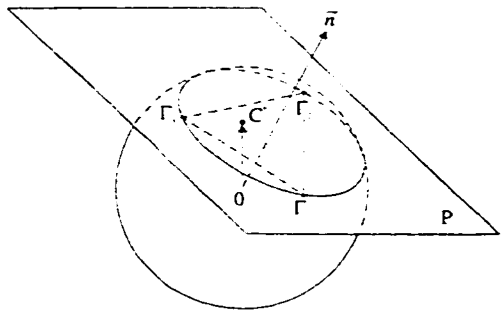

(a)

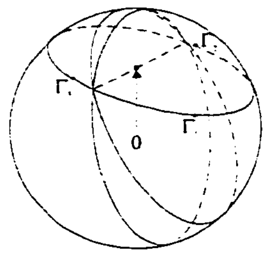

(b)

Figure 2.3: Sub-radial states : (a) c^* lies inside the sphere. (b) family of intersections of P with the sphere as the plane swings down.

To prove necessity in part (1), we start by setting time derivatives in (2.1) to zero:

$$\sum_{j=1}^{3}{}' \frac{\Gamma_j(\mathbf{x_j} \times \mathbf{x_i})}{(R^2 - \mathbf{x_i} \cdot \mathbf{x_j})} = 0.$$

Then take the cross product with $\Gamma_i \mathbf{x_i}$:

$$\Gamma_i \mathbf{x_i} \times \sum_{j \neq i}^{3} \frac{\Gamma_j(\mathbf{x_j} \times \mathbf{x_i})}{(R^2 - \mathbf{x_i} \cdot \mathbf{x_j})} = 0$$

Next, use the following manipulations:

$$\begin{aligned} \mathbf{x_i} \times (\mathbf{x_j} \times \mathbf{x_i}) &= (\mathbf{x_i} \cdot \mathbf{x_i})\mathbf{x_j} - (\mathbf{x_i} \cdot \mathbf{x_j})\mathbf{x_i} \\ &= \|\mathbf{x_i}\|^2 \mathbf{x_j} - (\mathbf{x_i} \cdot \mathbf{x_j})\mathbf{x_i} \\ &= R^2 \mathbf{x_j} - (\mathbf{x_i} \cdot \mathbf{x_j})\mathbf{x_i} \end{aligned}$$

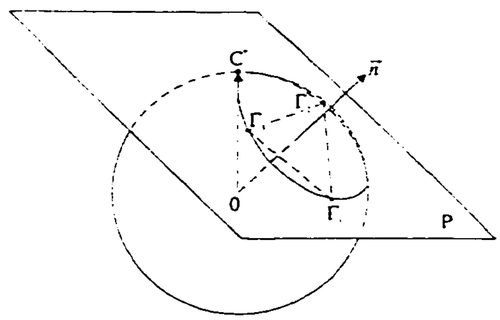

(a)

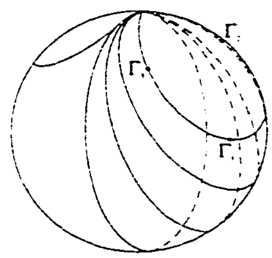

(b)

Figure 2.4: Radial states : (a) c^* lies on the sphere. (b) family of intersections of P with the sphere as the plane swings down.

and sum over i to get:

$$\sum_{i<j} \Gamma_i \Gamma_j (\mathbf{x_i} + \mathbf{x_j}) = 0$$
$$\Rightarrow$$
$$\sum_1^3 \Gamma_i \mathbf{x_i} (\sigma - \Gamma_i) = 0$$
$$\Rightarrow$$
$$M\sigma = \sum_1^3 \Gamma_i^2 \mathbf{x_i}$$

from which the condition in part (1) follows. To see that this condition is also sufficient, assume that it holds. Then:

$$\sum_{i=1}^3 \Gamma_i \mathbf{x_i} (\sigma - \Gamma_i) = 0$$
$$\Rightarrow \Gamma_1(\Gamma_2 + \Gamma_3)\mathbf{x_1} + \Gamma_2(\Gamma_3 + \Gamma_1)\mathbf{x_2} + \Gamma_3(\Gamma_1 + \Gamma_2)\mathbf{x_3} = 0 \tag{2.13}$$

Taking the dot product $\mathbf{x_i}$ with (2.13) for $i = 1, 2, 3$ gives:

$$\begin{aligned}\Gamma_2(\Gamma_3+\Gamma_1)l_{12}^2 + \Gamma_3(\Gamma_1+\Gamma_2)l_{31}^2 &= \Gamma_1(\Gamma_2+\Gamma_3)l_{12}^2 + \Gamma_3(\Gamma_1+\Gamma_2)l_{23}^2 \\ &= \Gamma_1(\Gamma_2+\Gamma_3)l_{31}^2 + \Gamma_2(\Gamma_1+\Gamma_3)l_{23}^2 \\ &= 2R^2[\Gamma_1(\Gamma_2+\Gamma_3)+\Gamma_2(\Gamma_1+\Gamma_3)+\Gamma_3(\Gamma_1+\Gamma_2)]\end{aligned}$$

After some manipulations, this yields:

$$\begin{aligned}(\Gamma_1+\Gamma_2)l_{31}^2 &= (\Gamma_1+\Gamma_3)l_{12}^2 \\ (\Gamma_2+\Gamma_3)l_{12}^2 &= (\Gamma_1+\Gamma_2)l_{23}^2\end{aligned} \tag{2.14}$$

Finally, substituting these relations into the cartesian equations (2.1) and making use of (2.13) gives $\dot{\mathbf{x}}_i = 0$.

It is clear that the vortices must lie on a great circle because $\mathbf{x_1}$, $\mathbf{x_2}$ and $\mathbf{x_3}$ are linearly dependent.

We next prove part (2). For fixed equilibria, we know from part (1) that $\mathbf{M}\sigma = \sum \Gamma_i^2\mathbf{x_i} = \mathbf{0}$. Also we have that $\mathbf{M} = \sum \Gamma_i\mathbf{x_i} = \mathbf{0}$. Therefore:

$$\begin{aligned}\Gamma_1^2\mathbf{x_1} + \Gamma_2^2\mathbf{x_2} + \Gamma_3^2\mathbf{x_3} &= 0 \\ \Gamma_1\mathbf{x_1} + \Gamma_2\mathbf{x_2} + \Gamma_3\mathbf{x_3} &= 0\end{aligned}$$

Multiplying the second equation by Γ_1 and subtracting from the first gives:

$$\Gamma_2(\Gamma_2-\Gamma_1)\mathbf{x_2} = \Gamma_3(\Gamma_1-\Gamma_3)\mathbf{x_3}$$

which means that either $\Gamma_1 = \Gamma_2 = \Gamma_3$ or that $\mathbf{x_2}$ is parallel to $\mathbf{x_3}$. Multiplying the second equation by Γ_2 and subtracting from the first gives

$$\Gamma_1(\Gamma_1-\Gamma_2)\mathbf{x_1} = \Gamma_3(\Gamma_2-\Gamma_3)\mathbf{x_3}$$

which means that either $\Gamma_1 = \Gamma_2 = \Gamma_3$ or that $\mathbf{x_1}$ and $\mathbf{x_3}$ are parallel. Since it is not possible for $\mathbf{x_1}$ parallel to $\mathbf{x_2}$ parallel to $\mathbf{x_3}$, we can conclude that $\Gamma_1 = \Gamma_2 = \Gamma_3$ and that $\mathbf{x_1}+\mathbf{x_2}+\mathbf{x_3}$ $= 0$. The second condition implies that the vortices must lie on an equilateral triangle. To see this, write

$$\mathbf{x_i} = R(\cos(\theta_i)\hat{i} + \sin(\theta_i)\hat{j})$$

and let $\theta_1 = 0$ with no loss of generality. Using $\mathbf{x_1}+\mathbf{x_2}+\mathbf{x_3} = 0$ gives:

$$1 + \cos(\theta_2) + \cos(\theta_3) \;=\; 0$$

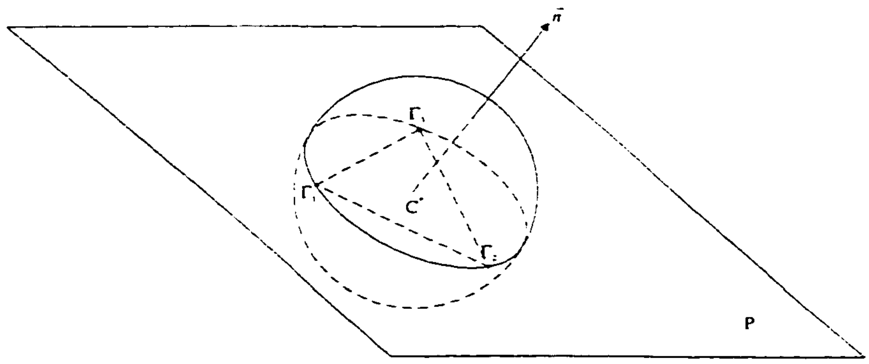

(a)

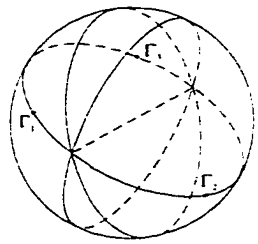

(b)

Figure 2.5: Degenerate states : (a) c^* is at the origin. (b) vortices must lie on great circle.

$$\sin(\theta_2) + \sin(\theta_3) \quad = \quad 0$$

Solving these equations gives $\theta_2 = \frac{2\pi}{3}$ and $\theta_3 = \frac{4\pi}{3}$, hence the triangle is equilateral. Figure 2.7(a) depicts this state.

To prove part (3),start with (2.14) which gives:

$$\begin{aligned}
\Gamma_2 &= \Gamma_1 \frac{l_{12}^2 + l_{23}^2 - l_{31}^2}{l_{12}^2 + l_{31}^2 - l_{23}^2} \\
\Gamma_3 &= \Gamma_1 \frac{l_{23}^2 + l_{31}^2 - l_{12}^2}{l_{12}^2 + l_{31}^2 - l_{23}^2}
\end{aligned}$$

We also have the following elementary relations between the sides and the angles of a triangle:

$$\begin{aligned}
l_{12}^2 &= l_{23}^2 + l_{31}^2 - 2l_{23}l_{31}\cos(\alpha_3) \\
l_{23}^2 &= l_{31}^2 + l_{12}^2 - 2l_{31}l_{12}\cos(\alpha_1) \\
l_{31}^2 &= l_{12}^2 + l_{23}^2 - 2l_{12}l_{23}\cos(\alpha_2)
\end{aligned}$$

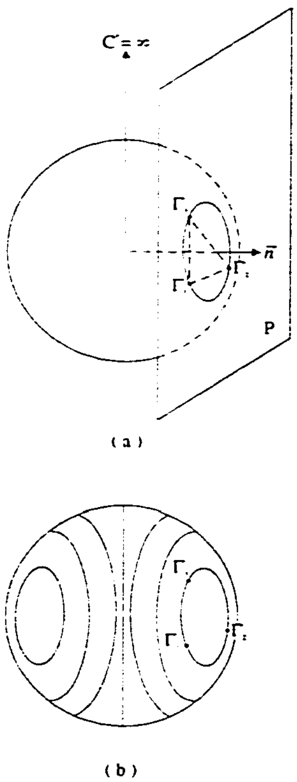

Figure 2.6: Limiting super-radial states : (a) plane P is parallel to c. (b) vortices must lie on vertical latitudes.

Using these relations, the above equations can be written:

$$\begin{aligned} \Gamma_2 l_{31} \cos(\alpha_1) &= \Gamma_1 l_{23} \cos(\alpha_2) \\ \Gamma_3 l_{12} \cos(\alpha_1) &= \Gamma_1 l_{23} \cos(\alpha_3) \end{aligned} \tag{2.15}$$

We also have the sine formula for the sides and angles of a triangle:

$$\frac{l_{23}}{\sin(\alpha_1)} = \frac{l_{31}}{\sin(\alpha_2)} = \frac{l_{12}}{\sin(\alpha_3)}$$

Using this in (2.15) gives the relation in part (3).

A non-degenerate great circle state is shown in figure 2.7(b). The vortex triangle can be either acute or obtuse.

There are several points worth emphasizing:

1. It is clear that the necessary condition generalizes to N vortex equilibria on the sphere.

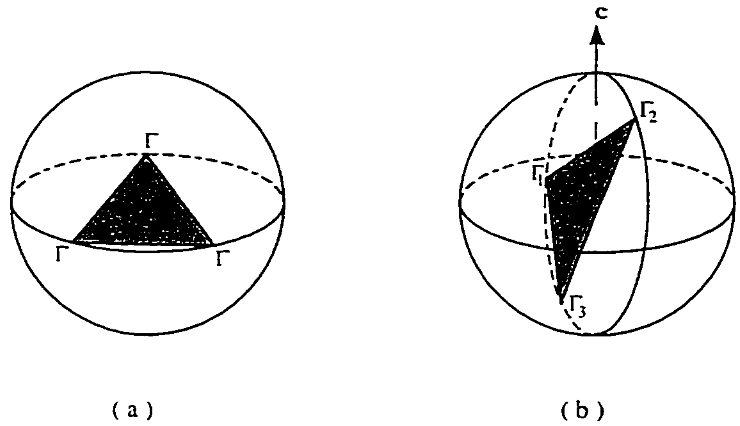

Figure 2.7: Fixed equilibrium states. (a) $\Gamma_1 = \Gamma_2 = \Gamma_3$, equilateral triangle, degenerate great circle state. (b) Non-degenerate great circle state.

2. In the plane, fixed equilibria imply h = 0 [77]. On the sphere it can be shown that fixed equilibria imply $h \neq 0$.

3. In the plane, only collinear configurations can be fixed [77], whereas on the sphere only vortices placed on a great circle can be fixed. This is because of the condition (2.13) which implies that the three vectors $\mathbf{x}_1$, $\mathbf{x}_2$, $\mathbf{x}_3$ are co-planar.

4. In the plane, fixed states are possible only for $\Gamma_1, \Gamma_2 > 0$, $\Gamma_3 < 0$[77]. On the sphere, fixed states are possible for both $\Gamma_1, \Gamma_2, \Gamma_3 > 0$, and $\Gamma_1, \Gamma_2 > 0, \Gamma_3 < 0$.

2.3.2 Relative Equilibria

The starting point for an analysis of the relative equilibria on the sphere is that $\mathbf{c} \cdot \mathbf{x}_i = const$. Therefore each vortex moves on a cone around the center of vorticity vector staying on a fixed latitude. Since each of the vortex triangle sides is constant, we can conclude that there is only one frequency of rotation around c, which we label $\dot{\phi}_i \equiv \omega = const$. Figure 2.8 depicts the general situation, which we summarize in:

Proposition 2.2 (Relative Equilibria). *1. For degenerate relative equilibria, all states lie on great circles, and the positions and strengths satisfy the relations:*

$$\Gamma_1 cosec(2\alpha_1) = \Gamma_2 cosec(2\alpha_2) = \Gamma_3 cosec(2\alpha_3).$$

The vortices rotate around a fixed vector:

$$\mathbf{x} = -\frac{1}{2\pi R}\left(\frac{\Gamma_1 \mathbf{x}_1(0)}{l_{23}^2} + \frac{\Gamma_2 \mathbf{x}_2(0)}{l_{31}^2} + \frac{\Gamma_3 \mathbf{x}_3(0)}{l_{12}^2}\right)$$

with frequency given by the formula:

$$\omega = \frac{1}{2\pi R}\left[R^2\left(\frac{\Gamma_1}{l_{23}^2} + \frac{\Gamma_2}{l_{31}^2} + \frac{\Gamma_3}{l_{12}^2}\right)^2 - \frac{\Gamma_1\Gamma_2 l_{12}^4 + \Gamma_2\Gamma_3 l_{23}^4 + \Gamma_1\Gamma_3 l_{13}^4}{l_{12}^2 l_{23}^2 l_{31}^2}\right]^{1/2}$$

2. For non-degenerate relative equilibria, the vortices rotate around $\mathbf{c}$ *with constant frequency given by:*

$$\omega = \frac{||\mathbf{M}||}{2\pi R l_{12}^2 l_{31}^2} A/B \tag{2.16}$$

where:

$$\begin{aligned} A &= l_{12}^2 l_{31}^2[\Gamma_2^2(4R^2 - l_{12}^2) + \Gamma_2\Gamma_3(4R^2 - l_{12}^2 - l_{31}^2) + \Gamma_3^2(4R^2 - l_{31}^2) \\ &+ 2R^2\Gamma_2\Gamma_3[l_{12}^2(l_{12}^2 - l_{23}^2) + l_{31}^2(l_{31}^2 - l_{23}^2)]] \\ B &= (\Gamma_2 l_{12}^2 + \Gamma_3 l_{31}^2)[\Gamma_2(4R^2 - l_{12}^2) + \Gamma_3(4R^2 - l_{31}^2)] - 4R^2\Gamma_2\Gamma_3 l_{23}^2 \end{aligned}$$

All such equilibria can be classified in one of two cases:

(a) The vortices form an equilateral triangle, but do not lie on a great circle. The rotation frequency simplifies to:

$$\omega = [\sigma^2 R^2 - 3h\Gamma_1\Gamma_2\Gamma_3 s^2]^{1/2}/2\pi R s^2 \tag{2.17}$$

The normal vector, in general, is neither parallel nor perpendicular to $\mathbf{c}$*. However if* $\Gamma_1 = \Gamma_2 = \Gamma_3$*, the normal vector is parallel to* $\mathbf{c}$*, and the case is a sub-radial latitudinal state shown in figure 2.3. If* $\sigma = 0$*, the normal vector is perpendicular to* $\mathbf{M}$ *and the case is a limiting super-radial state shown in figure 2.6.*

(b) The vortices lie on a great circle, but form triangles of arbitrary shape. The sides of the triangle and vortex strengths satisfy:

$$\begin{aligned} V(0) &= R^2[2(l_{12}^2 l_{23}^2 + l_{23}^2 l_{31}^2 + l_{31}^2 l_{12}^2) - l_{12}^4 - l_{23}^4 - l_{31}^4] - l_{12}^2 l_{23}^2 l_{31}^2 = 0 \\ \dot{V}(0) &= \frac{1}{8\pi}[2R\sum \frac{l_{ij}^2 - l_{jk}^2}{l_{ki}^2}(\Gamma_i + \Gamma_k) - \frac{1}{R}\sum l_{ij}^2(\Gamma_i - \Gamma_j)] = 0 \end{aligned}$$

The normal vector $\mathbf{n}$ *is perpendicular to* $\mathbf{c}$.

To prove the first part of the proposition, start with

$$\mathbf{c} = 0 \Rightarrow \Gamma_1\mathbf{x_1} + \Gamma_2\mathbf{x_2} + \Gamma_3\mathbf{x_3} = 0 \tag{2.18}$$

Taking the dot product of $\mathbf{x_i}$ with the above for $i = 1, 2, 3$ gives:

$$\begin{aligned} \Gamma_2 l_{12}^2 + \Gamma_3 l_{31}^2 &= \\ \Gamma_3 l_{23}^2 + \Gamma_1 l_{12}^2 &= \\ \Gamma_1 l_{31}^2 + \Gamma_2 l_{23}^2 &= 2\sigma R^2 \end{aligned} \tag{2.19}$$

From these, we can write Γ_2 and Γ_3 in terms of Γ_1 and the $l_{ij}s$ as:

$$\begin{aligned} \Gamma_2 &= \Gamma_1 \frac{l_{31}^2(l_{12}^2 + l_{23}^2 - l_{31}^2)}{l_{23}^2(l_{31}^2 + l_{12}^2 - l_{23}^2)} \\ \Gamma_3 &= \Gamma_1 \frac{l_{12}^2(l_{23}^2 + l_{31}^2 - l_{12}^2)}{l_{23}^2(l_{31}^2 + l_{12}^2 - l_{23}^2)} \end{aligned}$$

which upon using the standard triangle relations become:

$$\Gamma_1 cosec(2\alpha_1) = \Gamma_2 cosec(2\alpha_2) = \Gamma_3 cosec(2\alpha_3)$$

To get expressions for $\mathbf{x}$ and ω, start with the equation:

$$\dot{\mathbf{x}}_1 = \frac{1}{2\pi R}[\frac{\Gamma_2\mathbf{x_2} \times \mathbf{x_1}}{l_{12}^2} + \frac{\Gamma_3\mathbf{x_3} \times \mathbf{x_1}}{l_{31}^2}]$$

Using (2.18) in the above and noting the fact that the vortices are in relative equilibrium gives:

$$\dot{\mathbf{x}}_1 = \frac{\Gamma_2\mathbf{x_2} \times \mathbf{x_1}}{2\pi R}(\frac{1}{l_{12}^2} - \frac{1}{l_{31}^2}) = k_1(\mathbf{x_2} \times \mathbf{x_1})$$

Likewise, one can show : $\dot{\mathbf{x}}_2 = k_2(\mathbf{x_1} \times \mathbf{x_2})$. Taken together, we have : $k_2\mathbf{x}_1 + k_1\mathbf{x}_2 \equiv \mathbf{x} = \mathbf{const}$. which gives $\dot{\mathbf{x}}_1 = \mathbf{x} \times \mathbf{x_1}$ from which the expressions for $\mathbf{x}$ and ω follow.

For the second part, the starting point is based on our previous observation that each vortex moves on a fixed latitude rotating around $\mathbf{c}$ with constant frequency. The fact that ω is constant

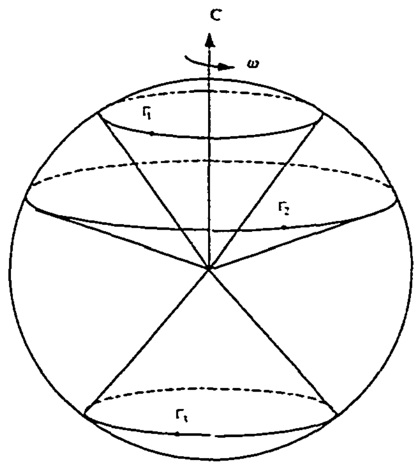

Figure 2.8: Vortices in relative equilibrium move on cones.

follows from equation (2.3) whose right side is constant. Of course, if a vortex is on the axis of rotation, it stays fixed, and for it, ω is undefined. (2.16) follows on using the following relations in (2.3):

$$\begin{aligned} \cos(\theta_i) &= \frac{R\sigma}{||\mathbf{M}||} - \frac{C_1 - \Gamma_j\Gamma_k l_{jk}^2}{2R||\mathbf{M}||\Gamma_i} \\ \cos(\phi_i - \phi_j) &= cosec(\theta_i)cosec(\theta_j)[1 - \cos(\theta_i)\cos(\theta_j) - l_{ij}^2/2R^2] \end{aligned}$$

Since $\omega_1 = \omega_2 = \omega_3$ anyone of the three equations for $\dot{\phi}$ could be used. We use the one for which $\theta \neq 0, \pi$ so that the vortex is not on the axis of rotation.

The two cases (a),(b) are just the conditions giving the fixed points of (2.6) - (2.8), i.e. relative equilibria. We start with case (a) where $l_{12} = l_{23} = l_{31} = s$, and $V \neq 0$. (2.16) can be specialized to yield (2.17) for this case. For $\Gamma_1 = \Gamma_2 = \Gamma_3$, (2.17) further specialises to the result in [15]. Since $\mathbf{n} \cdot \mathbf{c} = V \neq 0$, in general, it follows that $\mathbf{n}$ is at an angle to $\mathbf{c}$. Figure 2.9(a) shows the equilateral triangle state for general $\Gamma_1, \Gamma_2, \Gamma_3$. If the vortex strengths are equal, we see that $\dot{\mathbf{n}} = 0$ which implies that $\mathbf{n}=$ const. But we know that $\mathbf{c}=$ const. and $\mathbf{x}_i \cdot \mathbf{c} =$ const. For both of these conditions to hold, $\mathbf{x}_i$ must describe a cone around both $\mathbf{c}$ and $\mathbf{n}$, which is possible only if they are parallel. This state, in which the vortices just rotate on one fixed latitude, is shown in figure 2.9(b). If $\sigma = 0$, $\mathbf{n} \cdot \mathbf{M} = \sigma V = 0$, which implies that $\mathbf{n}$ and $\mathbf{M}$ are perpendicular. The frequency is obtained by setting $\sigma = 0$ in (2.17), as :

$$\omega = \frac{[\frac{1}{2}(\Gamma_1^2 + \Gamma_2^2 + \Gamma_3^2)]^{1/2}}{2\pi R s}$$

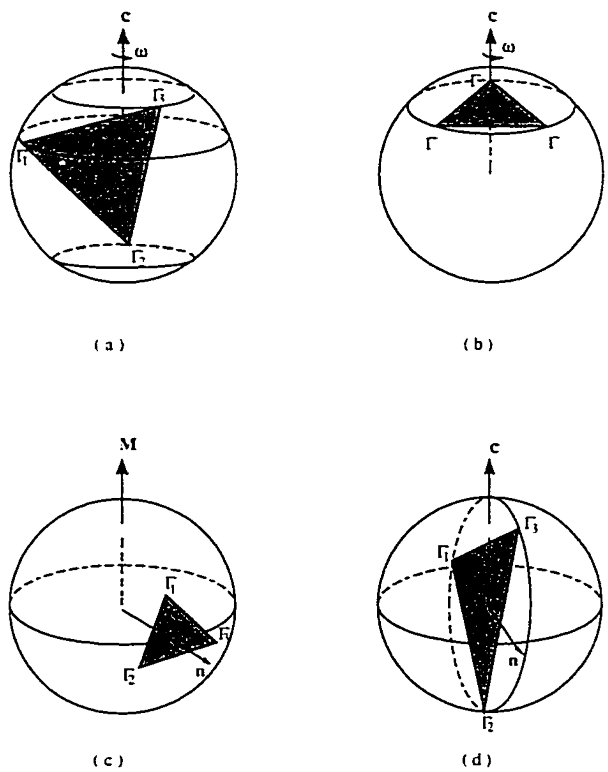

Figure 2.9: Non-degenerate relative equilibrium states.(a) - (c) : Equilateral triangle non-great-circle states. (a) The situation for general $\Gamma_1, \Gamma_2, \Gamma_3$. (b) $\Gamma_1 = \Gamma_2 = \Gamma_3$: Vortices move on one fixed latitude. (c) $\sigma = 0$: Vortices move on different fixed latitudes. (d) Great circle state.

This case is shown in figure 2.9(c). The planar limit $R \to \infty$, s fixed gives $\omega = 0$, i.e. in the planar limit the configuration does not rotate. This is not surprising because $\sigma = 0$ leads to a rigid translation of the vortices in the plane. If we compute the linear velocity of each vortex as:

$$v_i \equiv \omega R \sin(\theta_i) = \omega R[1 - \frac{2\Gamma_i^2 s^2}{(\Gamma_1^2 + \Gamma_2^2 + \Gamma_3^2)R^2}]^{1/2}$$

and take the limit $R \to \infty$, s fixed, we get the limiting value:

$$v = \frac{[\frac{1}{2}(\Gamma_1^2 + \Gamma_2^2 + \Gamma_3^2)]^{1/2}}{2\pi s}$$

which is the velocity of a translating configuration in the plane [87].

Case (b) comprises all great circle configurations, so that $V = 0$. It is straightforward to prove that $V \equiv 0$ if $V(0) = 0$ and $\dot{V}(0) = 0$. This can be seen by differentiating (2.10) repeatedly and using induction. Finally, $\mathbf{n}$ and $\mathbf{c}$ are perpendicular for this case because $\mathbf{x}_1, \mathbf{x}_2, \mathbf{x}_3$ are co-planar. Figure 2.9(d) depicts this case.

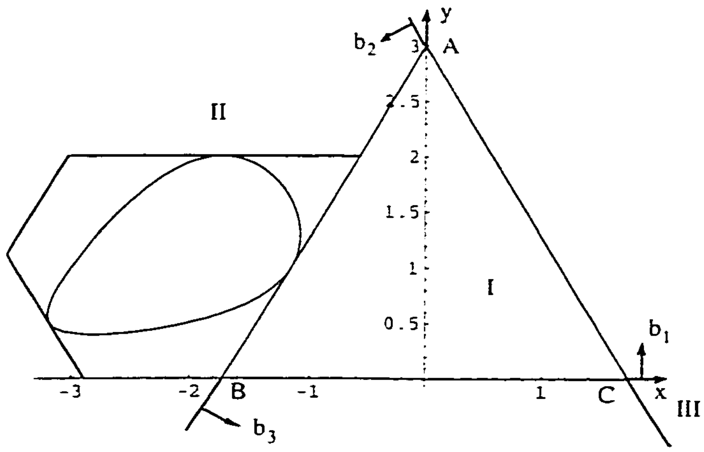

Figure 2.10: Phase plane defining trilinear coordinates and showing a 5-sided domain and the physical region for $\Gamma_1 = 1, \Gamma_2 = \frac{1}{2}, \Gamma_3 = -1, C_1 = -3R^2$

As a final comment, we mention that the stability properties of the various equilibria have been studied in [79].

2.4 Phase Plane Dynamics

In this section we formulate the equations of relative motion in the phase plane [5] and identify the equilibria. Then we discuss the relative dynamics.

The dynamical system (2.6) - (2.8) has a 3-D phase space. However, this can be reduced to a 2-D 'phase plane' by making use of the first invariant (2.11), as pointed out by Synge [98] for the planar problem. To this end, we introduce the variables

$$\begin{aligned} b_1 &= 3l_{23}^2\Gamma_2\Gamma_3/C_1 \\ b_2 &= 3l_{31}^2\Gamma_3\Gamma_1/C_1 \\ b_3 &= 3l_{12}^2\Gamma_1\Gamma_2/C_1 \end{aligned} \tag{2.20}$$

Then it is clear from the defining equation for C_1 that:

$$b_1 + b_2 + b_3 = 3$$

First we assume $C_1 \neq 0$. The case $C_1 = 0$ is treated in §2.5 and the next chapter. As in Aref [5], we use trilinear coordinates (see figure 2.10) to define an arbitrary point P in the plane. The height of the triangle ABC is 3 and (2.11) is identically satisfied for any point P in the phase plane. The trilinear coordinates b_1, b_2, b_3 are related to the rectangular coordinates x.y by

$$\begin{aligned} b_1 &= y \\ b_2 &= \frac{1}{2}(3 - y - \sqrt{3}x) \\ b_3 &= \frac{1}{2}(3 - y + \sqrt{3}x) \end{aligned} \tag{2.21}$$

The second invariant (2.12) in the b variables becomes:

$$f(b_1, b_2, b_3) = |b_1|^{1/\Gamma_1}|b_2|^{1/\Gamma_2}|b_3|^{1/\Gamma_3} \tag{2.22}$$

Curves defined by $f(b_1, b_2, b_3) = k$, where k is a constant. are called phase curves. This is the same equation for the phase curves in the planar case, as discussed in [5]. Using (2.21), (2.22) can be written as

$$H(x, y) = \frac{1}{\Gamma_1}\ln|y| + \frac{1}{\Gamma_2}\ln\frac{|3 - y - \sqrt{3}x|}{2} + \frac{1}{\Gamma_3}\ln\frac{|3 - y + \sqrt{3}x|}{2} = const. \tag{2.23}$$

It is straightforward to verify that, in terms of the cartesian variables

$$\begin{aligned} y &= b_1 \\ x &= (b_3 - b_2)/\sqrt{3} \end{aligned}$$

there is a Hamiltonian structure (see [60] for a general discussion) for the equations of motion:

$$\begin{aligned} \dot{x} &= \frac{6\sqrt{3}g^6 V(x, y)}{\pi R C_1^2}\frac{\partial H}{\partial y} \\ \dot{y} &= -\frac{6\sqrt{3}g^6 V(x, y)}{\pi R C_1^2}\frac{\partial H}{\partial x} \end{aligned} \tag{2.24}$$

It is interesting to note that the Hamiltonian structure of the relative equations, (2.6) - (2.8), remains hidden in the original form but becomes transparent when the cartesian variables are used, in the manner described above.

Though the phase plane is unbounded, the system obviously does not explore all of it, because of the compact geometry of the sphere. This is also clear from considering (2.20). Since the vortices lie on a sphere of radius R, the maximum value attained by l_{ij} is $2R$, which means the b_i's lie between 0 and $\frac{12R^2\Gamma_j\Gamma_k}{C_1}$. This means that the region accessible to the system is the interior of a polygonal domain D, which can have 3 to 6 sides depending on the values of $\Gamma_1, \Gamma_2, \Gamma_3$ and C_1. A 5-sided domain is shown in figure 2.10, for $\Gamma_1 = \Gamma_2 = \frac{1}{2}, \Gamma_3 = -1$ and $C_1 = -3R^2$. Even within the domain D. the physically relevant region is restricted by $V^2 \geq 0$. which is called the physical region [5]. For the same values of Γ_i and C_1, the physical region is also shown in the figure.

The physical region boundary, given by V = 0 is expressed in the b variables as

$$3R^2V_p - b_1b_2b_3C_1 = 0 \tag{2.25}$$

where $V_p = [2(\Gamma_1\Gamma_2b_1b_2 + \Gamma_2\Gamma_3b_2b_3 + \Gamma_3\Gamma_1b_3b_1) - (\Gamma_1b_1)^2 - (\Gamma_2b_2)^2 - (\Gamma_3b_3)^2]$. (2.25) shows an important difference between the plane three vortex and the spherical three vortex problems. In the plane, $V_p = 0$ gives the physical region boundary i.e. for a given set of Γ's. we have a fixed boundary. In contrast, on the sphere, the boundary is also a function of C_1 which means that, for a given set of Γ s. we have many physical region boundaries, depending on the initial vortex separations, or in other words, one for each value of C_1. Figures 2.11(a),(b) show these boundaries for three values of C_1, for the case $\Gamma_1 = \Gamma_2 = \Gamma_3 = 1$. As can be seen, in some cases, the physical region is restricted to isolated points, a situation not possible in the planar 3 vortex problem. Since isolated points are devoid of dynamics, these can give rise to new equilibria, the reason why the number of equilibria is higher for the sphere than for the plane.

As mentioned in §2.2. V can take both positive and negative values during the course of the vortex motion. The phase plane can be thought of as 2-sided with the front side having all the positive values and the backside all the negative ones. The two sides are joined together at the physical region boundary, given by the V = 0 curve. When the system, evolving along a phase curve, reaches the physical region boundary, its subsequent evolution will be on the other side of the phase plane.

Using (2.24), we get an important relation for $\dot{V}$ as

$$\dot{V} = \frac{3\sqrt{3}g^6}{\pi RC_1^2}\left(\frac{\partial V^2}{\partial x}\frac{\partial H}{\partial y} - \frac{\partial V^2}{\partial y}\frac{\partial H}{\partial x}\right) \tag{2.26}$$

(2.26) says that $\dot{V} = 0$ at points wherever the curves V^2 = const. and the phase curve H = const. are tangent.

With these preliminaries, we now locate all the equilibria of Propositions 2.1 and 2.2 in the phase plane :

Proposition 2.3 (Location of Equilibria). *1. Fixed equilibria are represented in the phase plane by points P whose trilinear coordinates are given by*

$$b_1 = \frac{3\Gamma_2\Gamma_3(\Gamma_2+\Gamma_3)}{\sum_{i<j}\Gamma_i\Gamma_j(\Gamma_i+\Gamma_j)}$$

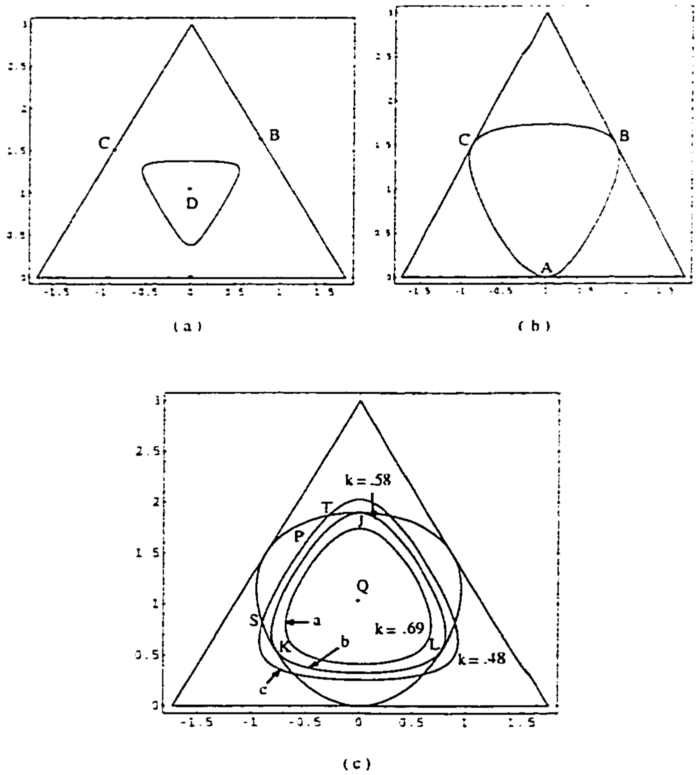

Figure 2.11: Physical region for $\Gamma_1 = \Gamma_2 = \Gamma_3 = 1$. (a) For $C_1 = 9R^2$, the physical region consists of isolated points A, B, C and D. For $C_1 = 8R^2$, the physical region is the area enclosed by the inner triangle plus the isolated points A, B and C. (b) For $C_1 = 6R^2$, the physical region is the area enclosed by the innermost curve. (c) Phase diagram showing the physical region and phase curves for $\Gamma_1 = \Gamma_2 = \Gamma_3 = 1$, $C_1 = 3R^2$.

$$
\begin{aligned}
b_2 &= \frac{3\Gamma_3\Gamma_1(\Gamma_3+\Gamma_1)}{\sum_{i<j}\Gamma_i\Gamma_j(\Gamma_i+\Gamma_j)} \\
b_3 &= \frac{3\Gamma_1\Gamma_2(\Gamma_1+\Gamma_2)}{\sum_{i<j}\Gamma_i\Gamma_j(\Gamma_i+\Gamma_j)}
\end{aligned}
\tag{2.27}
$$

with:

$$
C_1 = \frac{12\Gamma_1\Gamma_2\Gamma_3 h[\Gamma_1\Gamma_2(\Gamma_1+\Gamma_2)+\Gamma_2\Gamma_3(\Gamma_2+\Gamma_3)+\Gamma_3\Gamma_1(\Gamma_3+\Gamma_1)]}{(\Gamma_1+\Gamma_2)(\Gamma_2+\Gamma_3)(\Gamma_3+\Gamma_1)}
$$

2. (a)Degenerate relative equilibria are located by points U whose trilinear coordinates are given by

$$
b_1 = \frac{3(\Gamma_2+\Gamma_3-\Gamma_1)}{\sigma}
$$

$$b_2 = \frac{3(\Gamma_3 + \Gamma_1 - \Gamma_2)}{\sigma}$$
$$b_3 = \frac{3(\Gamma_1 + \Gamma_2 - \Gamma_3)}{\sigma}$$

with $C_1 = \sigma^2 R^2$.

(b) Non-degenerate relative equilibria are represented by points Q or S where

(i) Q are points representing equilateral triangle configurations, with trilinear coordinates given by,

$$Q = (\frac{1}{\Gamma_1 h}, \frac{1}{\Gamma_2 h}, \frac{1}{\Gamma_3 h})$$

(ii) S are points at which the physical region boundary, $V = 0$ *and the phase curve,* $H =$ *const. are tangent.*

The trilinear coordinates of P are obtained on using the definitions (2.20) in (2.14). Since, for a fixed equilibrium, V = 0 (Proposition 2.1), (2.25) with the b_i s supplied by (2.27) yields the stated expression for C_1. If $\Gamma_1 = \Gamma_2 = \Gamma_3$, then P represents a degenerate fixed equilibrium.

The trilinear coordinates of U are obtained on using definitions (2.20) in (2.19). C_1 has the stated value because c = 0 for a degenerate equilibrium. The condition for equilateral triangles (i.e. equal sides) yields the coordinates of Q. Q is a stationary point of (2.22) and is a maximum for (i) $\Gamma_1, \Gamma_2, \Gamma_3 > 0$ and (ii) $\Gamma_1, \Gamma_2 > 0, \Gamma_3 < 0$, $h < 0$, in which case the curves given by (2.22) are closed around Q. For $\Gamma_1, \Gamma_2 > 0, \Gamma_3 < 0$, $h > 0$, Q is a saddle point and the curves are open, see Aref [5]. From Proposition 2.2, 2(b), we know that all non-degenerate great circle relative equilibria satisfy V = 0 and $\dot{V} = 0$. This, with (2.26), yields the condition stated in (ii).

We now discuss the general relative motions of 3 vortices on a sphere. We first consider the case $\Gamma_1, \Gamma_2, \Gamma_3 > 0$. By (2.11),,we have $C_1 > 0$. This implies that $|c| < R$ i.e. the motions belong to the subradial category. By (2.20), $b_i > 0$ and so the region in the phase plane that is relevant to the motion is the interior of the equilateral triangle formed by the points $A = (0, 3)$, $B = (-\sqrt{3}, 0)$, $C = (\sqrt{3}, 0)$. $Q = (1/\Gamma_1 h, 1/\Gamma_2 h, 1/\Gamma_3 h)$ is a global maximum for (2.22), hence all phase curves are closed around Q. The details of the motions are presented for $\Gamma_1 = \Gamma_2 = \Gamma_3 = 1$ and for a value of $C_1 = 3R^2$.

Shown in figure 2.11(c) are the physical region for this case and three phase curves a,b and c each of which is representative of a different type of motion on the sphere. The curve a lies entirely in the physical region, so $V \neq 0$ at any time, which means the vortices never attain a great circle state, and hence maintain their initial orientation. The curve b is tangent to $V = 0$ at the points J,K and L. From Proposition 2.3, 2(ii), we know that these points represent relative equilibria. All initial states on curve b evolve to one of these states. The curve c intersects

$V = 0$. Consider the evolution of an initial state on this curve. like the one represented by the point P in the figure. This state corresponds to the vortices not being on a great circle as $V \neq 0$. The evolution will take this state to either the state S or the state T, both of which lie on the physical region boundary i.e. where $V = 0$. The actual state attained will depend on the initial orientation of the vortices i.e whether $V > 0$ or $V < 0$. On reaching the boundary. the state will continue to evolve on the other side of the phase plane until it again hits the boundary. this time from the other side. upon which it is back on the same side that it initially started on. Thus the evolution continues in a periodic manner. This means, that on the sphere initially non-great circle planes become great circle planes periodically. This scenario holds in general for any $\Gamma_1, \Gamma_2, \Gamma_3 > 0$, however. the various curves will lack the symmetry of the present case. These qualitative motions are the exact counterparts of the planar 3-V motions, as described in [5].

The other case we consider is $\Gamma_1, \Gamma_2 > 0, \Gamma_3 < 0$. We need to distinguish two cases $C_1 \neq 0$ and $C_1 = 0$. The second case will be considered in the next section and chapter. For $C_1 \neq 0$, the relevant regions in the phase plane are regions II and III (figure 2.10).

If $h < 0$, Q is a maximum which is global in region III. and the earlier discussion applies. In region II, the phase curves must pass through A and B and since V = 0 never passes through these points, it follows that these curves are intercepted by it so that the motions correspond to the ones represented by curves b and c, discussed earlier. If $h > 0$, Q is a saddle point and the phase curves are open, so again they always meet the physical region boundary. Again. all these motions are quite similar to the ones already described in the plane, say in Aref [5], except that in the last case. the motion can become unbounded in the plane, something that is obviously not possible on the sphere.

2.5 A special solution

In this section, we first describe the phase plane and then compute the relative and absolute motions of the vortices when $\Gamma_1 = \Gamma_2 = -\Gamma_3 = \Gamma$ and $C_1 = 0$. These conditions imply, by (2.11) and (2.12), that

$$l_{12}^2 = l_{23}^2 + l_{31}^2 \tag{2.28}$$

and

$$\frac{l_{23}^2 l_{31}^2}{l_{12}^2} = const. \tag{2.29}$$

(2.28) says that the vortices always form a right triangle with l_{12} giving the length of the hypotenuse. l_{23} and l_{31} are given by $l_{12}\cos\alpha$ and $l_{12}\sin\alpha$ where α is the angle between l_{12} and l_{23}.

Since $C_1 = 0$, we redefine the phase plane variables b_i :

$$b_1 = l_{23}^2/4\Gamma_1 R^2; \qquad b_2 = l_{31}^2/4\Gamma_2 R^2; \qquad b_3 = l_{12}^2/4\Gamma_3 R^2.$$

so that we have the following identity

$$b_1 + b_2 + b_3 = C_1/4R^2(\Gamma_1\Gamma_2\Gamma_3) = 0.$$

We no longer have tri-linear coordinates. However, we can still represent the states of the system in a phase plane. For this, we use b_1, b_2 as the rectangular coordinates. It is readily seen that $b_1, b_2 > 0$ so that the phase plane is the first quadrant. The physical region is given by the triangle OAB (see figure 2.12) with A = $(0,\frac{1}{\Gamma})$ and B = $(\frac{1}{\Gamma},0)$. Lines OA and OB are inaccessible to the motion because these correspond to 2 vortex collapses. However, AB is accessible and all the states on this line are great circle states which implies that $l_{12} = 2R$. It is also clear, from the fact that $l_{23} = 0$ at A and increases monotonically to 2R at B, that α decreases monotonically from $\frac{\pi}{2}$ at A to 0 at B.

The phase curves are given by $\frac{1}{b_1} + \frac{1}{b_2} = const.$ A typical curve, PSQ is shown in the figure. These are hyperbolas symmetric with respect to the line $b_1 = b_2$ i.e. if (b_1^*, b_2^*) lies on the curve, then so does (b_2^*, b_1^*)(Points E and F in the figure). On the front side of the plane, where $V > 0$, the vectorfield has the direction shown. It will, of course, be in the opposite direction, on the backside.

Further, we have $\alpha = const.$ on any ray through the origin, such as OC, because, on this line,

$$\frac{b_2}{b_1} = \frac{l_{31}^2}{l_{23}^2} = \tan^2\alpha = \lambda = const. \tag{2.30}$$

In particular, the angle bisector OW has $\alpha = \frac{\pi}{4}$ i.e all states on this line are isosceles right triangles. Moreover, $\dot{V} = 0$ on OW which makes W a non-degenerate great circle relative equilibrium. (Proposition 2.2,2(b))

We can further deduce, from the phase plane, that

1) l_{12} has time period T whereas l_{23} and l_{31} have periods 2T. This is because, $l_{12}(P) = l_{12}(Q)$ = 2R, as pointed out earlier.

2) the vortex triangle has the same shape and size at four different times, in general, in one period.

This can be seen quite simply by considering states such as E and F, corresponding to the intersection of the phase curve PQ with the rays OC and OD, symmetric with respect to $b_1 = b_2$. The slopes of OC and OD are $\tan\beta$ and $\cot\beta$ respectively. By (2.30), this means that the triangle corresponding to E will have α given by $\tan^2 \alpha_E = cot\beta$ and that corresponding to F by $\tan^2 \alpha_F = \tan \beta$. These two relations imply $\alpha_E = \frac{\pi}{2}$ - α_F which, together with (2.29), means the 2 triangles are congruent. In exactly, the same way, we obtain two more such triangles from the backside of the plane, making a total of four times that a triangle attains the same shape and size, in one period. However, the great circle triangles attain the same size and shape only three times in one period.

We now compute first the relative, and using that, the absolute motion of the vortices.

Using (2.28) and (2.29), we have

$$V = \pm\frac{1}{2} l_{23} l_{31} \sqrt{4R^2 - l_{12}^2}$$

and from (2.6) we get.

$$\frac{d}{dt}(l_{12}^2) = \mp\frac{\Gamma cosec 2\alpha_0}{2\pi R^2} sgn(l_{31}^2 - l_{23}^2)\sqrt{(4R^2 - l_{12}^2)(l_{12}^2 - 4R^2 \sin^2 2\alpha_0)} \tag{2.31}$$

where α_0 is the value of α at t = 0 and the initial state is taken on the line AB in the phase plane. for convenience i.e. $l_{12}(0) = 2R$. (Since the motion is periodic. this can be done without any loss of generality). (2.31) is integrated to give

$$l_{12} = 2R[\cos^2 \frac{ut}{2} + \sin^2 2\alpha_0 \sin^2 \frac{ut}{2}]^{\frac{1}{2}}$$

where

$$u = \frac{\Gamma cosec 2\alpha_0}{2\pi R^2}$$

Using this in (2.28) and (2.29) gives us l_{23} and l_{31} as

$$l_{23} = [\frac{l_{12}(l_{12} \pm \sqrt{l_{12}^2 - 4R^2 \sin^2 2\alpha_0})}{2}]^{\frac{1}{2}}$$

and

$$l_{31} = [\frac{l_{12}(l_{12} \mp \sqrt{l_{12}^2 - 4R^2 \sin^2 2\alpha_0})}{2}]^{\frac{1}{2}}$$

The appropriate sign is chosen depending on whether $l_{23} > l_{31}$ (segment QS of the phase curve) or $l_{23} < l_{31}$ (segment PS).

We can conclude the following about the relative motion :

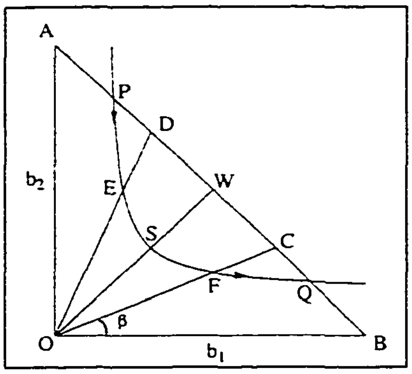

Figure 2.12: Phase diagram for $C_1 = 0$, $\Gamma_1 = \Gamma_2 = -\Gamma_3 = 1$.

1) The period of l_{12} is half that of l_{23} and l_{31}.

2) l_{12}, l_{23}, l_{31} can never equal zero i.e. there is no collapse.

However, the vortices can be made to approach within ϵ of each other, no matter how small ϵ is. This is because l_{12}, the biggest of separations, has a minimum value of 2R $\sin 2\alpha_0$, attained at times $t = \frac{(2n+1)\pi}{u}$, n=0,1... Hence, by choosing α_0, the initial angle as $\frac{1}{2}\sin^{-1}\frac{\epsilon}{2R}$ or $\frac{\pi}{2} - \frac{1}{2}\sin^{-1}\frac{\epsilon}{2R}$, the closest distance of approach of the vortices can be made to be ϵ, an event termed ϵ - collapse, in [58].

Knowing the l_{ij}s, we now compute the frequencies and the spherical polar angles θ_i and ϕ_i for the three vortices. θ_i is given by the formula

$$\cos(\theta_i) = 1 + \frac{\Gamma_j \Gamma_k l_{jk}^2}{2R^2 \Gamma_i \sigma}.$$

The frequencies are calculated using (2.3) and are given by

$$\dot{\phi}_1 \equiv \omega_1 = \frac{2\Gamma R^2}{\pi} \frac{1}{l_{12}^2(4R^2 - l_{23}^2)} \tag{2.32}$$

$$\dot{\phi}_2 \equiv \omega_2 = \frac{2\Gamma R^2}{\pi} \frac{1}{l_{12}^2(4R^2 - l_{31}^2)} \tag{2.33}$$

$$\dot{\phi}_3 \equiv \omega_3 = \frac{\Gamma}{\pi} \frac{1}{l_{12}^2} \tag{2.34}$$

We first integrate (2.34) to get

$$\phi_3 = \tan^{-1} \sin 2\alpha_0 \tan \frac{ut}{2} \tag{2.35}$$

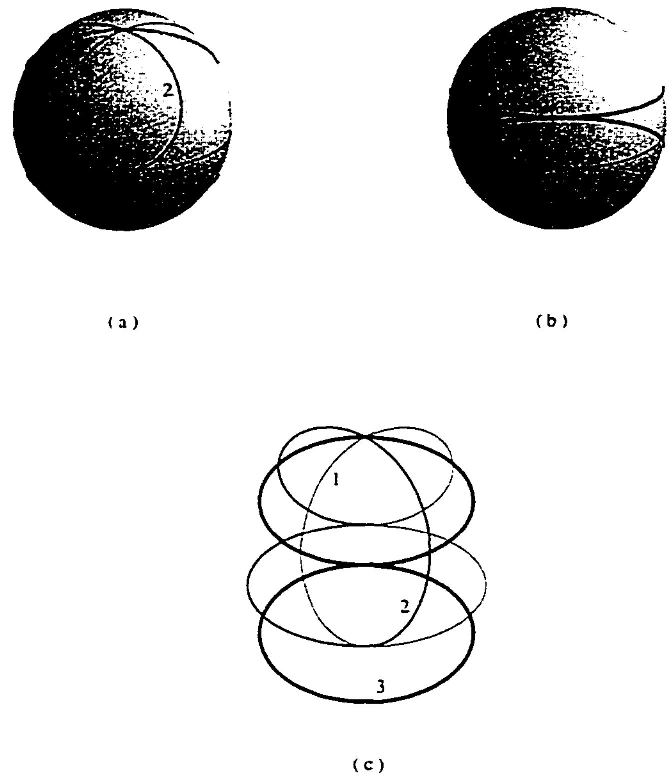

Figure 2.13: Vortex trajectories for $\Gamma_1 = \Gamma_2 = -\Gamma_3 = 1$, $C_1 = 0$. The vortices always form a right triangle. (a) Top view (b) View from the bottom (c) Top view through a transparent sphere

Then using (2.34), we get

$$
\begin{aligned}
\phi_1 &= \phi_3 + \cos^{-1}\frac{l_{23}}{l_{12}}\sqrt{\frac{4R^2 - l_{12}^2}{4R^2 - l_{23}^2}} \\
\phi_2 &= \phi_3 - \cos^{-1}\frac{l_{31}}{l_{12}}\sqrt{\frac{4R^2 - l_{12}^2}{4R^2 - l_{31}^2}}
\end{aligned}
$$

Finally, we have formulae for the cartesian coordinates of the vortices :

$$
\begin{aligned}
x_1 &= \frac{l_{23}}{l_{12}^2}\left[l_{23}\sqrt{4R^2 - l_{12}^2}\cos(\frac{ut}{2}) - 2Rl_{31}\sin(2\alpha_0)\sin(\frac{ut}{2})\right] \\
y_1 &= \frac{l_{23}}{l_{12}^2}\left[l_{23}\sqrt{4R^2 - l_{12}^2}\sin(\frac{ut}{2})\sin(2\alpha_0) + 2Rl_{31}\cos(\frac{ut}{2})\right] \\
z_1 &= \frac{1}{2R}[2R^2 - l_{23}^2]
\end{aligned}
$$

$$
\begin{aligned}
x_2 &= \frac{l_{31}}{l_{12}^2}[l_{31}\sqrt{4R^2 - l_{12}^2}\cos(\frac{ut}{2}) + 2Rl_{23}\sin(2\alpha_0)\sin(\frac{ut}{2})] \\
y_2 &= \frac{l_{31}}{l_{12}^2}\left[l_{31}\sqrt{4R^2 - l_{12}^2}\sin(\frac{ut}{2})\sin(2\alpha_0) - 2Rl_{23}\cos(\frac{ut}{2})\right] \\
z_2 &= \frac{1}{2R}[2R^2 - l_{31}^2] \\
x_3 &= \sqrt{4R^2 - l_{12}^2}\cos(\frac{ut}{2}) \\
y_3 &= \sqrt{4R^2 - l_{12}^2}\sin(2\alpha_0)\sin(\frac{ut}{2}) \\
z_3 &= \frac{1}{2R}[2R^2 - l_{12}^2].
\end{aligned}
$$

The following conclusions can be drawn about the absolute motion :

1) All the vortices have a period of $T = \frac{4\pi}{u}$, whereas l_{12} has time period $\frac{T}{2}$ and l_{23} and l_{31} have periods T.

2) If $\alpha_0 = \frac{\pi}{4}$, we have the non-degenerate great circle relative equilibrium, mentioned earlier, corresponding to the point W in the phase plane. Vortex 3 stays fixed on the c axis whereas 1 and 2 go around on the equator at a frequency, ω, deduced from (2.16) as

$$
\omega = \frac{\Gamma}{4\pi R^2}
$$

In figure 2.13, we plot the trajectories of all three vortices for $\Gamma = 1$ and an initial angle $\alpha_0 = 10^0$.

Chapter 3

Collapse of three vortices

When three point vortices of differing signs move on the surface of a sphere, it is possible for them to collapse self-similarly in finite time. The corresponding collapse process for planar point vortices has been well studied [5, 73, 75, 98], yet despite the fact that the spherical problem is more geophysically relevant [25, 82], this is the first work to study spherical collapse.

In this chapter, we describe the collapse process in detail, and contrast it with the planar collapse process for which much more is known. Aside from its inherent mathematical interest, there is recent evidence [26, 27] that three vortex collapse in the plane and on the sphere is the most frequent interaction for finite sized vortices in dilute 2D turbulence simulations.

In §3.1, we present the necessary and sufficient conditions for self - similar collapse and describe the collapse process in detail.We calculate the collapse times and the vortex velocities during the collapse process. In §3.2, we present a 'geometric' view of collapse; in particular, we examine why for a given set of vortex strengths and initial separations, there are 'partner' states which collapse in different times. In §3.3, we study the collapse process in the stereographic plane; in this plane the collapse is not self-similar. Finally, in §3.4, we describe the phase plane for the collapsing system and present another view of how 'partner states' come about.

3.1 Collapse process

Our analysis is based on the equations for the chord lengths (l_{12}, l_{23}, l_{31})

$$\frac{d(l_{12}^2)}{dt} = \frac{\Gamma_3 V}{\pi R}[\frac{1}{l_{23}^2} - \frac{1}{l_{31}^2}] \tag{3.1}$$

$$\frac{d(l_{23}^2)}{dt} = \frac{\Gamma_1 V}{\pi R}[\frac{1}{l_{31}^2} - \frac{1}{l_{12}^2}] \tag{3.2}$$

$$\frac{d(l_{31}^2)}{dt} = \frac{\Gamma_2 V}{\pi R}[\frac{1}{l_{12}^2} - \frac{1}{l_{23}^2}] \tag{3.3}$$

This system has two invariants (cf. §2.2)

$$C_1 = \Gamma_1\Gamma_2 l_{12}^2 + \Gamma_2\Gamma_3 l_{23}^2 + \Gamma_3\Gamma_1 l_{31}^2 \equiv 0 \tag{3.4}$$

$$C_2 = (l_{12}^2)^{1/\Gamma_3} \cdot (l_{23}^2)^{1/\Gamma_1} \cdot (l_{31}^2)^{1/\Gamma_2} \tag{3.5}$$

which arise from the conservation of momentum and energy. The first invariant is zero due to the fact that the chord lengths vanish at collapse. This implies that the vortex strengths cannot all have the same sign, so we use the convention $\Gamma_1 > 0, \Gamma_2 > 0, \Gamma_3 < 0$.

We recall a formula for the magnitude of c (cf. §2.2) :

$$||\mathbf{c}||^2 = R^2 - C_1/\sigma$$

from which we conclude

$$C_1 = 0 \Leftrightarrow ||\mathbf{c}|| = R, \tag{3.6}$$

assuming $\sigma \neq 0$.

We start with the ansatz that the ratios of the relative distances between vortices remain constant throughout their motion:

$$l_{12}^2 = \lambda_1 l_{31}^2 \tag{3.7}$$

$$l_{23}^2 = \lambda_2 l_{31}^2 \tag{3.8}$$

where:

$$\begin{aligned}\lambda_1 &= (\frac{l_{12}(0)}{l_{31}(0)})^2 \\ \lambda_2 &= (\frac{l_{23}(0)}{l_{31}(0)})^2\end{aligned}$$

The second conserved quantity, C_2 yields:

$$(l_{31}^2(t))^{\sum 1/\Gamma_i} = const.$$

implying

$$\sum_{i=1}^{3} \frac{1}{\Gamma_i} = 0 \tag{3.9}$$

There are two observations one can make regarding the conditions (3.6) and (3.9). Using these conditions together. it is possible to prove that neither equilateral, nor isosceles triangles can collapse, hence $l_{12} \neq l_{23} \neq l_{31}$. Furthermore, if we make the assumption that $\Gamma_1.\Gamma_2 > 0.\Gamma_3 < 0$, then l_{12}, which is the chord length joining the two vortices of like sign, must have length lying in between the other two.

The collapse times are obtained analytically by using (3.1),(3.2),(3.3) along with (3.7),(3.8) to get a scalar equation for l_{31}^2

$$\begin{aligned}\frac{d}{dt}(l_{31}^2) &= \frac{\Gamma_1}{\pi R}(\frac{\lambda_1 - 1}{\lambda_1\lambda_2})V/l_{31}^2 \\ &= \frac{\Gamma_2}{\pi R}(\frac{\lambda_2 - \lambda_1}{\lambda_1\lambda_2})V/l_{31}^2 \\ &= \frac{\Gamma_3}{\pi R}(\frac{1 - \lambda_2}{\lambda_1\lambda_2})V/l_{31}^2\end{aligned}$$

which gives a relationship to be satisfied among the vortex strengths and the initial conditions:

$$\Gamma_1(\lambda_1 - 1) = \Gamma_2(\lambda_2 - \lambda_1) = \Gamma_3(1 - \lambda_2).$$

These conditions can be derived from the previous conditions (3.4) and (3.5).

Solving for l_{31}^2 is straightforward and gives:

$$l_{31}^2(t) = l_{31}^2(0) \pm \alpha\omega t - \frac{\rho\omega^2}{4}t^2 \tag{3.10}$$

where:

$$\alpha = \sqrt{1 - \rho l_{31}^2(0)}$$

Since the coefficient:

$$\frac{\rho\omega^2}{4} = \frac{\Gamma_2^2(\lambda_1 - \lambda_2)^2}{16\pi^2 R^2(\lambda_1\lambda_2)} > 0$$

we know there are two zeroes of $l_{31}^2(t)$, one positive, one negative. We denote the positive collapse time $\tau^{\pm}$ (the $\pm$ corresponds to the $\pm$ in front of the term linear in 't'). It is straightforward to verify that the negative zero is $-\tau^{\mp}$. After some algebra, (3.10) reduces to the exact formula:

$$l_{ij}(t) = l_{ij}(0)(1 + \frac{t}{\tau^{\mp}})^{1/2}(1 - \frac{t}{\tau^{\pm}})^{1/2} \tag{3.11}$$

where

$$\tau^{\pm} \quad = \quad \frac{4\pi R^2\sqrt{\gamma}}{\Gamma_2|(\lambda_1 - \lambda_2)|}(1 \pm \beta) > 0 \tag{3.12}$$

with

$$\begin{aligned}
\gamma &= 2(\lambda_1 + \lambda_2) - (\lambda_1 - \lambda_2)^2 - 1 \\
\beta &= \sqrt{1 - \rho l_{13}^2(0)} \\
\rho &= \lambda_1\lambda_2/R^2\gamma.
\end{aligned}$$

Note that, for the same initial vortex separations and vortex strengths, we have, in general, two distinct collapsing states with distinct collapse times. We call these collapsing states 'partner' states. Of the two collapse times ($\tau^{\pm}$), the one which occurs for a given configuration depends on the orientation of the vortices, V(0) as well as $\dot{V}(0)$. For the planar case, Aref [5] shows that associated with each collapsing configuration, there is a 'partner' expanding state. These partner states in the plane are the analogs of the partner states on the sphere. We can compare these collapsing states more closely with those in the plane by expanding the formulas (3.11) near collapse. Their asymptotic expansions near collapse are:

$$l_{ij}(t) \sim A \cdot (1 - \frac{t}{\tau^{\pm}})^{1/2} + B \cdot (1 - \frac{t}{\tau^{\pm}})^{3/2} + O((1 - \frac{t}{\tau^{\pm}})^{5/2}) \tag{3.13}$$

with constants A and B given by

$$A = l_{ij}(0)\sqrt{1+\frac{(1\pm\alpha)}{(1\mp\alpha)}} \tag{3.14}$$

$$B = -l_{ij}(0)\Gamma_2|\lambda_1-\lambda_2|\tau^{\pm}\sqrt{1+\frac{(1\pm\alpha)}{(1\mp\alpha)}}/(8\pi R^2\sqrt{\gamma}) \tag{3.15}$$

The planar result of Aref [5] gives the exact collapse formula

$$l_{ij}(t) = l_{ij}(0)\cdot(1-\frac{t}{\tau})^{1/2}.$$

The leading term of (3.13) agrees with the exact planar results aside from the coefficient. The higher order terms represent the corrections due to the spherical geometry.

We next calculate the trajectories of each vortex on the route towards collapse. A difference between the planar and spherical problems is that for the planar case, there is only one frequency associated with the collapsing state, [75] given by:

$$\omega_p = \dot{\phi}_i = \frac{1}{4\pi}\sum_{i,j=1}^{3}(\Gamma_i+\Gamma_j)/l_{ij}^2$$

On the sphere, however, since the orientation of the vortex triangle changes in time, in general $\dot{\phi}_1 \neq \dot{\phi}_2 \neq \dot{\phi}_3$. The frequencies are given by the formulas:

$$\omega_i \equiv \dot{\phi}_i = \frac{1}{2\pi}[\Gamma_j(\cos(\theta_j)-\cot(\theta_i)\sin(\theta_j)\cos(\phi_i-\phi_j))/l_{ij}^2 + \Gamma_k(\cos(\theta_k)-\cot(\theta_i)\sin(\theta_k)\cos(\phi_k-\phi_i))/l_{ki}^2] \tag{3.16}$$

where $i \neq j \neq k$. To write these frequencies directly as functions of time,we first need to calculate $\cos(\theta_i)$ in terms of the l_{ij}s. It is straightforward to derive:

$$\cos(\theta_i) = 1+\frac{\Gamma_j\Gamma_k l_{jk}^2}{2R^2\Gamma_i\sigma} \tag{3.17}$$

To calculate $\cos(\phi_i-\phi_j)$ in terms of l_{ij}, we start with:

$$l_{ij}^2 = 2R^2(1-\cos(\theta_i)\cos(\theta_j)-\sin(\theta_i)\sin(\theta_j)\cos(\phi_i-\phi_j)) \tag{3.18}$$

which gives:

$$\cos(\phi_i-\phi_j) = cosec(\theta_i)cosec(\theta_j)(1-\cos(\theta_i)\cos(\theta_j)-l_{ij}^2/2R^2)$$

Finally, using the formulas (3.17) and (3.18) in (3.16) gives the result:

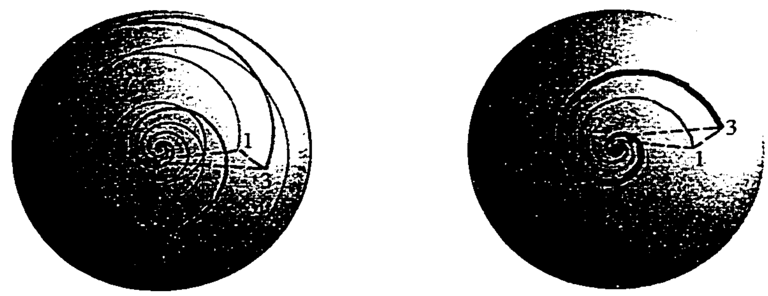

(a) (b)

Figure 3.1: Vortex paths for collapsing partner states. (a) Vortices collapse in time τ_+ (b) Vortices collapse in time τ_-. Notice that the vortices are anticlockwise in (a) and clockwise in (b).

$$\omega_i = \frac{\omega_p - (\Gamma_j + \Gamma_k)/(8\pi R^2)}{1 + (\Gamma_j \Gamma_k l_{jk}^2(t)/4\Gamma_i R^2 \sigma)}$$

where $i \neq j \neq k$. Note that in the above formula for ω_p, the expression for length l_{ij} should be that on the sphere, as given by (3.11). These equations can easily be integrated to give expressions for the angles $\phi_i(t)$:

$$\phi_i(t) = \phi_i(0) + D_i \ln(\frac{\tau^{\mp} + t}{\tau^{\pm} - t})^{\frac{\tau^{\pm}}{\tau^{\mp}}} + B_i[\tan^{-1}(\gamma_i t + \delta_i) - \tan^{-1}\delta_i] \tag{3.19}$$

where:

$$\begin{aligned}
D_i &= \frac{A_i}{l_{jk}^2(0)} \frac{\tau^+ \tau^-}{\tau^+ + \tau^-} \\
A_1 &= \frac{1}{\Gamma_2(1+\lambda)} \frac{(\Gamma_1 + \Gamma_2)^3 + \Gamma_1^3(1 + 1/\lambda) + \Gamma_2^3(1+\lambda)}{4\pi(\Gamma_1 + \Gamma_2)} \\
A_2 &= \frac{1}{\Gamma_1} \frac{\lambda}{1+\lambda} \frac{(\Gamma_1 + \Gamma_2)^3 + \Gamma_1^3(1 + 1/\lambda) + \Gamma_2^3(1+\lambda)}{4\pi(\Gamma_1 + \Gamma_2)} \\
A_3 &= \frac{(\Gamma_1 + \Gamma_2)^3 + \Gamma_1^3(1 + 1/\lambda) + \Gamma_2^3(1+\lambda)}{4\pi(\Gamma_1 + \Gamma_2)^2} \\
B_i &= \frac{2(A_i \alpha_i + \beta_i)\tau^+ \tau^-}{\alpha_i l_{jk}^2(0)} \frac{1}{\sqrt{-[(\tau^+ + \tau^-)^2 + 4\tau^+ \tau^- / \alpha_i l_{jk}^2(0)]}} \\
\alpha_i &= \Gamma_j \Gamma_k / (4\Gamma_i R^2 \sigma) \\
\beta_i &= (\Gamma_j + \Gamma_k)/(8\pi R^2) \\
\gamma_i &= \frac{2}{\sqrt{-[(\tau^+ + \tau^-)^2 + 4\tau^+ \tau^- / \alpha_i l_{jk}^2(0)]}}
\end{aligned}$$

$$\delta_i = \frac{\tau^{\mp} - \tau^{\pm}}{\sqrt{-[(\tau^+ + \tau^-)^2 + 4\tau^+\tau^-/\alpha_i l_{jk}^2(0)]}}$$

where λ is related to λ_2 by $\lambda = \frac{\Gamma_1}{\Gamma_2\lambda_2}$. Near collision, we can use the asymptotic expansions for $l_{ij}(t)$ to get expansions for the frequencies:

$$\omega_1 \sim \frac{(1 \mp \alpha)}{2}\omega_p - \frac{1}{8\pi R^2}[(\Gamma_2 + \Gamma_3) + R^2(\sum \frac{\Gamma_i + \Gamma_j}{l_{ij}^2(0)})(\frac{(\alpha^2 - 1)}{2} + 2\alpha_1 l_{23}^2(0))] + O((1 - t/\tau^{\pm}))$$

$$\omega_2 \sim \frac{(1 \mp \alpha)}{2}\omega_p - \frac{1}{8\pi R^2}[(\Gamma_1 + \Gamma_3) + R^2(\sum \frac{\Gamma_i + \Gamma_j}{l_{ij}^2(0)})(\frac{(\alpha^2 - 1)}{2} + 2\alpha_2 l_{31}^2(0))] + O((1 - t/\tau^{\pm}))$$

$$\omega_3 \sim \frac{(1 \mp \alpha)}{2}\omega_p - \frac{1}{8\pi R^2}[(\Gamma_1 + \Gamma_2) + R^2(\sum \frac{\Gamma_i + \Gamma_j}{l_{ij}^2(0)})(\frac{(\alpha^2 - 1)}{2} + 2\alpha_3 l_{12}^2(0))] + O((1 - t/\tau^{\pm}))$$

Notice that the leading term of each frequency agrees (up to a multiplicative constant) with the planar frequency ω_p. The correction terms make each frequency distinct. We show in figure 3.1 two partner collapsing trajectories for the three vortices ($\Gamma_1 = 1, \Gamma_2 = 1, \Gamma_3 = -\frac{1}{2}$).

We summarize here our main conclusions:

Proposition 3.1 (Self-similar collapse). *1. Necessary and sufficient conditions for self-similar collapse on the sphere are given by:*

(i) $C_1 = 0$

(ii) $\sum \frac{1}{\Gamma_i} = 0$

(iii) The vortices do not form an equilibrium.

2. *Collapsing configurations occur in pairs, which we call 'partner states'. For each given collapse configuration with collapse time denoted* τ^+, *its partner state is obtained by anti-cyclically permuting the indices. The collapse time associated with the partner state is* $\tau^- \neq \tau^+$.

3. *The lengths of the sides of the vortex triangle are given by the formulas:*

$$l_{ij}(t) = F(t) \cdot (1 - t/\tau^{\pm})^{1/2}$$

where:

$$F(t) = l_{ij}(0) \cdot (1 + t/\tau^{\mp})^{1/2}$$

with $\tau^{\pm} > 0$ *given by formulas (3.12). Near collapse, the asymptotic expansions are:*

$$l_{ij}(t) \sim A \cdot (1 - t/\tau^{\pm})^{1/2} + B \cdot (1 - t/\tau^{\pm})^{3/2} + O((1 - t/\tau^{\pm})^{5/2})$$

where A and B are constants given by the formulas (3.14),(3.15).

4. *Each vortex trajectory has a frequency associated with it, defined by $\dot{\phi}_i = \omega_i$ (i=1,2,3) with:*

$$\omega_i = (\omega_p - \beta_i)/(1 + \alpha_i l_{jk}^2(t))$$

where:

$$\begin{aligned} \omega_p &= \frac{1}{4\pi}\sum_{i,j=1}^{3}(\Gamma_i + \Gamma_j)/(l_{ij}^2(t)) \\ \alpha_i &= \Gamma_j\Gamma_k/(4\Gamma_i R^2\sigma) \\ \beta_i &= (\Gamma_j + \Gamma_k)/(8\pi R^2) \end{aligned}$$

Notice that $\alpha_i \to 0, \beta_i \to 0$ as $R \to \infty$, hence $\omega_i \to \omega_p$, which has the form of the frequency associated with the planar problem [5], but with the spherical l_{ij}s.

5. *Integrating the formulas for ω_i and using the explicit expressions for θ_i gives us the exact formulas for the trajectories of the collapsing vortices, in terms of polar coordinates centered at the collapse point $(r_i, \phi_i) = (R\sin(\theta_i), \phi_i)$:*

$$r_i = 2Rl_{jk}\sqrt{-\alpha_i(1 + \alpha_i l_{jk}^2)}$$

and the angles ϕ_i are given by the formulas (3.19).

6. *Near collapse, the frequencies have asymptotic expansions given by the formulas:*

$$\omega_i \sim \delta \cdot \omega_p + \rho_i + O((1 - t/\tau^{\pm}))$$

where $\delta = (1 \mp \alpha)/2$ and ρ_i is given by the formula:

$$\rho_i = -\frac{1}{8\pi R^2}[(\Gamma_j + \Gamma_k) + R^2(\sum \frac{\Gamma_i + \Gamma_j}{l_{ij}^2(0)})(\frac{(\alpha^2 - 1)}{2} + 2\alpha_i l_{jk}^2(0))]$$

To understand why the conditions in (1) are sufficient, we need to describe the phase plane associated with the collapsing states. We do this in the last section.

Hence, there are three differences between the spherical collapse process and the planar collapse process

- The spherical collapse has two distinct collapse times, whereas the planar collapse has one. In the plane, the analogue of the partner state is a self-similar expanding state [5] which cannot occur on the sphere because of the extra length scale R which puts an upper bound on the maximum chord length.

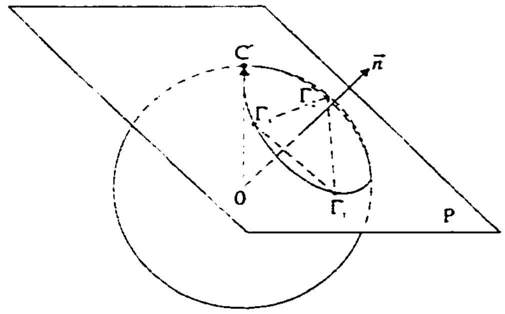

(a)

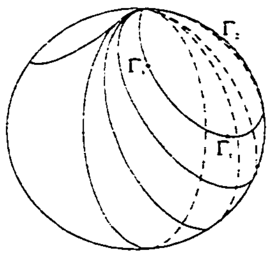

(b)

Figure 3.2: (a) C^* lies on sphere surface and on the vortex plane P. (b) Family of intersections of P with the sphere. Vortices are squeezed to the North Pole as P becomes tangent there.

- The exact formulas for chord lengths are different for the sphere and the plane, however the leading term near collapse agrees with the planar result, with higher order corrections due to the spherical geometry.
- In the plane, the vortices all rotate with the same angular velocity as they collapse, whereas on the sphere, each has a distinct angular velocity.

3.2 A geometric view of collapse

To understand the collapse process further, and in particular why there are two distinct collapse times $\tau^{\pm}$ associated with a set of initial conditions we make use of the constraint (3.6).

Figure 3.2 shows the relevant geometry, with the tip of the c vector, denoted C^*, lying at the North Pole. The vortex plane, denoted P, always intersects this point, hence the vortices lie on the circles formed by intersecting the plane with the sphere. We first compute the angle between c and $\mathbf{n}$, which we denote $\alpha(t)$.

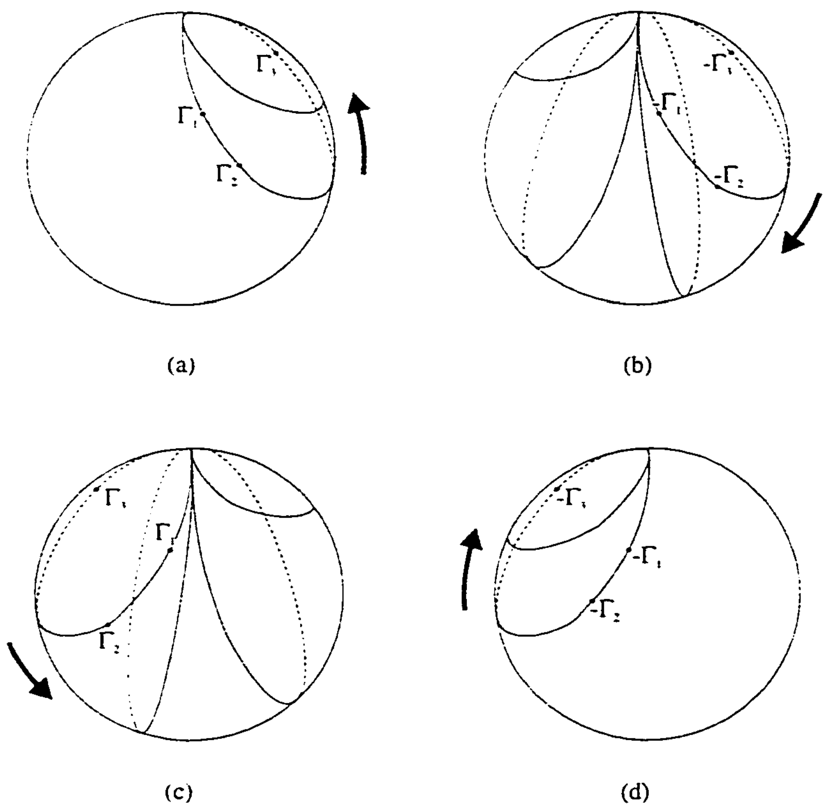

Figure 3.3: Partner states (a) I, (b) I_p, (c) II, (d) II_p. Configurations I and II_p collapse at time τ^-, while I_p and II collapse at time τ^+. In all cases the initial lengths are the same.

Since

$$\mathbf{c} \cdot \mathbf{n} = ||\mathbf{c}||||\mathbf{n}|| \cos(\alpha) = V.$$

and $||\mathbf{n}|| = 2|A| \geq 0$ and $||\mathbf{c}|| = R$, we have

$$\cos(\alpha) = V/2|A|R = \pm\sqrt{1 - a^2/R^2} \tag{3.20}$$

Differentiating this formula gives

$$\dot{\alpha} = \frac{1}{R^2 \sin(2\alpha)} \frac{d}{dt}(a^2)$$

which, after using some identities gives

$$\dot{\alpha} = \frac{\rho}{\sin(2\alpha)} \frac{\Gamma_2 V}{\pi R} \left(\frac{1}{l_{12}^2} - \frac{1}{l_{23}^2} \right) \tag{3.21}$$

where

$$\rho = \frac{\lambda_1\lambda_2}{R^2[2(\lambda_1+\lambda_2)-(\lambda_1-\lambda_2)^2-1]} > 0.$$

From (3.20) we can infer that

- $V \geq 0 \Rightarrow 0 < \alpha \leq \frac{\pi}{2} \Rightarrow \sin(2\alpha) \geq 0$,
- $V < 0 \Rightarrow \frac{\pi}{2} < \alpha < \pi \Rightarrow \sin(2\alpha) < 0$.

Thus, from (3.21) it is clear that

- $\dot{\alpha} > 0$ if $l_{12} < l_{23}$,
- $\dot{\alpha} < 0$ if $l_{12} > l_{23}$.

Suppose we have the collapsing configuration shown in Figure 3.3(a), which we call configuration (I). It is set up so that $\Gamma_1, \Gamma_2 > 0, \Gamma_3 < 0$, $l_{12} > l_{23}$ and $V(0) > 0$. Then by (3.21), we have $\dot{\alpha} < 0$ and hence $\alpha \downarrow 0$ as $t \to \tau^-$. To get the partner state associated with configuration (I), consider the same set-up, but with the signs of the Γ's reversed. Because it is the partner state associated with (I), we label this configuration (I_p). We have $\dot{\alpha} > 0$, hence $\alpha \uparrow \pi$ as $t \to \tau^+$. The partner states are related to each other by the opposite directions in which the plane P swings in order to become tangent to the sphere at the North Pole, thereby squeezing the vortices to their ultimate collapse. Another way of achieving the partner state related to (I) is by using the discrete symmetries inherent in the problem (cf. §2.2.1). Consider a configuration (II) obtained by reversing the signs of the x or y coordinates of configuration (I). All the chord lengths l_{ij} remain as in (I), as do the vortex strengths $\Gamma_1, \Gamma_2 > 0, \Gamma_3 < 0$. Once again, $\dot{\alpha} < 0$, hence $\alpha \downarrow 0$ as $t \to \tau^+$. Then, configuration (II_p) is obtained by reversing the signs of the Γ's, giving $\dot{\alpha} > 0, \alpha \uparrow \pi$ as $t \to \tau^-$.

3.3 Stereographic projection

The change of variable

$$r_i = \tan(\theta_i/2)$$

results in a stereographic projection of the vortex Γ_i onto the extended complex plane $\mathcal{C}$ which is tangent to the sphere at the North Pole, as shown in figure 3.4. This point of tangency is at the origin of $\mathcal{C}$, while the South Pole maps to the point at infinity. An important aspect of the stereographic projection is that it is conformal [68] and vector fields on the sphere are mapped in a one-to-one fashion to vector fields on $\mathcal{C}$.

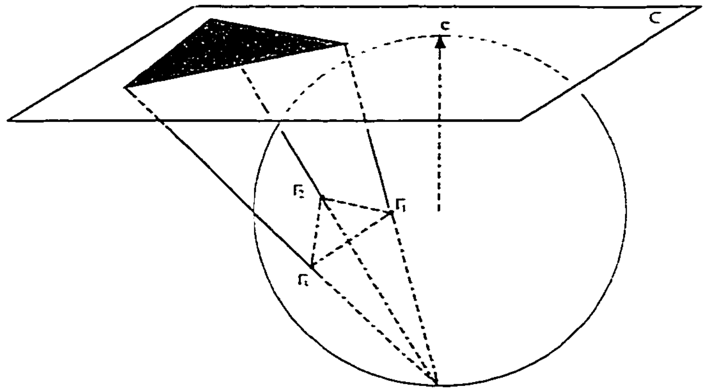

Figure 3.4: Stereographic projection of three vortices.

By a straightforward computation, one gets the new Hamiltonian in $\mathcal{C}$ as

$$\mathcal{H} = \frac{1}{4\pi R^2} \sum_{i<j} \Gamma_i \Gamma_j \log \left(\frac{r_i^2 + r_j^2 - 2r_i r_j \cos(\phi_i - \phi_j)}{(1+r_i^2)(1+r_j^2)} \right) \tag{3.22}$$

with the new equations of motion

$$\begin{aligned} \Gamma_i \frac{d}{dt}(r_i^2) &= -\frac{(1+r_i^2)^2}{2} \frac{\partial \mathcal{H}}{\partial \phi_i} \\ \Gamma_i \frac{d\phi_i}{dt} &= \frac{(1+r_i^2)^2}{2} \frac{\partial \mathcal{H}}{\partial r_i^2} \end{aligned}$$

where (r_i, ϕ_i) are the polar coordinates of the vortex Γ_i in the complex plane $\mathcal{C}$.

Our goal in this section is to show that the collision process in the stereographic plane is not self-similar. To prove this, we will show that the ratios r_{12}/r_{23} and r_{12}/r_{31} are functions of time, where r_{ij} is the distance between vortex Γ_i and Γ_j in $\mathcal{C}$. It is straightforward to show that

$$r_{ij}^2 = \frac{l_{ij}^2}{4R^2[1 + (\Gamma_j \Gamma_k / 4R^2 \sigma \Gamma_i) l_{jk}^2][1 + (\Gamma_k \Gamma_i / 4R^2 \sigma \Gamma_j) l_{ki}^2]}$$

where $i \neq j \neq k$, $i, j, k = 1, \cdots, 3$. Then we can write l_{12} and l_{23} in terms of l_{31} to get

$$\begin{aligned} r_{12}^2 &= \frac{\lambda_1}{4R^2} \frac{l_{31}^2}{(1+\alpha_1 l_{31}^2)(1+\alpha_2 l_{31}^2)} \\ r_{23}^2 &= \frac{\lambda_2}{4R^2} \frac{l_{31}^2}{(1+\alpha_2 l_{31}^2)(1+\alpha_3 l_{31}^2)} \\ r_{31}^2 &= \frac{1}{4R^2} \frac{l_{31}^2}{(1+\alpha_1 l_{31}^2)(1+\alpha_3 l_{31}^2)} \end{aligned}$$

where

$$\begin{aligned}\alpha_1 &= \frac{\Gamma_2\Gamma_3\lambda_2}{4R^2\sigma\Gamma_1}\\ \alpha_2 &= \frac{\Gamma_3\Gamma_1}{4R^2\sigma\Gamma_2}\\ \alpha_3 &= \frac{\Gamma_1\Gamma_2\lambda_1}{4R^2\sigma\Gamma_3}\end{aligned}$$

From these formulas, it is clear that

- $r_{ij} \to 0$ as $t \to \tau^{\pm}$,
- r_{12}/r_{23} and r_{12}/r_{31} are functions of time unless $\alpha_1 = \alpha_2 = \alpha_3$, which is not possible.

This shows that the collapse is not self-similar.

We end this section with several remarks:

1. As shown in the previous section, the angle α between $\mathbf{c}$ and $\mathbf{n}$ is not constant, which is the reason the collapse formulas on the projected $\mathcal{C}$ plane are not self-similar.

2. The Hamiltonian system in the stereographic plane is useful for several other purposes as well. In particular, in studying the streamline topology for the N-vortex problem on the sphere, it is advantageous to study the projected streamlines on the $\mathcal{C}$ plane. This is presented in the next chapter.

3.4 Collapse in the phase plane

To understand why the conditions in Proposition 3.1, (1) are sufficient, we now consider the phase plane associated with collapse. We use the phase plane coordinates introduced in §2.5, where also $C_1 = 0$. These are given by

$$b_1 = l_{23}^2/4\Gamma_1 R^2; \qquad b_2 = l_{31}^2/4\Gamma_2 R^2; \qquad b_3 = l_{12}^2/4\Gamma_3 R^2,$$

so that we have the following identity

$$b_1 + b_2 + b_3 = C_1/4R^2(\Gamma_1\Gamma_2\Gamma_3) = 0.$$

We can no longer use trilinear coordinates. However, we can still represent the states of the system in a phase plane. For this, we use b_1, b_2 as the rectangular coordinates. It is readily seen

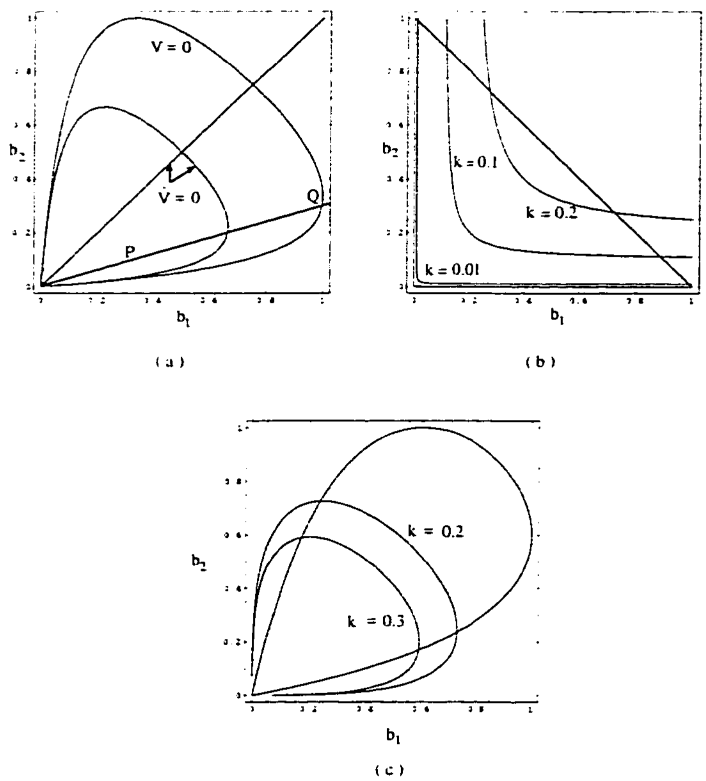

Figure 3.5: Phase plane showing the partner collapsing states. Both states start off at P. but on opposite faces. The one on the front face collapses directly towards the origin, the other evolves first to Q on the $V = 0$ curve. before collapsing to the origin on the front face.

that $b_1, b_2 > 0$ so that the phase plane is the first quadrant. Through each point $P = (b_1, b_2)$ there is a curve of the type

$$b_1^{\frac{1}{r_1}} b_2^{\frac{1}{r_2}} (b_1 + b_2)^{\frac{1}{r_3}} = const. \tag{3.23}$$

Assuming that the conditions in Proposition 3.1,(1) hold, (3.23) can be written as $(\frac{b_1}{b_1+b_2})^{\frac{1}{r_1}} (\frac{b_2}{b_1+b_2})^{\frac{1}{r_2}} = const.$ or

$$(\frac{1}{1+\lambda})^{\frac{1}{r_1}} (\frac{\lambda}{1+\lambda})^{\frac{1}{r_2}} = const.$$

where $\lambda = b_2/b_1 \Rightarrow \lambda$ is a constant i.e. the phase curves are straight lines passing through the origin. Now, since the the physical region given by $V^2 \geq 0$ is always a closed curve through the origin for this case, it follows that all non-equilibrium initial states evolve to the origin, in finite time, which corresponds to collapse.

Figure 3.5 shows the (b_1, b_2) phase plane, with each collapsing trajectory lying on a ray going through the origin. For definiteness, we show the case $\Gamma_1 = \Gamma_2 = 1$, $\Gamma_3 = -\frac{1}{2}$. The partner states associated with a given collapsing configuration are shown on the diagram. The partner states shown in figures 3.3(a) and (c) have identical l_{ij}'s and Γ's, therefore are located by the same point P. However for case (a) we have $V > 0$, while for case (c) we have $V < 0$. In both cases, the sign of $\dot{V}$ is the same. For case (a), the trajectory evolves straight to the origin along the ray (on the front face $V > 0$), collapsing at time τ^-. State (c) evolves away from the origin (on the back face $V < 0$) until it hits the $V = 0$ curve, corresponding to a great circle configuration, then evolves to the origin on the front face $V > 0$, collapsing at the later time $\tau^+ > \tau^-$. The difference between this process and the corresponding one in the plane, described in [5], is that for the planar problem, there is nothing to bound the coordinates from above, hence the accessible region is unbounded. As a result, the trajectory analogous to state (c) continues to travel away from the origin on the same ray, representing a self-similarly expanding state. An analogous explanation can be given for the partner states shown in figures 3.3(b) and (d).

We have seen that self-similar collapse requires $C_1 = 0$ and h=0. If h > 0 or h < 0, we no longer have collapse. This is because, although the physical region boundary, V $= 0$, passes through the origin, the phase curves either don't pass through the origin (h > 0) or they are intercepted by the V $= 0$ curve before they can reach the origin (h < 0). The representative phase plane for each of these cases is shown in figure 3.5(b) ($\Gamma_1 = \Gamma_2 = 1, \Gamma_3 = -1$) and figure 3.5(c) ($\Gamma_1 = \Gamma_2 = 1, \Gamma_3 = -\frac{1}{4}$).

Chapter 4

Streamline topologies

This chapter describes the instantaneous streamline patterns produced by point vortices of general strength on the surface of a two dimensional sphere. The completely integrable cases of two and three vortices are treated in detail both in a fixed inertial frame of reference, and for the case of relative equilibria, in a rotating frame of reference. One of the main results is a general topological classification of the 12 primitive patterns that are allowable for the case of three vortices, from which much more general and complex structures can be constructed via continuous deformation and linear superposition. The analogous planar problem has recently been studied by Aref and Brōns [7]. A general topological classification for all integrable two degree-of-freedom Hamiltonian systems has been carried out recently by Fomenko and co-workers [36, 37].

We start by introducing the equations of particle motion in the stereographic plane; these are compared with the well known equations of motion in the physical plane [5, 6]. In §4.2 we state several general results on stagnation points, consequences of the Poincaré Index Theorem. In §4.3 we classify all topological patterns for the two and three vortex problem, including the streamline patterns associated with all relative equilibria, as well as the collapsing state (cf. Chapter 3) and a special periodic solution (cf. §2.5). In §4.4 we view the patterns for the relative equilibria in a rotating frame of reference chosen so that the vortex configuration is stationary. We end with a discussion of the relevance of this study to a general understanding of global atmospheric weather patterns. In particular, it is argued that the primitive patterns generated from the three vortex problem are probably also useful for understanding and classifying more complex patterns in the general N-vortex problem. It is also conjectured that an important ingredient in understanding unstable global weather phenomena is an understanding of the dynamical topological transitions from one streamline pattern to another, a study which is only in its infancy and will require extensive computation and data analysis to fully understand.

4.1 Stereographic projection

In this section, we project the equations of motion for a fluid particle to the stereographic plane that was introduced in Chapter 3.

The change of variable

$$r = \tan(\theta/2)$$

results in a stereographic projection of the particle located at (θ, ϕ) onto the extended complex plane C which is tangent to the sphere at the North Pole, as shown in figure 4.1. This point of tangency is at the origin of C, while the South Pole ($\theta = \pi$) maps to the point at infinity. Note that we have also non-dimensionalized the equations so that the equator projects to the unit circle. An important aspect of the stereographic projection is that it is conformal [68] and vector fields on the sphere are mapped in a one-to-one fashion to vector fields on C.

The Hamiltonian for particle motion projected onto the extended complex plane C is

$$\mathcal{H}_p(r, \phi; r_i, \phi_i) = \frac{1}{4\pi R^2} \sum_{i=1}^{N} \Gamma_i \ln\left(\frac{r^2 + r_i^2 - 2rr_i\cos(\phi - \phi_i)}{(1 + r^2)(1 + r_i^2)}\right), \tag{4.1}$$

where r and ϕ are the polar coordinates of the particle in the complex plane — notice that r and r_i are dimensionless. Their dimensional counterparts are $s = 2Rr$ and $s_i = 2Rr_i$. It will be convenient to make this distinction when we take the limit $R \to \infty$ in order to make comparisons with the planar system. The Hamiltonian for the vortex motion was presented in Chapter 3.

The equations of motion for a particle can then be written

$$\dot{r^2} = -\frac{(1 + r^2)^2}{2}\frac{\partial \mathcal{H}_p}{\partial \phi} \tag{4.2}$$

$$\dot{\phi} = \frac{(1 + r^2)^2}{2}\frac{\partial \mathcal{H}_p}{\partial r^2}. \tag{4.3}$$

In terms of the cartesian variables, we have

$$\dot{x} = -\frac{(1 + r^2)^2}{4}\frac{\partial \mathcal{H}_p}{\partial y}$$

$$\dot{y} = \frac{(1 + r^2)^2}{4}\frac{\partial \mathcal{H}_p}{\partial x},$$

where $r^2 = x^2 + y^2$, with $\mathcal{H}_p$ being identical to that in (4.1), expressed in cartesian variables. Using the complex notation $z = x + iy$, these last equations can be written more compactly as

$$\dot{z}^* = -i\frac{(1 + ||z||^2)^2}{2}\frac{\partial \mathcal{H}}{\partial z} \tag{4.4}$$

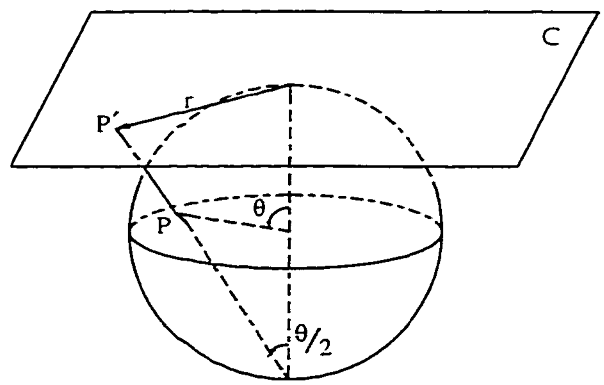

Figure 4.1: Stereographic projection of sphere onto the extended complex plane C. The point P is projected to P'.

where

$$\mathcal{H}(z, z^*) = \frac{1}{4\pi R^2} \sum_{i=1}^{N} \Gamma_i \log\left[\|z - z_i\|^2/(1 + \|z\|^2)(1 + \|z_i\|^2)\right]. \tag{4.5}$$

Written out in expanded form, equation (4.4) becomes

$$\dot{z}^* = -i\frac{(1 + \|z\|^2)^2}{8\pi R^2}\left[\sum_{i=1}^{N} \Gamma_i/(z - z_i) - \sigma z^*/(1 + \|z\|^2)\right]. \tag{4.6}$$

This equation, when written for the vortex motion, generalizes the equation in Hally [45], reducing to it when the total vorticity vanishes, i.e. $\sigma = 0$.

To see how (4.6) behaves in the planar limit $R \to \infty$, consider the equation for the dimensional variable $w = 2Rz$. The system (4.6) transforms as

$$\begin{aligned}\dot{w}^* &= -i\frac{(4R^2 + \|w\|^2)^2}{32\pi R^4}\left[\sum_{i=1}^{N} \Gamma_i/(w - w_i) - \sigma w^*/(4R^2 + \|w\|^2)\right] \\ &= -i\frac{(4 + \|w\|^2/R^2)^2}{32\pi}\left[\sum_{i=1}^{N} \Gamma_i/(w - w_i) - \sigma w^*/R^2(4 + \|w\|^2/R^2)\right].\end{aligned}$$

Then, in the limit $R \to \infty$ where $\|w\|/R << 1$, to leading order we obtain the equations

$$\dot{w}^* = -\frac{i}{2\pi}\sum_{i=1}^{N} \Gamma_i/(w - w_i),$$

which correspond to the planar equations of Aref [5], as one would expect.

Although (4.6) gives the correct velocity at all finite points in the plane, it should not be used to calculate the velocity at the point at infinity, i.e. the image of the South Pole, since the stereographic projection is not continuous there. In the rest of the chapter, this point will be treated separately. In particular situations if it appears that the South Pole could be a stagnation point, this is ascertained by recourse to the vector form of the equations (2.1).

4.2 General Results

We start by stating some general results regarding the stagnation points on a sphere. The motion of a passive particle in the field of N vortices is given by (4.6). The stagnation points on the stereographic plane, $z \equiv z_s$, are stationary points of (4.6) and as such are obtained as solutions of the algebraic system

$$\sum_{j=1}^{N} \Gamma_j/(z_s - z_j) = \sigma z_s^*/(1 + ||z_s||^2). \tag{4.7}$$

It is useful to write this condition in cartesian variables as well. The velocity field at an arbitrary point $\mathbf{x}$ on the sphere is

$$\dot{\mathbf{x}} = \frac{1}{4\pi R} \sum_{j=1}^{N} \Gamma_j(\mathbf{x}_j \times \mathbf{x})/||\mathbf{x}_j - \mathbf{x}||^2. \tag{4.8}$$

The stagnation points, $\mathbf{x} \equiv \mathbf{x}_s$, are then obtained by solving the algebraic system

$$\sum_{j=1}^{N} \Gamma_j(\mathbf{x}_j \times \mathbf{x}_s)/||\mathbf{x}_s - \mathbf{x}_j||^2 = 0. \tag{4.9}$$

We now summarize some general topological consequences arising from the fact that the vortices move on the surface of a sphere. The first consequence is contained in the following general theorem:

Poincaré Index Theorem (PIT) : *The index, $I_f(S)$, of a two dimensional surface S, relative to any C^1 vector field f on S with at most a finite number of critical points is equal to the Euler-Poincaré characteristic of S, denoted $\chi(S)$, i.e. $I_f(S) = \chi(S)$* (see Perko [80]).

Remarks

1. Critical points refer to points where the vector field vanishes or is singular. In our case, these are the stagnation points and the point vortex locations, which in general are not stagnation points.

2. For a sphere, $\chi(S) = 2$. The index of a center is $+1$, while that for a saddle is -1. Hence, if only centers and saddles are present, and c denotes the number of centers, s the number of saddles, then

$$c - s = 2.$$

3. Recall that each vortex is a center, hence there are at least N centers, i.e. $c \geq N$. In the planar problem studied in Aref and Bröns [7], $c = N$.

To understand and categorize the vector fields and streamline patterns, we first need the following definition:

Definition: *A stationary point,* $\mathbf{x}_0$, *of the system* $\dot{\mathbf{x}} = f(\mathbf{x})$ *is called non-degenerate if the Jacobian matrix* $Df(\mathbf{x}_0)$ *has no zero eigenvalues, otherwise it is called degenerate* (see Perko [80]).

The first question of interest is how many stagnation points are present in the flowfield generated by N vortices. To answer this, notice that (4.7) can be written

$$z_s^* = -\frac{\sum_{m=0}^{N-1} a_m z_s^m}{\sum_{m=0}^{N-1} b_m z_s^m} \equiv S(z_s, z_j; \Gamma_j) \tag{4.10}$$

along with its complex conjugate

$$z_s = -\frac{\sum_{m=0}^{N-1} a_m^* z_s^{*m}}{\sum_{m=0}^{N-1} b_m^* z_s^{*m}}. \tag{4.11}$$

Then (4.10) can be substituted into (4.11) to obtain an equation only in z_s

$$z_s = -\frac{\sum_{m=0}^{(N-1)^2} c_m z_s^m}{\sum_{m=0}^{(N-1)^2} d_m z_s^m}, \tag{4.12}$$

which is an algebraic equation of degree $N^2 - 2N + 2$ and hence can have at most as many distinct solutions. To establish the types of stagnation points that can exist in the flow, one can use a standard result from Hamiltonian theory (see Perko [80]) that for a non-degenerate stationary point, only saddles and centers can occur.

More specifically, for the case $N = 1$, (4.7) can be manipulated in order to obtain the result that

$$z_s = -\frac{1}{z_1^*},$$

showing that the stagnation point occurs at the antipodal point associated with the isolated vortex. By the Poincaré Index Theorem, it is clear that this stagnation point must be a center. For the case $N = 2$, it is clear that the vortices must lie on a great circle. From (4.9) we know that the vectors $\mathbf{x_1}$, $\mathbf{x_2}$, $\mathbf{x_s}$ are coplanar, which means that all the stagnation points must lie on this circle as well. If $\sigma = 0$, then (4.7) yields

$$\sum_{j=1}^{N} \Gamma_j/(z_s - z_j) = 0.$$

This is the governing equation for stagnation points in the planar N vortex problem, as discussed in Aref and Bröns [7]. In this case it is known that there are at most $N - 2$ stagnation points and all stagnation points are saddles, whereas for the general spherical problem ($\sigma \neq 0$), there are both saddles and centers.

It is useful here to recall the definition of a Schwarz function, in order to further characterize the stagnation point structure:

Definition: *For a general analytic function S(z), if the roots of the equation $z^* = S(z)$ fill out an analytic arc C, then S(z) is called the Schwarz function of C (see Davis [24]).*

We can then state the following theorem:

Theorem 1 (Schwarz function theorem). *The Schwarz function of an analytic arc C is a rational function of z if and only if C is an arc of a circle or a straight line.*

This means that the roots of (4.10) fill out an analytic arc iff $S(z) = \frac{az+b}{cz+d}$. From (4.10) we know that

$$S(z) = -\frac{\sum_{m=0}^{N-1} a_m z^m}{\sum_{m=0}^{N-1} b_m z^m},$$

where $a_{N-1} = \sigma$. Thus, for $N > 2$, $S(z)$ can be of the form required by the theorem only if $\sigma = 0$. However, for the special case $\sigma = 0$, there can be at most $N - 2$ stagnation points, and they are all isolated. Finally, for the case $N = 3$, the stagnation point must lie on the vortex circle. To see this, consider (4.9) which implies

$$\sum_{j=1}^{N} \frac{\Gamma_j \mathbf{x}_j}{l_j^2} = k(t)\mathbf{x}_s,$$

where $l_j^2 = ||\mathbf{x}_s - \mathbf{x}_j||^2$. Taking the dot product of the above equation with $\mathbf{x}_s$ gives

$$k(t) = \sum_{j=1}^{N} \frac{\Gamma_j}{l_j^2} - \frac{\sigma}{2R^2}.$$

Substituting for $k(t)$ gives

$$\sum \frac{\Gamma_j}{l_j^2}(\mathbf{x}_j - \mathbf{x}_s) = -\frac{\sigma}{2R^2}\mathbf{x}_s = 0,$$

since we have assumed $\sigma = 0$. This equation shows that $\mathbf{x}_1 - \mathbf{x}_s$, $\mathbf{x}_2 - \mathbf{x}_s$, and $\mathbf{x}_3 - \mathbf{x}_s$ are co-planar, which together with the fact that the vortices lie on a circle implies that the stagnation point is on the circle as well. We can now summarize these statements concisely as a general proposition:

Proposition 4.1 (Stagnation point proposition). *In a flowfield of N point vortices on a sphere,*

1. *There are at most $(N^2 - 2N + 2)$ stagnation points if $N > 2$.*
2. *The only possible non-degenerate stagnation points are centers (index = +1) or saddles (index = -1).*
3. *For $N = 1$, there is only one stagnation point. It is a center located at the antipodal point to the vortex.*
4. *For $N = 2$, all stagnation points must lie on the great circle passing through the two vortices.*
5. *If $\sigma = 0$, there can be at most $N - 2$ stagnation points. If $N = 3$, the single stagnation point must lie on the vortex circle.*

Remarks

1. One might wonder why $N^2 - 2N + 2$ is only an upper bound and not the actual number of stagnation points. This is because all solutions of (4.12) are not solutions of (4.10). As a simple example of this, consider the solutions of the complex equation

$$z^* = \frac{z-1}{z+1}. \tag{4.13}$$

If one takes the complex conjugate of this equation, then uses this to get a single equation for z, one gets

$$z^2 = -1,$$

with solutions $z = \pm i$. However both these solutions fail to satisfy (4.13).

2. For each saddle point, the angle α_s between the inset and outset is given by the formula

$$\alpha_s = \tan^{-1}\left[\frac{2(\mathcal{H}_{xy}^2 - \mathcal{H}_{xx}\mathcal{H}_{yy})^{1/2}}{\mathcal{H}_{xx}+\mathcal{H}_{yy}}\right]|_{(x_s,y_s)}.$$

Then one can show

$$\nabla^2\mathcal{H} = -\frac{\sigma}{\pi R^2(1+r^2)^2},$$

giving

$$\alpha_s = \tan^{-1}\left[-\frac{2\pi R^2(1+r^2)^2}{\sigma}(\mathcal{H}_{xy}^2 - \mathcal{H}_{xx}\mathcal{H}_{yy})^{1/2}\right].$$

From this formula, it is clear that $\alpha_s \to \pi/2$ when $\sigma \to 0$. For the planar problem, as was mentioned in Aref and Bröns [7], the corresponding angle must be $\pi/2$. Hence, α_s agrees with the planar case not only in the limit $R \to \infty$, but also when $\sigma = 0$.

4.3 Topological classification of streamline patterns

We now study in some detail the streamline patterns for the case of two and three vortices. In particular, we classify all possible streamline topologies according to a set of 'building block' figures, which we call *primitives*. Using only continuous transformations (homotopies) on the sphere and linear superposition of the primitives, all possible topologies can be constructed.

4.3.1 Two vortices

The case of two vortices is simple enough to be treated in detail. The vortices necessarily lie on a great circle, so for convenience, we assume they lie on the equator defined in the complex plane as the unit circle $||z|| = 1$. Without loss, we can fix the position and strength of one of the vortices, so we take $\Gamma_1 = 1, \phi_1 = 0$, hence $z_1 = 1$. This leaves a two parameter problem as we vary the strength, $\Gamma \in (-\infty, \infty)$, and angle $\phi \in (0, \pi]$ of the second vortex, i.e. we take $z_2 = \exp(i\phi)$. The only case in which the great circle through the vortices is not unique is when they are on opposite sides of the sphere, hence $\phi \equiv \phi^* = \pi$ — we will treat this case separately.

If we let z_s denote the location of the stagnation points, then we know from (4.7) that it must satisfy the algebraic system

$$\frac{1}{z_s - 1} + \frac{\Gamma}{z_s - \exp(i\phi)} = \frac{(1+\Gamma)z_s^*}{1 + z_s z_s^*}.$$

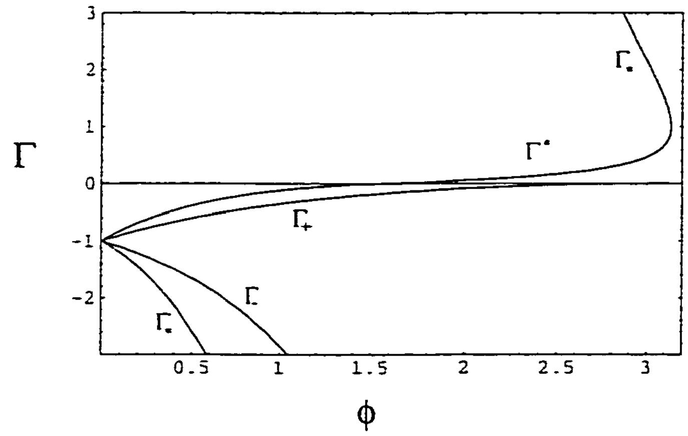

Figure 4.2: Special bifurcation curves for the two vortex problem. Shown are the curves $\Gamma_\pm$ and Γ^*, Γ_* in the (Γ, ϕ) plane.

Since we know that $||z_s||^2 = 1$, we can simplify the equation to obtain

$$F(z_s;\phi,\Gamma) \equiv (1+\Gamma)z_s^2 + (1-\Gamma)(1-\exp(i\phi))z_s - (1+\Gamma)\exp(i\phi) = 0. \qquad (4.14)$$

The solutions of this complex quadratic are summarized in the following proposition:

Proposition 4.2 (Two vortex problem). *Consider the solution of $F(z_s;\phi,\Gamma) = 0$ on the unit circle $||z_s||^2 = 1$, as a function of the two parameters $\phi \in (0,\pi]$, $\Gamma \in [-\infty,\infty]$. In the (ϕ,Γ) plane, define the following two curves, shown in figure 4.2:*

$$\Gamma_+ = \frac{\sin(\phi/2) - 1}{\sin(\phi/2) + 1}, \qquad \Gamma_- = 1/\Gamma_+.$$

Then, for any fixed value $\phi \in (0,\pi]$, we have:

1. *For $\Gamma > \Gamma_+$ or $\Gamma < \Gamma_-$, there are two stagnation points $z_s = z_\pm$ given by*

$$z_+ = \exp(i(\frac{\phi}{2} + \alpha)), \qquad z_- = \exp(i(\frac{\phi}{2} + \pi - \alpha))$$

where

$$\sin(\alpha) = \frac{1-\Gamma}{1+\Gamma}\sin(\frac{\phi}{2}), \qquad (-\frac{\pi}{2} \le \alpha \le \frac{\pi}{2}).$$

The stagnation point at z_+ is a saddle, while the one at z_- is a center.

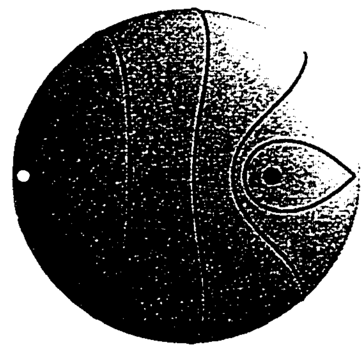

Figure 4.3: Streamline topology showing a cusp.

2. *At the endpoints* $\Gamma = \Gamma_{\pm}$, *the roots coalesce and there is only one stagnation point, which is a cusp located at*

$$z_s = \exp(i(\frac{\phi}{2} \pm \frac{\pi}{2})).$$

3. *For* $\Gamma \in (\Gamma_-, \Gamma_+)$, *there are no stagnation points.*

The proof is based on an examination of the solutions to (4.14), which we write as

$$\begin{aligned} z_{\pm} &= \frac{i(1-\Gamma)\sin(\phi) \pm 2\cos^2(\frac{\phi}{2})h(\Gamma)}{(1+\Gamma)(1+\exp(-i\phi))}, \\ h(\Gamma) &= [(\Gamma-\Gamma_+)(\Gamma-\Gamma_-)]^{1/2}. \end{aligned}$$

There are no stagnation points for $\Gamma \in (\Gamma_-, \Gamma_+)$, because for these values, $||z_{\pm}|| \neq 1$. The classification of type follows from the eigenvalues of the Hessian evaluated at the stationary points:

$$\lambda^2|_{z_+} = \frac{16\Gamma^2\sin^4(\frac{\Gamma}{2}) - \sigma^4[\cos\alpha - \cos(\frac{\phi}{2})]^4}{4\sigma^2[\cos\alpha - \cos(\frac{\phi}{2})]^4} > 0.$$

From the Poincaré Index Theorem, we can deduce that z_- is a center. When the center and saddle coalesce, a cusp is obtained. Figure 4.3 shows a cusp for $\Gamma = -3 + 2\sqrt{2}$, $\phi = \pi/2$.

Remarks

1. The stagnation point z_- always lies on the longer arc connecting the two vortices. z_+ is on the shorter arc for $\Gamma > 0$, and the longer one for $\Gamma < 0$. In the limiting case $\Gamma \to \pm\infty$, the stagnation point z_+ coincides with the first vortex, while in the limit $\Gamma \to 0$, it coincides with the second. These limits are clearly singular.

2. As seen in figure 4.2. the limit $\Gamma \to -1$ is also special. In this limit, there are no stagnation points irrespective of the location of the second vortex. This corresponds to the case $\sigma = 0$ in Proposition 4.1.

3. The limit $\phi \to 0$ corresponds to the planar case studied in Aref and Bröns [7], since the vortices are close together. For the planar problem, there are no stagnation points for the case $\Gamma = -1$. In the spherical problem as $\phi \to 0$, $\Gamma_{\pm} \to -1$ and the stagnation points disappear. Hence, the interval $\Gamma \in (\Gamma_-, \Gamma_+)$ for the spherical problem in which no stagnation points exist is the anologue of the isolated value $\Gamma = -1$ for the plane.

4. As $\phi \to \pi$, $\Gamma_+ \to 0^-$, $\Gamma_- \to -\infty$. Hence when the vortices are at antipodal points, there are no stagnation points for $\Gamma \in (-\infty, 0)$. This case can be summarized as:

Lemma 4.1. *Suppose the vortices are at antipodes on the sphere, i.e. let $\Gamma_1 = 1$, $z_1 = 1$, $z_2 = -1$. Then:*

(a) For $\Gamma > 0$, there is a continuum of stagnation points located on the vertical latitude of the sphere at a distance $2R/(1+\Gamma)$ from z_1.

(b) For $\Gamma = 0$, there is one stagnation point at $z_3 = -1$. This is produced by the vortex located at $z_1 = 1$.

(c) For $\Gamma < 0$, there are no stagnation points.

It is of some interest to study the bifurcations that occur from one pattern to another as the parameters vary. We emphasize that these are not dynamical bifurcations for the two vortex problem, since all solutions are in relative equilibrium so there can be no dynamical bifurcations. Bifurcations in streamline topologies can occur as the parameters ϕ and Γ are varied. The changes fall into two general classes: (1) Homotopies due to the spherical topology; (2) Bifurcations involving changes in the number of stagnation points in the flow.

1. To understand the first type of bifurcation, consider figure 4.4. Shown in this figure is a continuous deformation of one of the primitives (lemniscate as shown in figure 4.4(a)) on the sphere to its homotopic equivalent, the limacon, as shown in figure 4.4(d). As the sphere is pushed through the left loop of the lemniscate, it deforms to a limacon. For the planar problem considered in [7], these two figures are not homotopic equivalents since in that case, it is not possible to continuously deform one to the other.

2. Changes in the number of stagnation points in the flow occur in two cases:

   (i) $\Gamma = 0$: In this case, the saddle point vanishes. As Γ goes through the origin parametrically, the lemniscate/limacon switches to limacon/lemniscate. This type of bifurcation occurs in the planar case as well [7] and is shown in figure 4.5(a), marked as point A;

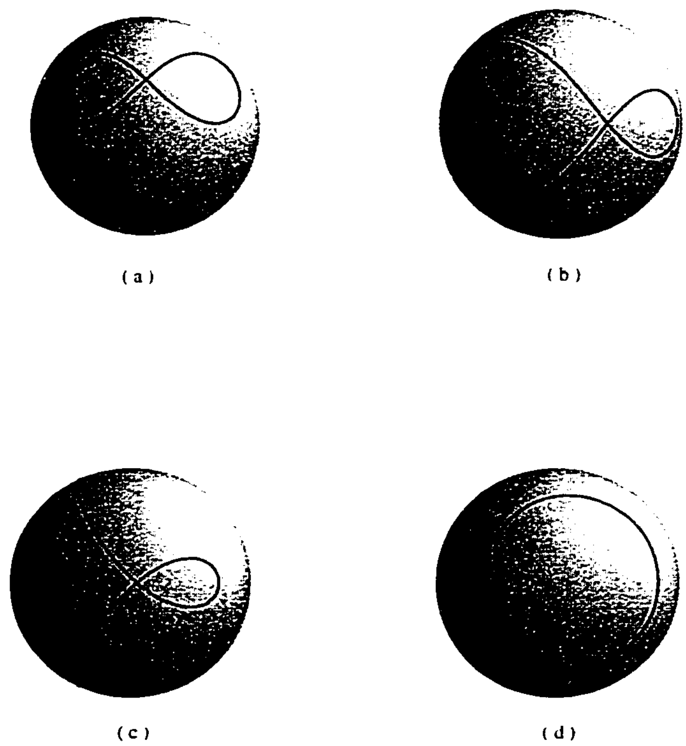

Figure 4.4: Continuous deformation of a lemniscate to a limacon. In the four steps (a), (b), (c), (d), the sphere is pushed through the left loop.

(ii) $\Gamma = \Gamma_{\pm}$: At $\Gamma = \Gamma_{+}$ (marked as point C in figure 4.5(a)), the two stagnation points coalesce to form a cusp. For $\Gamma_{-} < \Gamma < \Gamma_{+}$, there are no stagnation points in the flow. At the value $\Gamma = \Gamma_{-}$ (marked as point D in figure 4.5(a)), the cusp then gives birth to a saddle and center. This kind of bifurcation is unique to the sphere and cannot occur in the plane [7]. Figure 4.5(b) shows the topologies associated with each of the distinct intervals.

A quantitative understanding of the first type of bifurcation is achieved by tracking level curves of the Hamiltonian $\mathcal{H}$ given by (4.5). For $N = 2$ the level curves, in cartesian variables, are given by

$$\frac{[(x-1)^2 + y^2][(x-\cos(\phi))^2 + (y-\sin(\phi))^2]^{\Gamma}}{(1+x^2+y^2)^{1+\Gamma}} = const.$$

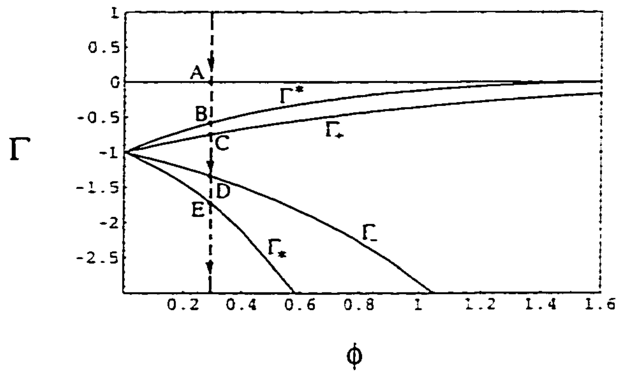

(a)

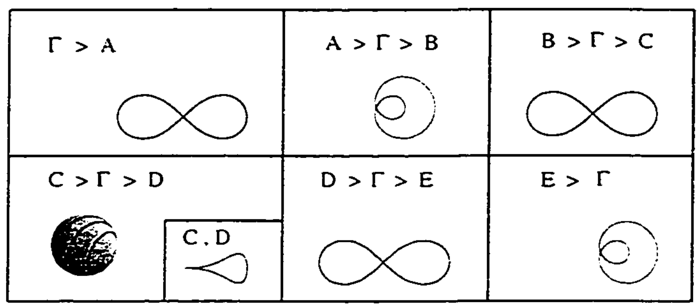

(b)

Figure 4.5: (a) Same curves as shown in figure 4.2. As Γ decreases down the dashed line, topologies change at points marked A, B, C, D, and E; (b) Primitive topologies in each region. Degenerate cusp occurs at points C and D.

Constant values for three particular streamlines are of interest — the ones going through $z_\pm$ and the point at ∞, which we call the dividing streamline. This streamline also passes through the origin and divides the complex plane into two regions. Designating these $c_\pm$ and c_d, we have

$$
\begin{aligned}
c_+ &= 2^{1+\Gamma}\sin^2(\frac{\phi}{4}+\frac{\alpha}{2})\left[\sin^2(\frac{\phi}{4}-\frac{\alpha}{2})\right]^\Gamma && (4.15)\\
c_- &= 2^{1+\Gamma}\cos^2(\frac{\phi}{4}+\frac{\alpha}{2})\left[\cos^2(\frac{\phi}{4}-\frac{\alpha}{2})\right]^\Gamma && (4.16)\\
c_d &= 1. && (4.17)
\end{aligned}
$$

The transition from a primitive to its homotopic equivalent occurs when a stagnation point moves from one region to the other, i.e. crosses the dividing streamline. Only a saddle can cross the dividing streamline since centers are local extrema of the Hamiltonian and hence cannot live on the dividing streamline. To obtain the values of Γ at which this occurs, we solve (4.15) numerically with $c_+ = 1$, viewing Γ as a function of α.

We summarize the behavior in the following lemma:

Lemma 4.2. *Consider $\phi \in (0, \pi)$. $\exists$ two special values of Γ, which we denote Γ^* and Γ_* such that $c_+ = c_d = 1$.*

1. *For $\phi > \pi/2$, we have $\Gamma_* > 1$, $0 < \Gamma^* < 1$.*

2. *For $\phi < \pi/2$, we have $\Gamma_* < -1$, $-1 < \Gamma^* < 0$.*

3. *When $\phi = \pi/2$, we have $\Gamma^* = 0$.*

The curves Γ^*, Γ_* are shown in figure 4.2.

Points B and E in figure 4.5(a) mark the values at which these homotopic bifurcations occur. A typical bifurcation sequence is shown in figure 4.5(b). For the case $\Gamma > 0$, we have a lemniscate topology which switches to a limacon at $\Gamma = 0$ (point A), via a type II bifurcation. This topology persists until $\Gamma = \Gamma^*$ (point B) at which value there us a homotopic bifurcation (type I) to a lemniscate which then gives rise to a cusp (C). In between points C and D (note that this region always includes $\Gamma = -1$) there are no stagnation points and the topology consists of simple closed streamlines. At point D, the cusp gives birth to a saddle and a center, resulting in a lemniscate topology. Finally, at $\Gamma = \Gamma_*$ (point E), the lemniscate again transforms to its homotope, the limacon via a type I bifurcation. For $\Gamma < \Gamma_*$, we have the limacon topology. This general scenario holds for all $\phi \in (0, \pi)$, with two exceptions. When $\phi = \frac{\pi}{2}$, there are only three bifurcations. For $\phi = \pi$, the scenario described in lemma 4.1 holds. These cases are not illustrated in figure 4.5(a).

4.3.2 Three vortices

We now consider the stagnation point structure and streamline topologies in the case of three vortices of general strength. This problem is much richer than the two vortex case, or the planar three vortex case as treated by Aref and Bröns [7]. We start by stating a general proposition classifying the number of stagnation points in the flowfield:

Proposition 4.3. *For the case $N = 3$, let M be the number of non-degenerate stagnation points.*

1. *$M = 1, 3$, or 5.*

2. *If $M = 1$, it must be a saddle. If $M = 3$, there must be two saddles and one center. If $M = 5$, there must be 3 saddles and 2 centers.*

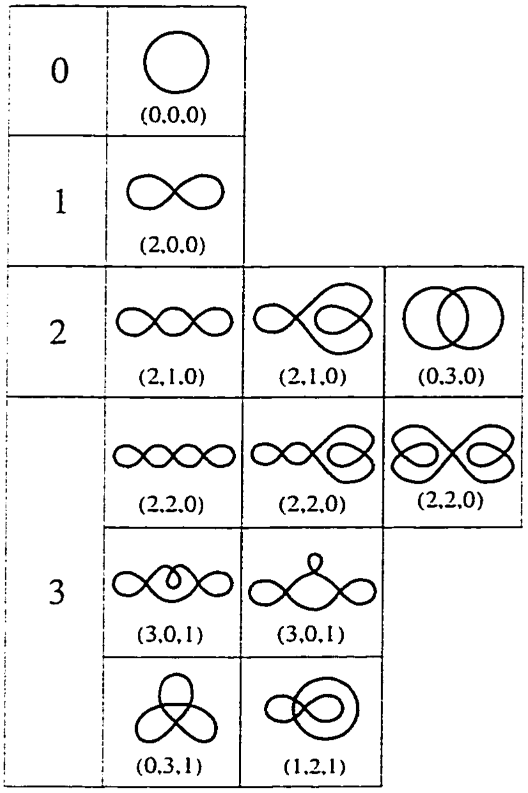

Figure 4.6: Three vortex primitive chart showing the twelve primitive topologies. Number down left denotes the number of saddle points. The three numbers under each figure refer to the number of homoclinic - heteroclinic - triheteroclinic loops.

By Proposition 4.1, $M \leq 5$. If we let s denote the number of saddles and c the number of centers that are stagnation points, then

$$\begin{aligned} s + c &= M \\ -s + c + N &= 2. \end{aligned}$$

From this we have

$$s = \frac{M+1}{2}, \quad c = \frac{M-1}{2},$$

implying that $M = 1, 3, 5$. The second statement follows from the above and the Poincaré Index Theorem.

The main result of this section is a topological classification of all possible primitive topologies that can occur. This classification scheme is in the spirit of Fomenko [36, 37] who has classified all possible topologies associated with integrable systems with two degrees of freedom. For the three vortex problem in the plane. Aref and Bröns [6] have recently identified all possible topologies. In three space, there have been recent attempts at using knot theory to understand and classify flow structures, see for example Ghrist et al [39] and Moffatt [66]. See also the work of Perry and Chong [81] and Dallman [22] for more on the role of topology of streamline patterns in fluid flows.

The classification into 12 primitive topologies is shown in figure 4.6. The left column lists the number of saddle points occuring in the figure. The numbers along the bottom of each figure indicate the number of homoclinic-heteroclinic-triheteroclinic loops in each figure. Hence, the upper left figure is the 'least complex', while that on the bottom right is the 'most complex'. It is important to understand that each primitive can be continuously deformed on the surface of the sphere to a visually distinct but topologically equivalent figure as was shown, for example, in figure 4.4. Hence, each of the twelve figures represents a homotopy equivalence class [90]. We show in figure 4.7 the primitives and their topologically equivalent figures, of which there are 23. As a final point, we mention that any given streamline configuration associated with the three vortex problem will be made up of a general combination of the primitives and their topological equivalents. We show a typical example of such a streamline pattern in figure 4.8 which is a combination of lemniscate and limacon.

4.3.3 Relative equilibrium patterns

In this section we present the streamline patterns that occur when the three vortices lie in a relative equilibrium configuration, as categorized and studied in Chapter 2. The dynamical stability of these equilibria has been studied in Pekarsky and Marsden [79], hence it is now possible to ascertain which of the streamline patterns are associated with dynamically stable patterns. The relevance of this to global atmospheric weather patterns is commented on in the final section.

The number of stagnation points in the flowfield of three vortices in a relative equilibrium could be 1,3, or 5 and hence a variety of topologies are possible. We content ourselves with providing several examples of some of the interesting cases.

Figures 4.9 and 4.10 show two different topologies when the vortices are in a fixed equilibrium, hence lie on a great circle with strengths satisfying the appropriate relations as detailed in Chapter 2. Both configurations are isosceles triangles but with different angles. In the first case, the equal angle is 40^0 and there are three stagnation points (two saddles and a center); in the second, the equal angle is 50^0 and there are five stagnation points (three saddles and two centers). Both configurations are stable [79]. In fact, it can be shown that all fixed equilibria are stable. Figure 4.11 shows four different topologies when the vortices are in a relative equilibrium state. Figure 4.11(a) and 4.11(b) are Great circle states. Both configurations are identical isoceles triangles but with different vortex strengths ($\Gamma_1 = \Gamma_2 = 1$ in both cases, $\Gamma_3 = 1$ in figure 4.11(a), $\Gamma_3 = -4$ in figure 4.11(b)) leading to different topologies. Again, both are stable configurations.

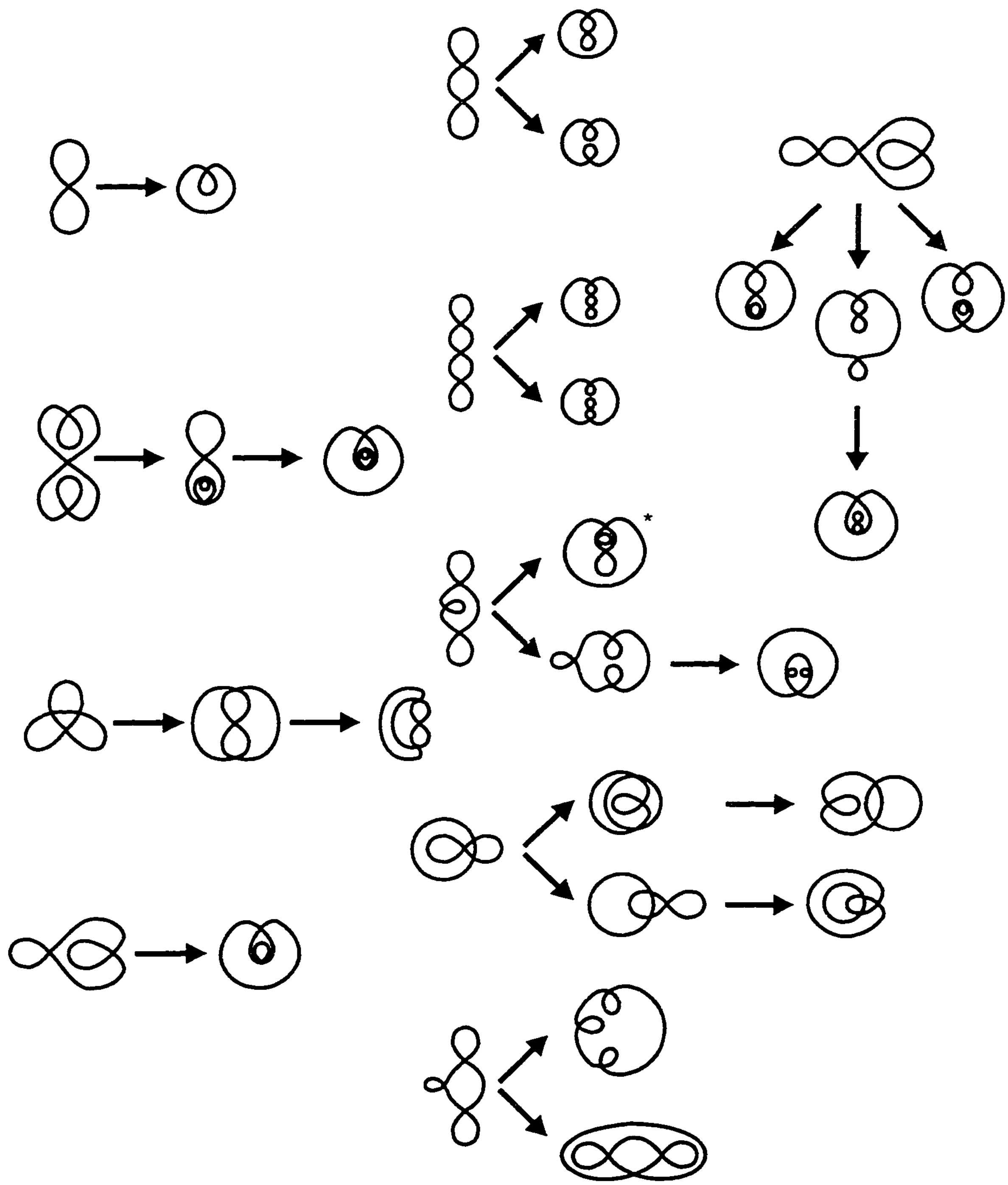

Figure 4.7: Homotopic equivalent figures obtained by continuously deforming each of the primitives shown in figure 4.6.

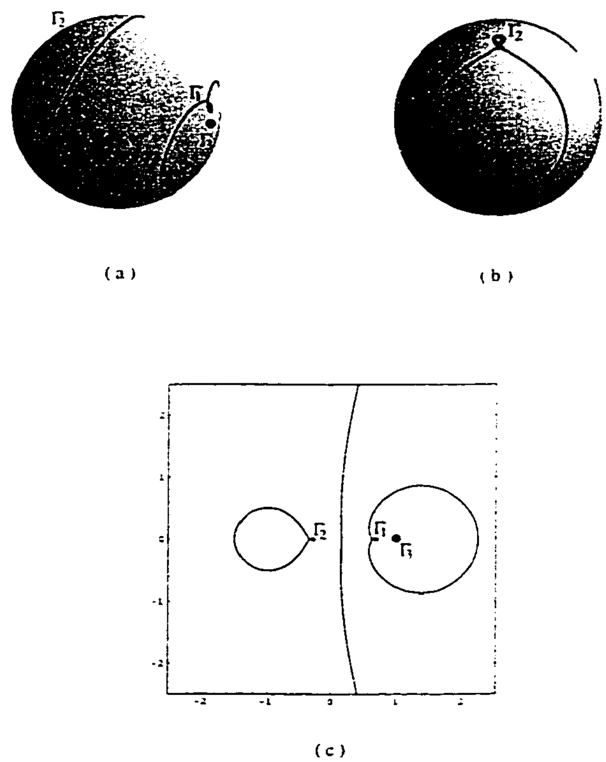

Figure 4.8: Typical three vortex streamline pattern. Shown is a combination of a lemniscate and limacon formed by a three vortex cluster. (a) Front of sphere; (b) Back of sphere; (c) Stereographic projection.

Figures 4.11(c) and (d) pertain to the other type of relative equilibria, the equilateral triangle configuration. Figure 4.11(c) shows a symmetric situation where $\Gamma_1 = \Gamma_2 = \Gamma_3$ and the vortices are on a fixed latitude of 45^0. There are three saddles and two centers and the topology is made up of primitives $(0,3,1)$ and $(0,0,0)$. In figure 4.11(d), $\Gamma_1 = 1, \Gamma_2 = 2, \Gamma_3 = 3$. Since c is aligned with the z-axis, the vortices are not on a fixed latitude. The topology in this case is simpler and consists of a pair of nested lemniscates (primitives $(2,0,0)$ and $(0,0,0)$). Both equilateral triangle configurations are stable.

In general, it is possible to say more about the streamline topologies that can occur when the vortices happen to lie on a great circle at a given time, not necessarily in equilibrium. For this, consider the great circle to be made of the longitudes 0 and π so that in the stereographic plane, the vortices lie on the x-axis. The stagnation points on the great circle can be found by solving (4.7), which takes the form of a cubic:

$$Ax_s^3 + Bx_s^2 + Cx_s + D = 0,$$

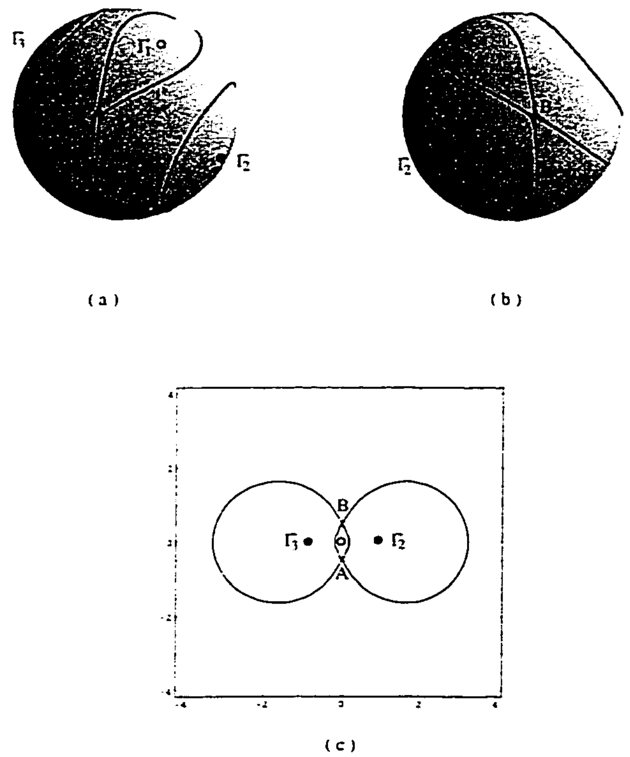

Figure 4.9: Streamline topology for fixed equilibria — vortices are on a fixed longitude. (a) Front of sphere; (b) Back of sphere; (c) Stereographic projection.

where

$$
\begin{aligned}
A &= \sigma \sum x_i - \sum \Gamma_i (x_j + x_k) \\
B &= \sum \Gamma_i x_j x_k + \sigma (1 - \sum x_i x_j) \\
C &= \sigma x_1 x_2 x_3 - \sum \Gamma_i (x_j + x_k) \\
D &= \sum \Gamma_i x_j x_k .
\end{aligned}
$$

Hence, the maximum number of stagnation points on the x-axis (great circle) is three. Also, symmetry requires an equal number of stagnation points in the upper and lower half planes. Further, from Proposition 4.3, the maximum number of saddles and centers are two and three respectively. All 1 and 2 saddle primitives can satisfy these conditions and thus are topologies that can occur. However, among the 3-saddle primitives, the $(2,2,0)$ primitives and one homotope of a $(3,0,1)$ primitive (indicated by a * in figure 4.7) violate one or more of these conditions and so constitute topologies that cannot occur when the vortices are on a great circle and in particular for fixed equilibria and great circle relative equilibria.

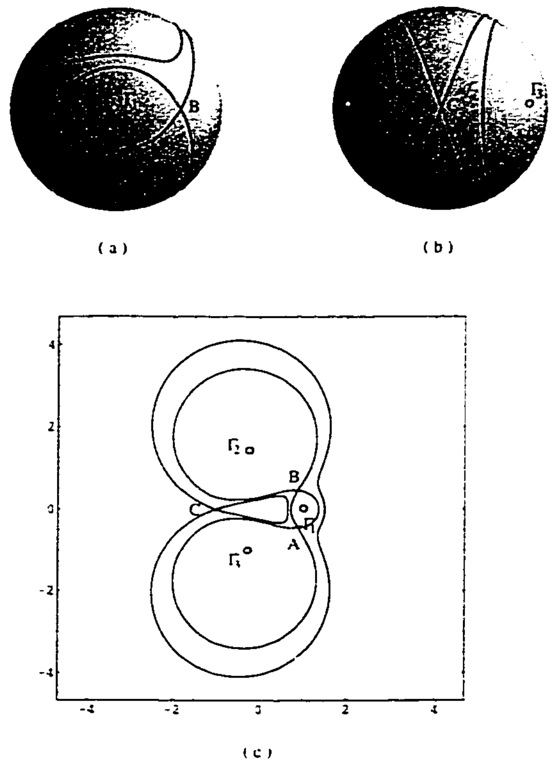

Figure 4.10: Fixed equilibrium on the equator. (a) Front of sphere; (b) Back of sphere; (c) Stereographic projection.

4.3.4 Other patterns

In this section we show the streamline patterns for two dynamical states that are not in equilibrium. Figure 4.12 shows the streamline topologies for a collapsing state (cf. Chapter 3) at three different times. As the vortices spiral in towards the collapse point at the tip of the center of vorticity vector, the streamline pattern retains the same topology throughout. Figure 4.13, on the other hand, shows streamlines for the special periodic solution that was computed in §2.5. For this solution, there is one bifurcation in the streamline topology during the course of one period, as seen by comparing figure 4.13(a) and figure 4.13(c). In more general problems, of course one would expect many more dynamical bifurcations to occur.

4.4 Rotating frames

When the vortices are in relative equilibrium, they rotate rigidly about their center of vorticity vector, c, with a fixed angular velocity ω ($||\omega|| \equiv \omega$)(cf. §2.3). In this section, we study the

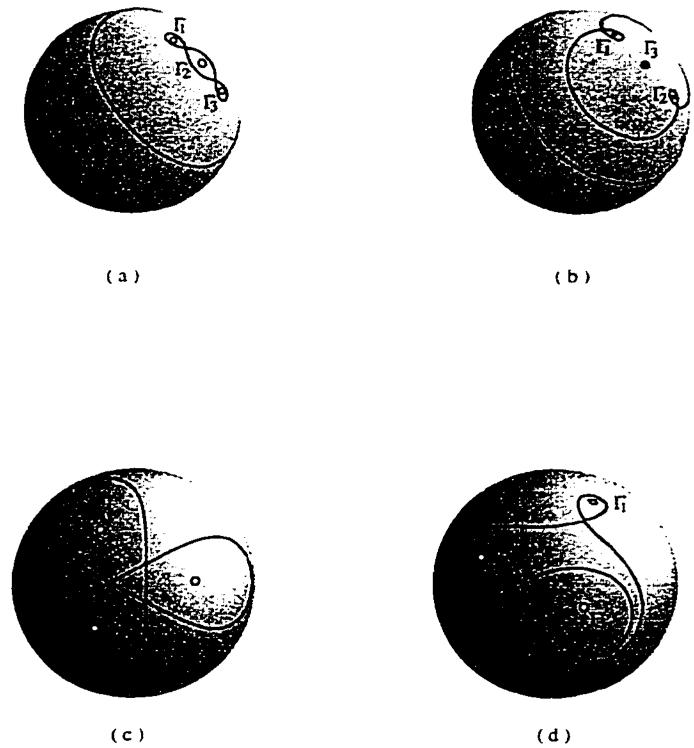

Figure 4.11: Four relative equilibria exhibiting distinct topologies. (a) Great circle state; (b) Great circle state; (c) Non- great circle state, fixed latitude equilateral triangle; (d) Non- great circle equilateral triangle state.

streamline patterns in a frame that is co-rotating at the same angular velocity, so that the vortices are stationary and the flow is steady.

If we designate the coordinates in this rotating frame (Θ, Φ), it is easy to see that they are related to the old coordinates by

$$\begin{aligned} \Theta &= \theta \\ \Phi &= \phi - \omega t. \end{aligned}$$

Implicit in this formulation is the assumption that the vortices rotate around the z axis, or equivalently around the center of vorticity vector c. The equations of motion then take the form

$$\begin{aligned} \dot{\theta} &= -\frac{1}{\sin(\theta)}\frac{\partial \mathcal{H}}{\partial \Phi} \\ \dot{\Phi} &= \frac{1}{\sin(\theta)}\frac{\partial \mathcal{H}}{\partial \theta}, \end{aligned}$$

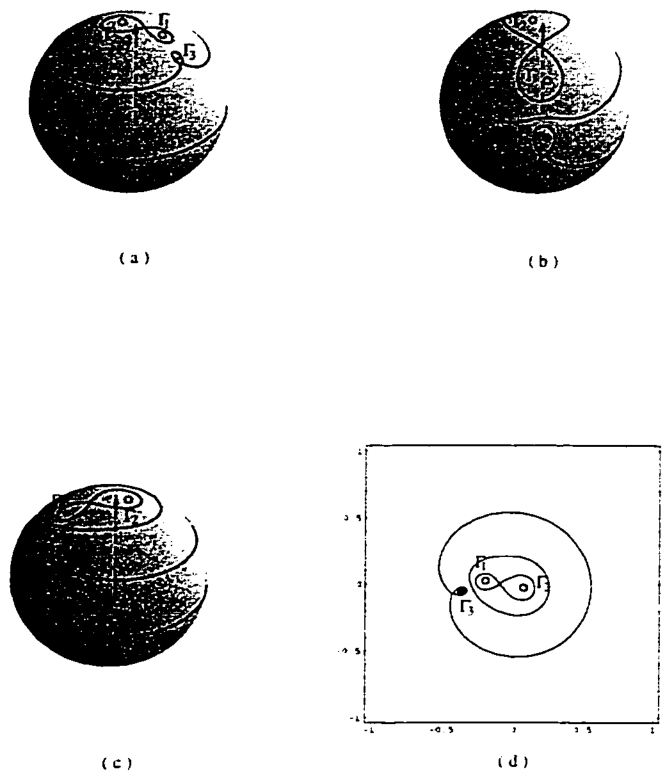

Figure 4.12: Collapsing state shown at three different times. t^* is the collapse time. Note that the topology does not change during collapse. (a) $t = 0$; (b) $t = .5t^*$; (c) $t = .9t^*$; (d) Stereographic projection of state (c).

where

$$\begin{aligned} \mathcal{H} &= \frac{1}{4\pi R^2}\left[\sum \Gamma_i \log(l_i^2) + \mu \cos^2(\frac{\theta}{2})\right] \\ \mu &= 8\pi R^2 \omega, \end{aligned}$$

with l_i being the distance between a fluid particle at (θ, ϕ) and the vortex Γ_i. In the complex plane, the equations of motion are equivalent to (4.2),(4.3), but with the Hamiltonian $\mathcal{H}$ given by

$$\mathcal{H} = \frac{1}{4\pi R^2}\left[\sum \Gamma_i \log\left(\frac{||z - z_i||^2}{(1 + ||z||^2)(1 + ||z_i||^2)}\right) + \frac{\mu}{1 + ||z||^2}\right].$$

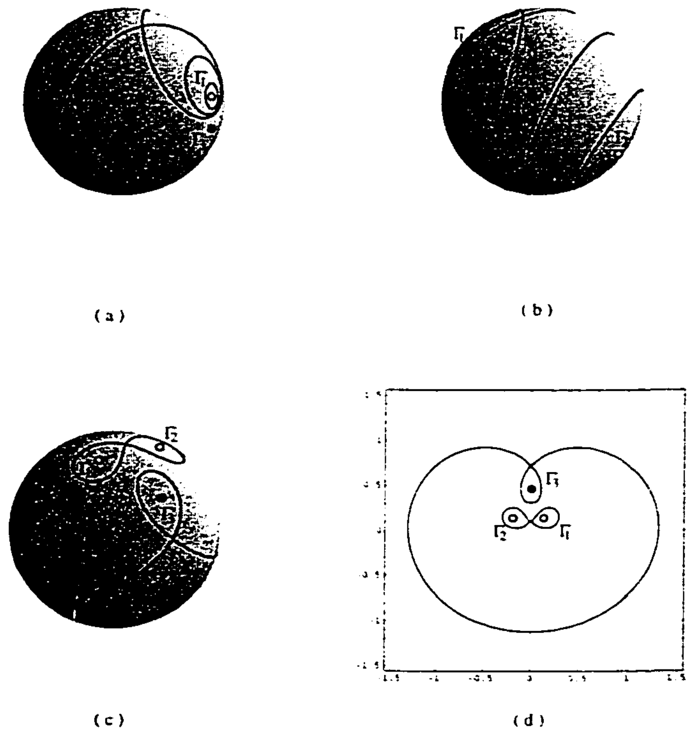

Figure 4.13: Special periodic solution exhibiting a single topological bifurcation through one period, T. (a) Front of sphere; (b) Back of sphere; (c) Time $t = T/4$; (d) Stereographic projection of (c).

The stagnation points are again given by solutions of $\dot{z}^* = 0$, or equivalently $\frac{\partial \mathcal{H}}{\partial z} = 0$. Using the above Hamiltonian, we see that the stagnation points are solutions to

$$\sum \frac{\Gamma_i}{z - z_i} - \frac{\sigma z^*}{1 + ||z||^2} = \frac{\mu z^*}{(1 + ||z||^2)^2}. \tag{4.18}$$

Notice that (4.18) is similar to (4.7), with an additional term.

It is useful to write the governing equations in vector form as well. Since the stagnation points in the rotating frame are precisely those points at which the fluid particles rotate with angular velocity ω, these points, denoted $\mathbf{x}_s$, are solutions to

$$\dot{\mathbf{x}}_s = \omega \times \mathbf{x}_s = \frac{1}{2\pi R} \sum_{i=1}^{N} \frac{\Gamma_i \mathbf{x}_i \times \mathbf{x}_s}{l_i^2}. \tag{4.19}$$

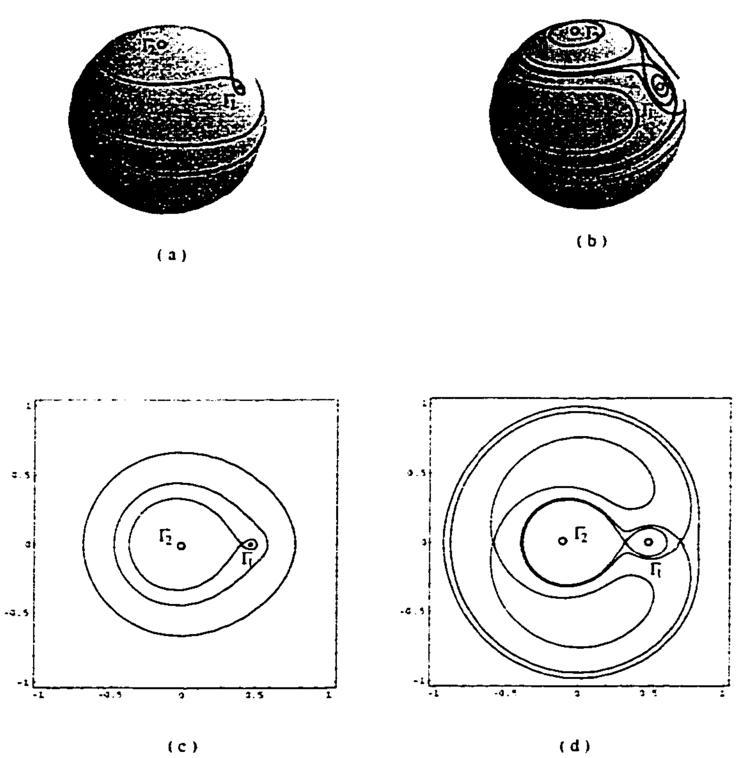

Figure 4.14: Two vortex streamline pattern. (a) Fixed inertial frame: (b) Rotating frame: (c) Stereographic projection of (a); (d) Stereographic projection of (b).

This can be written

$$\left[\sum_{i=1}^{N} \frac{\Gamma_i \mathbf{x}_i}{l_i^2} - 2\pi R\omega\right] \times \mathbf{x}_s = 0.$$

which implies

$$\sum_{i=1}^{N} \frac{\Gamma_i \mathbf{x}_i}{l_i^2} - 2\pi R\omega = k\mathbf{x}_s, \tag{4.20}$$

where k is a scalar. We now examine the cases $N = 2, 3$ in more detail.

4.4.1 N=2

For the case $N = 2$, it is clear that the two vortices must lie on a great circle. Since $\mathbf{c}$ must be co-planar with $\mathbf{x}_1$ and $\mathbf{x}_2$, without loss we assume that $\mathbf{c}$ is aligned with the z-axis and $\Phi = 0$ defines the plane in which the vortices lie. We note that if the vortices are of the same sign,

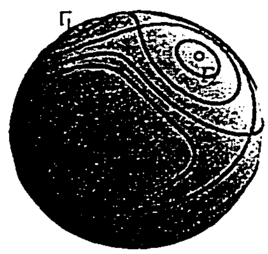

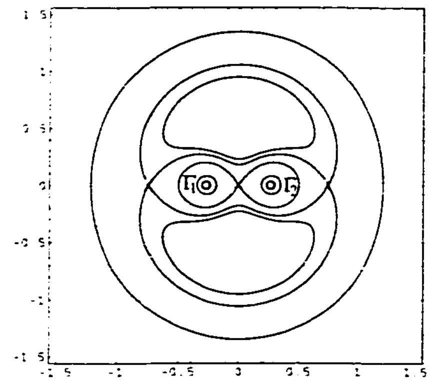

(a) (b)

Figure 4.15: Two vortex equilibrium. (a) Co-rotating frame; (b) Stereographic projection.

they lie on opposite longitudes, while if they are of opposite sign, they lie on the same longitude. Then, in the complex plane, the vortices lie on the x axis.

All two-vortex motions are rigid rotations around the center of vorticity vector **c**. The angular velocity is given by the formula

$$\omega = \frac{(\sigma^2 - \Gamma_1\Gamma_2 l^2)^{1/2}}{2l^2}.$$

Since the vortices lie on a great circle, we can categorize the stagnation points into two classes: those on the great circle and those off it. Consider first those that lie off the great circle. From (4.20), it is clear that since the three vectors $\mathbf{x}_1$. $\mathbf{x}_2$ and ω lie in the same plane, with $\mathbf{x}_s$ not lieing in that plane, then the scalar $k = 0$. From this, we have

$$\frac{\Gamma_1\mathbf{x}_1}{l_1^2} + \frac{\Gamma_2\mathbf{x}_2}{l_2^2} = \frac{\Gamma_1\mathbf{x}_1 + \Gamma_2\mathbf{x}_2}{l_{12}^2},$$

where we have used the appropriate expression for ω. This then implies that

$$\Gamma_1\mathbf{x}_1\left(\frac{1}{l_1^2} - \frac{1}{l_{12}^2}\right) + \Gamma_2\mathbf{x}_2\left(\frac{1}{l_2^2} - \frac{1}{l_{12}^2}\right) = 0,$$

which is possible only if $l_1 = l_2 = l_{12}$. Hence, the off-great-circle stagnation point lies at the third vertex of an equilateral triangle formed with the two vortices at the other vertices. Due to symmetry considerations, it is clear that there are two such stagnation points, one on either side of the great circle. A simple necessary condition for the existence of these stagnation points is that $l_{12} < \sqrt{3}R$, which is the side of the largest equilateral triangle that can be inscribed in a sphere of radius R.

(a) (b)

Figure 4.16: Two vortex equilibrium with $\Gamma_1 + \Gamma_2 = 0$. (a) Fixed frame; (b) Co-rotating frame.

To determine the stagnation points on the great circle, we need to solve (4.18). In this case, we have $z_i = x_i$ and $z = z^* = x$. Using these in (4.18) gives a quartic equation

$$Ax^4 + Bx^3 + Cx^2 + Dx + E = 0,$$

where

$$\begin{aligned} A &= \sum \Gamma_i x_i \\ B &= \sigma(1 - x_1x_2) - \mu \\ C &= A + E + \mu \sum x_i \\ D &= \sigma(1 - x_1x_2) - \mu x_1 x_2 \\ E &= -\sum \Gamma_i x_j. \end{aligned}$$

Since a quartic can have at most 4 real solutions, the maximum total number of stagnation points in a frame co-rotating with the vortices is 6 — 4 on the great circle and 2 off. Recall that in the stationary frame, the maximum number was shown to be two. We show an example of a streamline topology with six stagnation points in figure 4.14, where for comparison purposes, the streamlines in the stationary frame are shown as well. It is interesting to note that the streamlines in the stationary frame are a simple lemniscate, whereas those in the co-rotating frame form a more complex pattern consisting of a superposition of two lemniscates and one limacon. Thus, we obtain a topology for the two vortex problem in the co-rotating frame that could only be achieved with three vortices in the stationary frame. We mention also that the topology shown in figure 4.14(d) is identical to the well known 'zero-velocity' curves for a restricted three body problem, as shown for example in [99]. Another interesting example is shown in figure 4.15. In this case, the topology is a superposition of primitives (0,0,0),(2,0,0) and (0,3,0). A case with four stagnation points (two on the great circle and two off) is shown in figure 4.16(b) where the corresponding topology in the stationary frame is shown as well in figure 4.16(a). In this case, $\sigma = 0$ and we have the well known bubble topology. When $l_{12} > \sqrt{3}R$, the two stagnation points off the great circle disappear as do two of the stagnation points on the great circle. Thus, there remain two stagnation points on the great circle. Finally, we point out that we can have a configuration with no stagnation points. This can happen only when the two vortices are of opposite sign and $l_{12} > \sqrt{3}R$.

4.4.2 N=3

As categorized in §2.3, there are two types of three vortex relative equilibria: (1) Great circle equilibria, including fixed equilibrium states; (2) Non great circle equilibria. These are the equilateral triangle configurations with arbitrary vortex strengths.

We consider each of these in turn.

4.4.2.1 Great circle relative equilibria

Since the center of vorticity vector is aligned with the z axis, the vortices lie on the same longitude, or on two longitudes on opposite sides of the sphere. We choose these to be the longitudes marked 0 and π. The sides of the vortex triangle and the vortex strengths must satisfy $\dot{V} = 0$ (cf. Prop. 2.2) and the rotation frequencies ω, (2.16). We now look for stagnation points in a frame co-rotating with these vortices.

As in the two vortex case, the stagnation points can again be classified into great circle and non-great circle types. The latter can be located by using the vector form of the equations (4.20), with $k = 0$. Since the three vectors $\mathbf{x}_i$ and the angular frequency vector ω are co-planar, we can write two of these vectors in terms of the other two (say $\mathbf{x}_1$ and $\mathbf{x}_2$), so that (4.20) becomes

$$a_1\mathbf{x}_1 + a_2\mathbf{x}_2 = 0, \tag{4.21}$$

where a_1 and a_2 are scalar functions of the vortex strengths and positions. From this, we can conclude that $a_1 = 0$ and $a_2 = 0$. This yields:

$$\begin{aligned} a_1 &= \frac{\Gamma_1}{l_1^2} + \frac{\Gamma_3 u}{l_3^2} - w_1 = 0 \\ a_2 &= \frac{\Gamma_2}{l_2^2} + \frac{\Gamma_3 v}{l_3^2} - w_2 = 0, \end{aligned}$$

where

$$\begin{aligned} \mathbf{x}_3 &= u\mathbf{x}_1 + v\mathbf{x}_2 \\ 2\pi R\mathbf{w} &= w_1\mathbf{x}_1 + w_2\mathbf{x}_2 \\ l_i^2 &= 2[R^2 - xx_i - zz_i] \end{aligned}$$

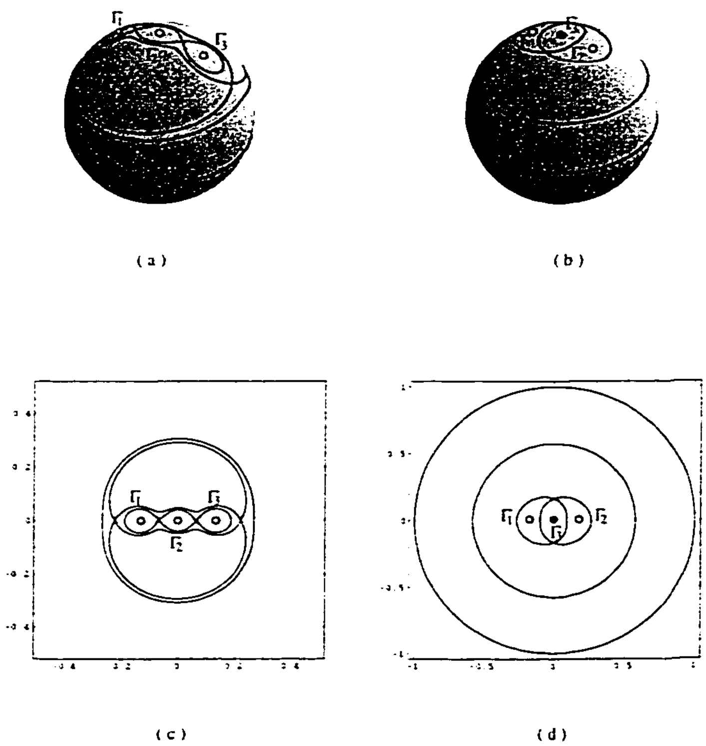

Figure 4.17: (a) A seven stagnation point topology in the co-rotating frame. The topology is a combination of primitives (0,0,0), (2,1,0) and (0,3,0). The same configuration, in an inertial frame, was shown in figure 4.11(a); (b) Three stagnation point topology in a co-rotating frame. The same configuration in an inertial frame was shown in figure 4.11(b); (c) Stereographic projection of (a); (d) Stereographic projection of (b).

must be solved numerically.

For the great circle stagnation points, we can use $z_i = x_i$ and $z = x$, in which case (4.18) takes the form of a quintic

$$Ax^5 + Bx^4 + Cx^3 + Dx^2 + Ex + F = 0,$$

where

$$\begin{aligned}
A &= \sigma \sum x_i - \sum \Gamma_i (x_j + x_k) \\
B &= \sum \Gamma_i x_j x_k - \mu + \sigma (1 - \sum x_i x_j) \\
C &= \sigma \sum x_i - 2 \sum \Gamma_i (x_j + x_k) + (\sigma + \mu) x_1 x_2 x_3 \\
D &= 2 \sum \Gamma_i x_j x_k + \sigma - (\sigma + \mu) \sum x_i x_j
\end{aligned}$$

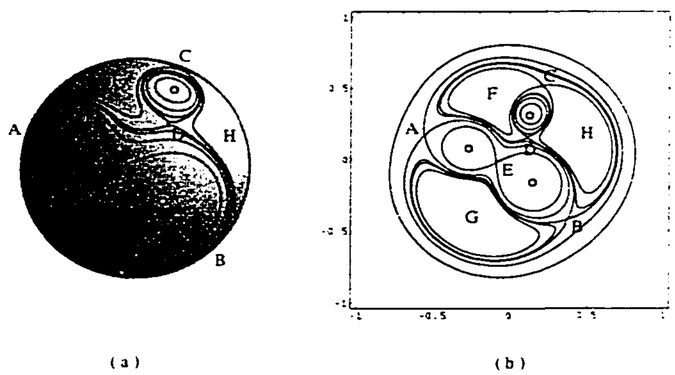

Figure 4.18: (a) The configuration of figure 4.11(d) in a co-rotating frame. In this frame there are 9 stagnation points — 5 saddles and 4 centers; (b) Stereographic projection of (a).

$$E = (\sigma+\mu)x_1x_2x_3 - \sum \Gamma_i(x_j + x_k)$$
$$F = \sum \Gamma_i x_j x_k.$$

There can be a maximum of 5 real solutions to the quintic. Figure 4.17(a) shows an example of a 7 stagnation point topology in the rotating frame — 5 on the great circle and 2 off. The structure is a superposition of primitives (0,0,0), (2,1,0), and (0,3,0). The same configuration in an inertial frame was shown in figure 4.11(a). Figure 4.17(b) shows the topology of figure 4.11(b) in the co-rotating frame. In this frame there are three stagnation points.

4.4.2.2 Non-great circle relative equilibria

In the most general case, the vortices lie on different latitudes and form an equilateral triangle. They rotate around the center of vorticity vector with angular velocity given by (cf. §2.3)

$$\omega = \frac{(\sigma^2R^2 - l^2\sum\Gamma_i\Gamma_j)^{1/2}}{2\pi R l^2}.$$

To obtain the stagnation points in the co-rotating frame, one has to solve (4.18). In general this must be done numerically. We examine the topologies of figure 4.11(c) and 4.11(d) in the co-rotating frame. The topology of figure 4.11(c) is maintained in the co-rotating frame. The topology of 4.11(d), on the other hand, appears as shown in figure 4.18 when seen in the co-rotating frame. Figure 4.18(a) shows the topology looking down on the sphere; figure 4.18(b) is the stereographic projection. There are five saddles, marked by A,B,C,D, and E, and four centers marked F,G, and H, with the last on the far side so is not visible, to give a total of nine stagnation points. The topology is a nested structure with lemniscates and limacons inside one another.

Shown in figure 4.19 is the topology for another equilateral configuration in the co-rotating frame, this time with $\sigma = 0$ ($\Gamma_1 = 1$, $\Gamma_2 = \Gamma_3 = -1/2$). This configuration is a 'limiting super-radial state' (cf. §2.2.2) such that the moment of vorticity vector $\mathbf{M}$ is perpendicular to $\hat{\mathbf{n}}$, the vector normal to the vortex plane. Also, by the stability criterion of [79], this is an unstable state as $\sum \Gamma_i \Gamma_j < 0$. In the co-rotating frame, we see the familiar bubble topology. There are three saddles and two centers. In the inertial frame (not shown), there is just one saddle, and it lies on the vortex circle as stipulated in Proposition 4.1. It is interesting that even in the two vortex case, for $\sigma = 0$, we have a bubble type topology in the co-rotating frame (figure 4.16). The dynamics of dipoles and tripoles (2 and 3 vortex clusters with $\sigma = 0$) has been the subject of numerous recent studies. ([25], [83])

4.5 Conclusion

One of the main goals of this chapter has been to identify and classify all of the possible instantaneous streamline patterns on a sphere that are obtainable from integrable point vortex motion. The 12 primitive topologies, along with their 23 additional homotopic equivalents form the building blocks for all global integrable streamline patterns achievable on a sphere. These integrable templates can be used as a first step in performing a Melnikov analysis if one wanted to induce chaotic motion on the sphere under appropriate perturbations. An example of this was recently published [12]. One might then reasonably ask the following questions:

- How representative are these patterns for more general flows?
- How do these topologies evolve dynamically? In particular, can one identify the bifurcations that occur on the spherical surface as the patterns evolve?
- What role do the bifurcations of patterns and the evolution of instantaneous streamline structures play in the mixing and transport of Lagrangian particles and the stretching of passive interfaces?

While we do not yet have an answer to the first question, we do have indications that these patterns, along with the additional patterns produced by the integrable four vortex problem obtained under the restriction $\mathbf{c} = 0$, do cover many of the structures one finds in much more complex flows. For example, one can find a picture of spherical instantaneous streamline patterns in Gill [40], figure 2.3. We have decomposed this figure into 10 connected components and can show that the topology requires a minimum of 7 vortices to produce such a field. Nonetheless, despite the fact that at least 7 isolated vortices are required to produce this instantaneous flow, the vast majority of topological structures in this figure are contained in our primitive chart for the three vortex problem.

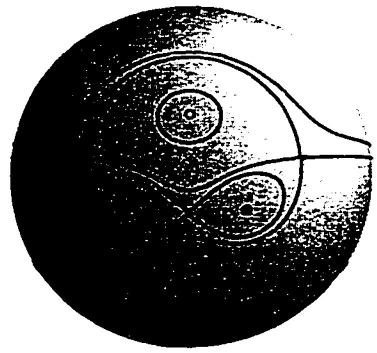

Figure 4.19: Equilateral configuration in a co-rotating frame. $\sigma = 0$. There are 3 saddles and 2 centers.

The second question is clearly connected to the issue of structural stability of the flow under its natural dynamics. In general, to understand this second question for any reasonably complex flowfield will require extensive numerical computations together with more sophisticated visualization techniques. This is also related to the third question, which has also not yet been sufficiently explored. A much more restricted analysis of this type was initiated in Meiburg, Newton, Raju, and Ruetsch [64] for a two dimensional shear layer model. For this problem, a topological bifurcation was first identified in a model flow made up of point vortices, then verified that it persisted in a direct numerical Navier-Stokes simulation. This was followed by a computation of Lyapunov exponents associated with the evolving interface in cases for which the bifurcation occured, and compared with cases where it did not occur.

It is our opinion that a better understanding of global weather patterns will involve a deeper analysis of the interplay between topology and dynamics of the streamline patterns produced by the flow. The dynamical transition from one topology to another is probably an underappreciated *global instability* mechanism of enhanced atmospheric mixing in the fully nonlinear regime and is certainly worthy of further investigation.

Chapter 5

Motion in domains with boundaries

In this chapter, we study particle and vortex motion in a simply connected domain D on the sphere. This problem differs from the ones considered earlier for three reasons :

1) On the boundary, ∂D, the condition of no fluid penetration has to be satisfied.

2) Because of the presence of the boundary, the constraint $\int \omega dA = 0$ no longer holds.

3) The presence of boundaries can break symmetries that would otherwise exist, reducing the number of conserved quantities. Since the latter are related to conservation laws, as few as two vortices could exhibit non - integrable motion in a suitable domain.

First, we write the governing equations for N vortices in an arbitrary simply connected domain D. We then cast the problem in terms of the Green's function of the first kind. In the next section, we consider the motion in D' which is the projection of D onto the stereographic plane. For several special symmetric domains, we describe a method that uses known image vortex solutions for the planar vortex problem to construct similar solutions to the problem in the stereographic plane and hence in D. In particular, we present the Hamiltonians H_p and H_v, for the particle and vortex motions respectively. In the last section, we show examples of several domains D that are amenable to solution by this method. The streamlines and paths of an isolated vortex are shown for these domains. A general study of the scope of the planar image method was carried out by Keller [51]. The analogous spherical problem apparently has not been studied systematically.

5.1 Governing Equation

Consider the flow due to N point vortices of strengths Γ_i and located at $(\theta_i, \phi_i) \in D$, $1 \leq i \leq N$. The flow is described by a stream-function ψ which is a solution to

$$\begin{aligned} \Delta\psi &= -\sum_{\alpha=1}^{N} \Gamma_\alpha \delta(\theta, \phi, \theta_\alpha, \phi_\alpha) \ \in \ D \\ \psi &= 0 \ \in \ \partial D \end{aligned} \tag{5.1}$$

The Green's function G for a single source can be written as $G = G_1 + G_2$ where G_1 is the Green's function for the sphere with no solid boundary [52]

$$G_1(\theta, \phi, \theta_\alpha, \phi_\alpha) = -\frac{1}{4\pi}\ln(1 - \cos\theta\cos\theta_\alpha - \sin\theta\sin\theta_\alpha\cos(\phi - \phi_\alpha))$$

such that

$$\Delta G_1 = -\delta(\theta, \phi, \theta_\alpha, \phi_\alpha) + \frac{1}{4\pi R^2}$$

G_2 satisfies

$$\begin{aligned} \Delta G_2 &= -\frac{1}{4\pi R^2} \in D \\ G_2 &= -G_1 \\ &= \frac{1}{4\pi}\ln(1 - \cos\theta\cos\theta_\alpha - \sin\theta\sin\theta_\alpha\cos(\phi - \phi_\alpha)), (\theta, \phi) \in \partial D \end{aligned} \tag{5.2}$$

The Green's function for N sources located at $(\theta_\alpha, \phi_\alpha) \in D$ is given by linear superposition :

$$\begin{aligned} G^{(N)}(\theta, \phi; \theta_1, \phi_1, ..., \theta_N, \phi_N) &= \sum_{\alpha=1}^{N} G(\theta, \phi; \theta_\alpha, \phi_i\alpha) \\ &= \sum_{\alpha=1}^{N} G_1(\theta, \phi; \theta_\alpha, \phi_\alpha) + \sum_{\alpha=1}^{N} G_2(\theta, \phi; \theta_\alpha, \phi_\alpha) \end{aligned} \tag{5.3}$$

ψ is then obtained by $\psi = \sum_{\alpha=1}^{N} \Gamma_\alpha G(\theta, \phi; \theta_\alpha, \phi_\alpha)$.
The stream-function generates a Hamiltonian vectorfield in the usual way :

$$\begin{aligned} \dot{\theta} &= \frac{1}{R^2\sin\theta}\frac{\partial\psi}{\partial\phi}, \\ \dot{\phi} &= -\frac{1}{R^2\sin\theta}\frac{\partial\psi}{\partial\theta}. \end{aligned}$$

We define the particle Hamiltonian as $H_p = -\frac{\psi}{R^2}$ so that the above equations are in standard Hamiltonian form with conjugate variables $P \equiv \cos\theta$ and $Q \equiv \phi$:

$$\begin{aligned} \dot{P} &= \frac{\partial H_p}{\partial Q}, \\ \dot{Q} &= -\frac{\partial H_p}{\partial P}. \end{aligned}$$

The motion of the ith vortex is given by similar equations with the vortex Hamiltonian, H_v in place of H_p and conjugate variables $P_i \equiv \cos\theta_i$, $Q_i \equiv \phi_i$.

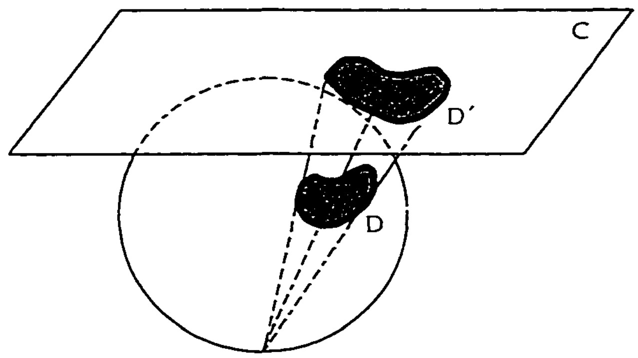

Figure 5.1: Stereographic projection of domain D to domain D' in the complex plane.

5.2 Method of Images

For domains with special symmetries, H_p and H_v can be constructed using the method of images. In this section, we describe a method that uses known image vortex systems for the planar vortex problem to solve the problem in the stereographic plane and hence in D.

Consider the problem analogous to (5.1) for the motion generated by N planar vortices,in a domain D', where D' is the stereographic projection of D onto the complex plane (figure 5.1). The stream-function, $\tilde{\psi}$ in this case is given by

$$\begin{aligned} \Delta\tilde{\psi} &= -\sum_{\alpha=1}^{N} \Gamma_\alpha \delta(x, y, x_\alpha, y_\alpha) \ \in \ D' \\ \tilde{\psi} &= 0 \ on \ \partial D' \end{aligned} \tag{5.4}$$

It will be shown below that if this problem can be solved by the method of images, then this system of images would also solve (5.1). For this, we recall the forms of H_p and H_v for the motion of M vortices γ_α, $1 \leq \alpha \leq M$, in the stereographic plane :

$$\begin{aligned} H_p &= \frac{1}{4\pi R^2}\sum_{\alpha=1}^{M} \gamma_\alpha \ln \frac{|z-z_\alpha|^2}{(1+|z|^2)(1+|z_\alpha|^2)}, \\ H_v &= \frac{1}{4\pi R^2}\sum_{\alpha<\beta} \gamma_\alpha\gamma_\beta \ln \frac{|z_\alpha-z_\beta|^2}{(1+|z_\alpha|^2)(1+|z_\beta|^2)}. \end{aligned} \tag{5.5}$$

The corresponding equations of particle and vortex motions are given by

$$\begin{aligned}
\dot{z}^{*} &= -i\frac{(1+r^2)^2}{8\pi R^2}\Big[\sum_{\alpha=1}^{M}\frac{\gamma_\alpha}{z-z_\alpha}-\frac{\sigma z^{*}}{1+|z|^2}\Big],\\
\dot{z}_\alpha^{*} &= -i\frac{(1+r_\alpha^2)^2}{8\pi R^2}\Big[\sum_{\beta=1}^{M'}\frac{\gamma_\beta}{z_\alpha-z_\beta}-\frac{(\sigma-\gamma_\alpha)z_\alpha^{*}}{1+|z_\alpha|^2}\Big].
\end{aligned}\tag{5.6}$$

Also consider the motion of M planar vortices with particle and vortex Hamiltonians given by the familiar

$$\begin{aligned}
\hat{H} &= -\frac{1}{2\pi}\sum_{\alpha=1}^{M}\gamma_\alpha \ln|z-z_\alpha|,\\
\hat{H}_v &= -\frac{1}{2\pi}\sum_{\alpha<\beta}\gamma_\alpha\gamma_\beta \ln|z_\alpha-z_\beta|.
\end{aligned}\tag{5.7}$$

The corresponding equations of motion given by

$$\begin{aligned}
\dot{z}^{*} &= -\frac{i}{2\pi}\sum_{\alpha=1}^{M}\frac{\gamma_\alpha}{z-z_\alpha},\\
\dot{z}_\alpha^{*} &= -\frac{i}{2\pi}\sum_{\beta=1}^{M'}\frac{\gamma_\beta}{z_\alpha-z_\beta}.
\end{aligned}\tag{5.8}$$

We now establish the following lemmas -

Lemma 5.1. *Let D' be a domain for which (5.4) can be solved by the method of images. Then $\sum_{\alpha=1}^{M}\gamma_\alpha = 0$ where γ_α, $1 \le \alpha \le N$ are the N vortices and the rest (M - N) are image vortices.*

To prove this, we need only consider the case of a single vortex of strength Γ i.e. $N = 1$. By the Riemann Mapping Theorem, $\exists\ \zeta = f(z)$ such that any domain D' can be analytically mapped to the upper half plane (UHP). The complex potential transforms as $w(\zeta) = w(f(z))$ which implies $\psi(\zeta) = \psi(f(z))$. Now, the image system in the UHP consists of just one vortex with strength $-\Gamma$ located at ζ_v^* where ζ_v locates the vortex in the UHP and so

$$\psi(\zeta) = -\frac{\Gamma}{2\pi}\ln\Big|\frac{\zeta-\zeta_v}{\zeta-\zeta_v^*}\Big|.$$

Expressing $\zeta = f(z)$, we see that

$$\hat{\psi}(z) = -\frac{\Gamma}{2\pi}\ln\Big|\frac{f(z)-f(z_v)}{f(z)-f^*(z_v)}\Big|.\tag{5.9}$$

Since we have assumed that (5.4) can be solved by the method of images, it necessarily follows that

$$\begin{aligned} f(z) - f(z_v) &= (z - z_v)(z - z_{+1})(z - z_{+2}) \cdots (z - z_{+q}) \\ f(z) - f^*(z_v) &= (z - z_{-1})(z - z_{-2}) \cdots (z - z_{-(q+1)}) \end{aligned} \tag{5.10}$$

where z_{+n} and z_{-n} locate the n^{th} positive and negative image vortices respectively and $q = \frac{M}{2} - 1$. Thus, $\hat{\psi}$ is a linear superposition of ψ's due to equal numbers of positive vortices (strength $+\Gamma$) and negative vortices (strength $-\Gamma$) which implies $\sigma = 0$.

Remark For certain D', M could be infinite with the sets of positive and negative vortices, P and N, both countably infinite. Let P_m and N_m be the m^{th} subsets of P and N i.e their elements are the first m positive and the first m negative vortices respectively. In this case, we define

$$\sigma = \lim_{m \to \infty} \sum_{i=1}^{m} (p_i + n_i)$$

where $p_i \in P_m, n_i \in N_m$ so that again $\sigma = 0$. An example of such a domain is an infinite strip bounded by y=0 and y=h.

Lemma 5.2. *Let I be the system of M point vortices of strengths γ_α, such that $\sum_{\alpha=1}^{M} \gamma_\alpha = 0$ and located at (x_α, y_α), in the stereographic plane and II be an identical planar system. Then I and II have the same streamlines.*

(5.8) in component form is

$$\begin{aligned} \dot{x} &= -\frac{1}{2\pi} \sum_{\alpha=1}^{M} \frac{\gamma_\alpha (y - y_\alpha)}{(x - x_\alpha)^2 + (y - y_\alpha)^2} \equiv \frac{A}{2\pi}, \\ \dot{y} &= \frac{1}{2\pi} \sum_{\alpha=1}^{M} \frac{\gamma_\alpha (x - x_\alpha)}{(x - x_\alpha)^2 + (y - y_\alpha)^2} \equiv \frac{B}{2\pi}. \end{aligned}$$

The streamlines are given by

$$\frac{dy}{dx} = \frac{B}{A}. \tag{5.11}$$

In the stereographic plane, the particle velocity is given by (5.6a). Since, by assumption, $\sigma = 0$, (5.6a) gives

$$\dot{z}^* = -i \frac{(1 + |z|^2)^2}{8\pi R^2} \sum_{\alpha=1}^{M} \frac{\gamma_\alpha}{z - z_\alpha}$$

which in component form is

$$\dot{x} = -\frac{(1+x^2+y^2)^2}{8\pi R^2}\sum_{\alpha=1}^{M}\frac{\gamma_\alpha(y-y_\alpha)}{(x-x_\alpha)^2+(y-y_\alpha)^2},$$

$$\dot{y} = \frac{(x^2+y^2+1)^2}{8\pi R^2}\sum_{\alpha=1}^{M}\frac{\gamma_\alpha(x-x_\alpha)}{(x-x_\alpha)^2+(y-y_\alpha)^2}.$$

Streamlines in this case are given by $\frac{dy}{dx} = \frac{B}{A}$ i.e. exactly by (5.11). Thus, if $\sigma = 0$, the streamlines in the planar and stereographic flows are identical for identical vortex positions.

Hence, given a domain D on the sphere and one vortex of strength Γ located at $(\theta_v, \phi_v) \in D$. the particle and vortex Hamiltonians, H_p and H_v are calculated as follows :

1) Map D stereographically to D'. (θ_v, ϕ_v) maps to (r_v, ϕ_v).

2) Consider the identical problem for planar vortex motion in D' which we assume can be solved by the method of images. From (5.9),

$$|\frac{f(z)-f(z_v)}{f(z)-f^*(z_v)}| = const. \tag{5.12}$$

gives the streamlines. Here, $z = re^{i\phi}$ and $\zeta = f(z)$ maps D' to the UHP.

3) By Lemma 5.2, (5.12) describes the streamlines in the stereographic plane as well. Hence, taking into account (5.5), the particle Hamiltonian. H_p is given by

$$H_p = \frac{\Gamma}{4\pi R^2}\ln|\frac{f(z)-f(z_v)}{f(z)-f^*(z_v)}|^2 \tag{5.13}$$

4) To get the Hamiltonian for the vortex motion, we use (5.5b) with the positive image vortices located at $z_{+\alpha}, 1 \le \alpha \le q$ and the negative ones at $z_{-\beta}, 1 \le \beta \le (q+1)$. Thus, we get

$$H_v = \frac{\Gamma^2}{4\pi R^2}[\lim_{z\to z_v}\ln|\frac{f(z)-f(z_v)}{(z-z_v)}|^2|\frac{1}{f(z)-f^*(z_v)}|^2 + \ln\frac{(1+|z_v|^2)(1+|z_{-1}|^2)\cdots(1+|z_{-(q+1)}|^2)}{(1+|z_{+1}|^2)(1+|z_{+2}|^2)\cdots(1+|z_{+q}|^2)}]$$

which yields

$$H_v = \frac{\Gamma^2}{4\pi R^2}[\ln|\frac{df}{dz}|^2_{z=z_v}|\frac{1}{f(z)-f^*(z_v)}|^2 + \ln\frac{(1+|z_v|^2)(1+|z_{-1}|^2)\cdots(1+|z_{-(q+1)}|^2)}{(1+|z_{+1}|^2)(1+|z_{+2}|^2)\cdots(1+|z_{+q}|^2)}] \tag{5.14}$$

5.2.1 Solvable Domains

We now present H_p and H_v for several domains. In the following discussion, a vortex of strength Γ is located at $(\theta_v, \phi_v) \in D$.

(a) (b)

Figure 5.2: Vortex motion in a circular cap. (a) Instantaneous streamlines for $\theta_v = 30^0, \phi_v = 270^0$. (b) Vortex paths are constant latitudes.

Example 1 : Spherical cap. D is the spherical cap bounded by the latitude $\theta = \theta_0$. D', the stereographic projection of D, is the disk of radius $r_0 = \tan\frac{\theta_0}{2}$. The image system consists of just one vortex. $-\Gamma$ at the inverse point $r_i = \frac{r_0^2}{r_v}, \phi_i = \phi_v$. Hence,

$$\begin{aligned} H_p &= \frac{\Gamma}{4\pi R^2}\ln|\frac{z-z_v}{z-z_i}|^2 \\ &= \frac{\Gamma}{4\pi R^2}\ln\frac{(r^2-2rr_v\cos(\phi-\phi_v)+r_v^2)r_v^2}{r^2r_v^2-2rr_vr_0^2\cos(\phi-\phi_v)+r_0^4} \end{aligned}$$

The streamlines are given by

$$\frac{(r^2-2rr_v\cos(\phi-\phi_v)+r_v^2)}{r^2r_v^2-2rr_vr_0^2\cos(\phi-\phi_v)+r_0^4} = const.$$

A few representative streamlines are plotted in figure 5.2(a) for $\theta_0 = 60^0, \theta_v = 30^0, \phi_v = 270^0$. H_v is easily calculated as

$$H_v = \frac{\Gamma^2}{4\pi R^2}\ln\frac{(1+|z_v|^2)(1+|z_i|^2)}{|z_v-z_i|^2}$$

and so the vortex paths are given by

$$\frac{(1+r^2)(r^2+r_0^4)}{(r_0^2-r^2)^2} = const.$$

Vortex paths for different initial conditions (θ_v, ϕ_v) are shown in figure 5.2(b). In the stereographic plane, the paths are circles centered at the origin, while on the sphere they are fixed latitudes.

Example2 : **Sector.** D is the sector bounded by the longitudes 0 and π/m, $m \in N$. D' is a wedge of angle π/m. Since $f(z) = z^m$ maps D' to the UHP, by (5.13),

$$H_p = \frac{\Gamma}{4\pi R^2} \ln |\frac{z^m - z_v^m}{z^m - z_v^{*m}}|^2.$$

It is not difficult to see that there are 2m - 1 image vortices, with the positive vortices located at $z_{+\alpha} = z_v e^{i2\pi\alpha/m}$, $1 \leq \alpha \leq m-1$ and the negative ones at $z_{-\beta} = z_v^* e^{i2\pi\beta/m}$, $1 \leq \beta \leq m$. The streamlines are given by

$$\frac{r^{2m} - 2r^m r_v^m \cos m(\phi - \phi_v) + r_v^{2m}}{r^{2m} - 2r^m r_v^m \cos m(\phi + \phi_v) + r_v^{2m}} = const.$$

Figure 5.3(a) shows a few streamlines for $m = 3$ and $\theta_v = \phi_v = 45^0$. The vortex Hamiltonian,using (5.14), is

$$H_v = \frac{\Gamma^2}{4\pi R^2} \ln \frac{m^2 |z_v|^{2m-2} (1 + |z_v|^2)^2}{|z_v^m - z_v^{*m}|^2},$$

and so the vortex paths are given by

$$\frac{(1 + r^2)^2}{r^2 \sin^2 m\phi} = const.$$

Vortex paths for different initial positions (θ_v, ϕ_v) are shown in figure 5.3(b) while the stereographic projection of the paths is shown in figure 5.3(c). Though the streamlines of the stereographic and planar vortex flows are the same, the vortex paths are not. To illustrate this, we plot the planar vortex paths in a wedge in figure 5.3(d), for the same initial positions that were shown in 5.3(c); the paths are closed in the spherical domain whereas in the planar wedge, they are open.

Example 3 : **Half sector.** D is the half-sector bounded by longitudes 0, $\pi/m, m \in N$ and the equator. D' is the sector of a circle. $f(z) = (\frac{1+z^m}{1-z^m})^2$ maps the sector to the UHP and so

$$H_p = \frac{\Gamma}{4\pi R^2} \ln |\frac{(\frac{1+z^m}{1-z^m})^2 - (\frac{1+z_v^m}{1-z_v^m})^2}{(\frac{1+z^m}{1-z^m})^2 - (\frac{1+z_v^{*m}}{1-z_v^{*m}})^2}|^2.$$

Streamlines are given by

$$\frac{[r^{2m} - 2r^m r_v^m \cos m(\phi - \phi_v) + r_v^{2m}][r^{2m} r_v^{2m} - 2r^m r_v^m \cos m(\phi + \phi_v) + 1]}{[r^{2m} - 2r^m r_v^m \cos m(\phi + \phi_v) + r_v^{2m}][r^{2m} r_v^{2m} - 2r^m r_v^m \cos m(\phi - \phi_v) + 1]} = const.$$

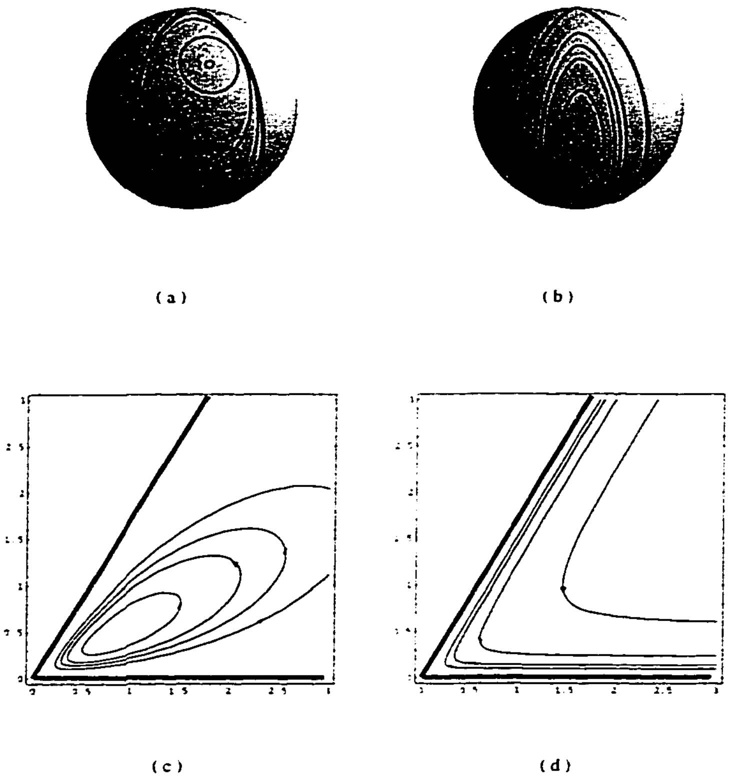

Figure 5.3: Vortex motion in a sector. (a) Instantaneous streamlines for $\theta_v = 45^0, \phi_v = 45^0$. (b) Vortex paths on the sphere. (c) Stereographic projection of vortex paths. (d) Vortex paths in a planar domain.

There are 4 m - 1 image vortices located as follows : (m - 1) positive vortices at $z_{+\alpha} = z_v e^{i2\pi\alpha/m}$, $1 \le \alpha \le m-1$, m positive vortices at $z_{+\beta} = \frac{1}{z_v} e^{i2\pi\beta/m}$, $1 \le \beta \le m$, m negative vortices at $z_{-\alpha} = z_v^* e^{i2\pi\alpha/m}$, $1 \le \alpha \le m$ and m negative vortices at $z_{-\beta} = \frac{1}{z_v^*} e^{i2\pi\beta/m}$, $1 \le \beta \le m$. The image system for m = 2 is shown in figure 5.4(a). Figure 5.4(b) shows a few streamlines for $\theta_v = 45^0$, $\phi_v = 60^0$.

To get the vortex Hamiltonian, we first compute

$$|\frac{df}{dz}|_{z=z_v} = \frac{4m|z_v|^{m-1}|z_v^m + 1|}{|(1-z_v^m)^3|}.$$

Using (5.14) we get

$$H_v = \frac{\Gamma^2}{4\pi R^2} \ln \frac{16m^2|z_v|^{2m-2}|z_v^m+1|^2}{|(1-z_v^m)^3|^2} \frac{(1+|z_v|^2)^2}{|(\frac{1+z_v^m}{1-z_v^m})^2 - (\frac{1+z_v^{*m}}{1-z_v^{*m}})^2|^2}$$

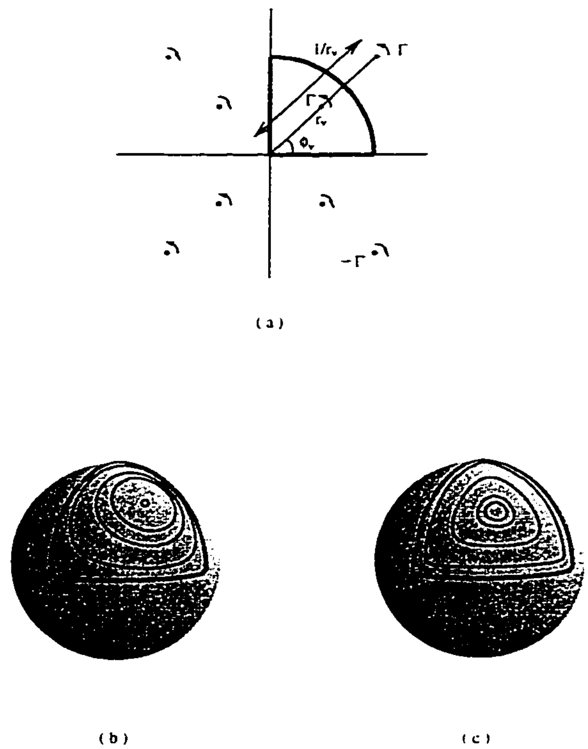

Figure 5.4: Vortex motion in a half-sector. (a) Image system. (b) Instantaneous streamlines for $\theta_v = 45^0, \phi_v = 60^0$. (c) Vortex paths on the sphere.

The vortex paths are then given by

$$\frac{[(1+r^{2m})^2 - 4r^{2m}\cos^2 m\phi](1+r^2)^2}{r^2(r^{2m}-1)^2\sin^2 m\phi} \quad = \quad const.$$

Vortex paths for m = 2 and different initial positions (θ_v, ϕ_v) are shown in figure 5.4(c). 5.5(a) shows the stereographic projection of these paths. Shown in figure 5.5(b) are paths of planar vortices in an identical domain.

Example 4 : Channel. D is the "channel" bounded by the longitudes 0 and π and the curve $\tan\frac{\theta}{2}\sin\phi = c$, a constant. D' is an infinite channel whose boundaries are $y = 0$ and $y = c$. $f(z) = e^{\pi z/c}$ maps D' to the UHP and so

$$H_p = \frac{\Gamma}{4\pi R^2}\ln\left|\frac{e^{\pi z/c} - e^{\pi z_v/c}}{e^{\pi z/c} - e^{\pi z_v^*/c}}\right|^2.$$

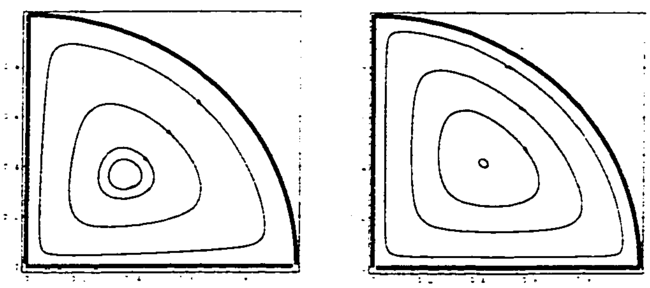

(a) (b)

Figure 5.5: Vortex motion in a half-sector. (a) Stereographic projection of vortex paths. (b) Vortex paths in an identical planar domain.

On simplification, the streamlines are given by the curves

$$\frac{\sinh^2 \frac{\pi}{2c}(x - x_v) + \sin^2 \frac{\pi}{2c}(y - y_v)}{\sinh^2 \frac{\pi}{2c}(x - x_v) + \sin^2 \frac{\pi}{2c}(y + y_v)} = const.$$

Several streamlines for the case $c = 1$, $x_v = 0, y_v = .4142\ldots$ are shown in figure 5.6(a). The number of image vortices, as is well known, is infinite.

From (5.14), we calculate

$$H_v = \frac{\Gamma^2}{4\pi R^2} \ln \frac{\pi^2}{c^2} \frac{(1 + x^2 + y^2)^2}{\sin^2 \frac{\pi}{c} y_v}$$

so that the vortex paths are

$$\frac{(1 + x^2 + y^2)^2}{\sin^2 \frac{\pi}{c} y} = const.$$

Vortex paths for different initial positions (θ_v, ϕ_v) are shown in figure 5.6(b). A stereographic projection of the paths is shown in figure 5.6(c). Figure 5.6(d) shows the paths of planar vortices in an identical domain. These are straight lines parallel to the x-axis.

Example 5 : Rectangle. D is the rectangle bounded by the longitudes 0 and ϕ_1 and latitudes θ_1 and θ_2. D' is the annular sector bounded by the circular arcs of radius $r_1 = tan\theta_1/2$ and $r_2 = tan\theta_2/2$ and by the radial lines $\phi = 0$ and $\phi = \phi_1$. D' maps to the rectangle

$D'' = \{(x, y) | \ln r_1 \leq x \leq \ln r_2, 0 \leq y \leq \phi_1\}$ under the map $u = \ln z$ where u is the plane of the rectangle D''.

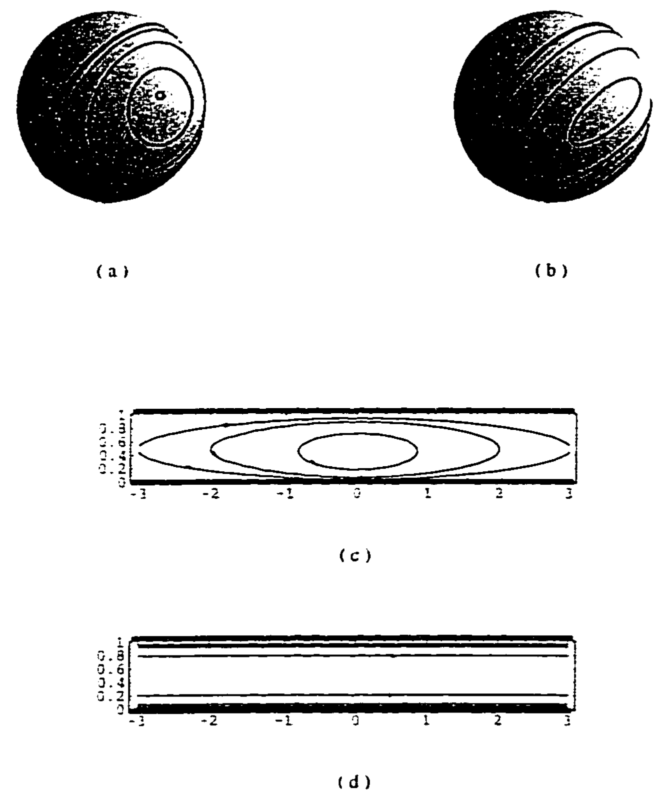

Figure 5.6: Vortex motion in a channel. (a) Instantaneous streamlines for $\theta_v = 45^0, \phi_v = 90^0$. (b) Vortex paths on the sphere. (c) Stereographic projection of vortex paths. (d) Vortex paths in an identical planar domain.

The rectangle is mapped to the lower half-plane (LHP) by the map, [1]. $w = \mathcal{P}(u - \ln r_1)$ where $\mathcal{P}(u) = \mathcal{P}(u; g2, g3)$ is the Weierstrass' $\mathcal{P}$ function and $g2, g3$ are the Weierstrass invariants, which are related to the half-periods ω and ω'. In the present case, $\omega = \ln r_2/r_1$ and $\omega' = i\phi_1$.

Thus, the annular sector D' is mapped to the LHP by $f(z) = \mathcal{P}(\ln \frac{z}{r_1})$.

The image system for a vortex in a rectangle consists of a doubly infinite lattice whose corners are occupied by image vortices [56, 107]. Thus, even for a vortex in an annular sector, we will have a doubly infinite lattice of image vortices. Using (5.13), we have the particle Hamiltonian for the annular sector as

$$H_p = \frac{\Gamma}{2\pi R^2} \ln \left| \frac{\mathcal{P}(\ln \frac{z}{r_1}) - \mathcal{P}(\ln \frac{z_v}{r_1})}{\mathcal{P}(\ln \frac{z}{r_1}) - \mathcal{P}(\ln \frac{z_v^*}{r_1})} \right|.$$

Using (5.14), the vortex Hamiltonian is obtained as

$$H_v = \frac{\Gamma^2}{2\pi R^2} \ln \left| \frac{(1 + r_v{}^2)\mathcal{P}'(\ln \frac{z_v}{r_1})}{\mathcal{P}(\ln \frac{z_v}{r_1}) - \mathcal{P}(\ln \frac{z_v^*}{r_1})} \right|.$$

(a) (b)

Figure 5.7: Vortex motion in a rectangle. (a) Instantaneous streamlines for $\theta_v = 45^0, \phi_v = 30^0$. (b) Vortex paths on the sphere.

Several streamlines for the case $\phi_1 = \pi/4, \theta_1 = \pi/6, \theta_2 = \pi/3$ and $\theta_v = \pi/4, \phi_v = \pi/6$ are shown in figure 5.7(a). Figure 5.7(b) shows the vortex paths for different initial positions (θ_v, ϕ_v).

Appendix I. Two vortex problem.

The two vortex problem can be completely solved. and certain aspects of the solution are described in [25]. We summarize the solution in a form that is consistent with our treatment of the three vortex problem. There are two invariants given by the Hamiltonian H and the center of vorticity vector $\mathbf{c}$:

$$\begin{aligned} H &= \frac{1}{4\pi R^2}\Gamma_1\Gamma_2\ln(l_{12}^2) \\ \mathbf{c} &= \frac{\Gamma_1\mathbf{x_1}+\Gamma_2\mathbf{x_2}}{\Gamma_1+\Gamma_2} \end{aligned}$$

Since the Hamiltonian is conserved. the distance between the two vortices remains fixed. There are two separate cases to consider: $\mathbf{c}=0$ and $\mathbf{c}\neq 0$.

$\mathbf{c}=0$:

In this degenerate case. the vectors $\mathbf{x_1}$ and $\mathbf{x_2}$ are linear multiples of each other. hence point in opposite directions. i.e. the vortices lie on opposite sides of the sphere. Since the length of each vector is equal to R. we must have $|\Gamma_1|=|\Gamma_2|$. It is easy to show that for any strengths. if the two vortices lie on opposite sides of the sphere. they are in fixed equilibrium. Furthermore. since each vortex lies at an elliptic fixed point of the flow. the equilibrium is nonlinearly stable. Recall that in the plane. no fixed states are possible for N=2.

$\mathbf{c}\neq 0$:

For this case, there is no loss in generality in always orienting the vortices so that the $\mathbf{c}$ vector points straight up. Our starting point is the formula:

$$\dot{\mathbf{x}}_i = \frac{\mathbf{M}}{2\pi R l_{12}^2}\times\mathbf{x_i}$$

Then the possible configurations can be listed as:

1. In general,the above formula implies that the two vortices move on cones around the center of vorticity vector $\mathbf{c}$. If $\mathbf{M}\times\mathbf{x_i}=0$, i.e. if the vortices are directly opposite each other, then as in the degenerate case $\mathbf{c}=\mathbf{0}$, the vortices are in a fixed, nonlinearly stable equilibrium. If $\mathbf{M}\times\mathbf{x_i}\neq 0$, then the frequency of rotation is given by $\omega=||\mathbf{M}||/2\pi R l_{12}^2$.
2. If $\Gamma_1=\Gamma_2$, the vortices are on the same latitude but on opposite sides of the sphere.
3. If $\Gamma_1+\Gamma_2=0$, the vortices are on the same longitude and symmetrically placed on equal latitudes on either side of the sphere.

Appendix II

Appendix II has some of the fortran and mathematica programs that were used to draw pictures in this work. *special.f* is used to plot the vortex paths in the special periodic solution (cf. §2.5). Vortex trajectories for the positive collapse time, τ_+ are caculated by *colp.f*. All contour plots on the sphere are drawn using the mathematica package, *contour.m*, written by Dr.Allan Hayes, Mathematica Consultant, UK, supplemented with a short program in Mathematica written for the specific problem. Two programs for plotting streamlines on a sphere, without and with domains, are included.

special.f

The fortran program given below calculates the vortex paths for the special periodic solution (cf. §2.5).

```
cProgram to calculate vortex paths in special periodic solution
c***********************************************************

      open(95,file='v1.out')
      open(96,file='v2.out')
      open(97,file='v3.out')

      pi=4*atan(1.)
      am1 = 1.
      am2 = 1.
      am3 = - 1.
      sigma = am1 + am2 + am3
      alpha0 = pi/18
      u = am1/2/pi/sin(2*alpha0)
      tau = 4*pi/u

       do 10 i=1,1001
             t=(i-1)*tau/1000

      el12=sqrt((cos(u*t/2))**2+(sin(2*alpha0))**2*(sin(u*t/2))**2)
      el12 = 2*el12
      v = sqrt(el12**2 - 4*(sin(2*alpha0))**2)
      if((251.lt.i).and.(i.lt.751)) go to 2
      alpha=.5*asin(2*sin(2*alpha0)/el12)
```

```
      el23 = sqrt((el12/2)*(el12+v))
      el31 = sqrt((el12/2)*(el12-v))
      w1 = sqrt(4 - el12**2)
      w2 = sin(2*alpha0)*sin(u*t/2)

      x1 = el23*w1*cos(u*t/2) - 2*el31*w2
      x1 = (el23/el12**2)*x1
      y1=el23*w1*w2 + 2*el31*cos(u*t/2)
      y1=(el23/el12**2)*y1
      z1 = .5*(2 - el23**2)

      x2 = el31*w1*cos(u*t/2) + 2*el23*w2
      x2 = (el31/el12**2)*x2
      y2=  el31*w1*w2 - 2*el23*cos(u*t/2)
      y2=(el31/el12**2)*y2
      z2 = .5*(2 - el31**2)

      x3 = w1*cos(u*t/2)
      y3 = w1*w2
      z3 = .5*(2 - el12**2)

      go to 3
2     alpha = pi/2 - .5*asin(2*sin(2*alpha0)/el12)

      el23 = sqrt((el12/2)*(el12-v))
      el31 = sqrt((el12/2)*(el12+v))
      w1 = sqrt(4 - el12**2)
      w2 = sin(2*alpha0)*sin(u*t/2)

      x1 = el23*w1*cos(u*t/2) - 2*el31*w2
      x1 = (el23/el12**2)*x1
      y1 = el23*w1*w2 + 2*el31*cos(u*t/2)
      y1= (el23/el12**2)*y1
      z1 = .5*(2 - el23**2)

      x2 = el31*w1*cos(u*t/2) + 2*el23*w2
      x2 = (el31/el12**2)*x2
```

```
      y2=  el31*w1*w2 - 2*el23*cos(u*t/2)
      y2=(el31/el12**2)*y2
      z2 = .5*(2 - el31**2)

      x3 = w1*cos(u*t/2)
      y3 = w1*w2
      z3 = .5*(2 - el12**2)

 3    write(95,*)x1,y1,z1
      write(96,*)x2,y2,z2
      write(97,*)x3,y3,z3

 10         continue
            stop
            end
```

colp.f

Given $\Gamma_1, \Gamma_2, \Gamma_3$ and initial vortex separations l_{12}, l_{23}, l_{31} such that the conditions for collapse are met (cf. §3.1), the following fortran program gives the vortex paths for the positive collapse time, τ_+. A similar program, which is not presented, gives the paths for the negative collapse time, τ_-.

```
cProgram to calculate vortex paths for collapse time tau+
c*******************************************************

c 'colxp.out' gives the xth vortex path for tau+

      open(60,file='col1+.out')
      open(61,file='col2+.out')
      open(62,file='col3+.out')

      pi=4*atan(1.)
      am1 = 1.
      am2 = 1.
      am3 = - am1*am2/(am1+am2)
      sigma = am1 + am2 + am3
      el12 = .5
      el23 = .674
```

```
el31 = .214

vdot = (el12**2 - el23**2)*(am1+am3)/el31**2
vdot = vdot + (el23**2 - el31**2)*(am2+am1)/el12**2
vdot = vdot + (el31**2 - el12**2)*(am3+am2)/el23**2
vdot = 2*vdot-el12**2*(am1-am2)-el23**2*(am2-am3)
vdot = vdot -el31**2*(am3-am1)

ambda1 = (el12/el31)**2
ambda2 = (el23/el31)**2
ambda = 1./ambda2

a = (am1+am2)**3 + am1**3*(1+1/ambda) + am2**3 * (1+ambda)
a = a/(4*pi*(am1 + am2))
a1 = a/am2/(1+ambda)
a2 = a*ambda/am1/(1+ambda)
a3 = a/(am1+am2)

alpha1 = am2*am3/(4*am1*sigma)
alpha2 = am3*am1/(4*am2*sigma)
alpha3 = am1*am2/(4*am3*sigma)

beta1 =  (am2 + am3)/8/pi
beta2 =   (am3 + am1)/8/pi
beta3 =  (am1 + am2)/8/pi

gamma = 2*(ambda1 + ambda2) - (ambda1-ambda2)**2 - 1
rho = ambda1*ambda2/gamma
alpha = sqrt(1. - rho*el31**2)

taup=4*pi*sqrt(gamma)*(1+alpha)/(abs(ambda1-ambda2))/am2
taum=4*pi*sqrt(gamma)*(1-alpha)/(abs(ambda1-ambda2))/am2

w=taup*taum/(taup+taum)

e1=a1*w/(el23**2)
e2=a2*w/(el31**2)
e3=a3*w/(el12**2)
```

```
      c1=1./(sqrt(-((taup+taum)**2+4*taup*taum/(alpha1*el23**2))))
      b1=2*(a1*alpha1+beta1)*taup*taum*c1/(alpha1*el23**2)
      gamma1 = 2*c1
      delta1 = -(taup - taum)*c1

      c2=1./(sqrt(-((taup+taum)**2+4*taup*taum/(alpha2*el31**2))))
      b2=2*(a2*alpha2+beta2)*taup*taum*c2/(alpha2*el31**2)
      gamma2 = 2*c2
      delta2 = -(taup - taum)*c2

      c3=1./(sqrt(-((taup+taum)**2+4*taup*taum/(alpha3*el12**2))))
      b3=2*(a3*alpha3+beta3)*taup*taum*c3/(alpha3*el12**2)
      gamma3 = 2*c3
      delta3 = -(taup - taum)*c3

c Calculation of th10, th20, th30, phi10,phi20, phi30

      th10 = acos(1 + am2*am3*el23**2/(2*am1*sigma))
      th20 = acos(1 + am3*am1*el31**2/(2*am2*sigma))
      th30 = acos(1 + am1*am2*el12**2/(2*am3*sigma))

      phi10 = 0
      phi20 = (1-cos(th10)*cos(th20)-.5*el12**2)/sin(th10)/sin(th20)
      phi20 = acos(phi20)

      phi30 = (1-cos(th10)*cos(th30)-.5*el31**2)/sin(th10)/sin(th30)
      phi30 = acos(phi30)

      tl23 = 1-cos(th20)*cos(th30)-sin(th20)*sin(th30)*cos(phi20-phi30)
      tl23 = sqrt(2*tl23)
      if (abs(tl23 - el23).gt.1e-3) go to 102

      go to 103

 102  phi20 = 2*pi - phi20
      tl23 = 1-cos(th20)*cos(th30)-sin(th20)*sin(th30)*cos(phi20-phi30)
      tl23 = sqrt(2*tl23)
```

```
103  x10 = sin(th10)*cos(ph10)
     y10 = sin(th10)*sin(ph10)
     z10 = cos(th10)
     x20 = sin(th20)*cos(ph20)
     y20 = sin(th20)*sin(ph20)
     z20 = cos(th20)
     x30 = sin(th30)*cos(ph30)
     y30 = sin(th30)*sin(ph30)
     z30 = cos(th30)

     v0 = x10*(y20*z30 - y30*z20) - y10*(x20*z30 - x30*z20)
     v0 = v0 + z10*(x20*y30 - x30*y20)

     if((v0.gt.0).and.(vdot.gt.0)) go to 100
     if((v0.lt.0).and.(vdot.lt.0)) go to 100
     if((v0.gt.0).and.(vdot.lt.0)) go to 101
     if((v0.lt.0).and.(vdot.gt.0)) go to 101

101   phi20 = 2*pi - phi20
      phi30 = 2*pi - phi30

100   do 10 i=1,10001

         t=(i-1)*taup/10000

         phi1=e1*alog((taum+t)*(taup/taum)/(taup-t))
         phi1=phi1+b1*(atan(gamma1*t+delta1)-atan(delta1))+phi10
         tel23=el23*sqrt(1+t/taum)*sqrt(1-t/taup)
         th1=acos(1+ am2*am3*tel23**2/(2*am1*sigma))

         phi2=e2*alog((taum+t)*(taup/taum)/(taup-t))
         phi2=phi2+b2*(atan(gamma2*t+delta2)-atan(delta2))+phi20
         tel31=el31*sqrt(1+t/taum)*sqrt(1-t/taup)
         th2=acos(1+ am3*am1*tel31**2/(2*am2*sigma))

         phi3=e3*alog((taum+t)*(taup/taum) /(taup-t))
         phi3=phi3+b3*(atan(gamma3*t+delta3)-atan(delta3))+phi30
```

```
        tel12=el12*sqrt(1+t/taum)*sqrt(1-t/taup)
        th3=acos(1+ am1*am2*tel12**2/(2*am3*sigma))

        x1 = sin(th1)*cos(phi1)
        y1 = sin(th1)*sin(phi1)
        z1 = cos(th1)
        x2 = sin(th2)*cos(phi2)
        y2 = sin(th2)*sin(phi2)
        z2 = cos(th2)
        x3 = sin(th3)*cos(phi3)
        y3 = sin(th3)*sin(phi3)
        z3 = cos(th3)

        write(60,*)x1,y1,z1
        write(61,*)x2,y2,z2
        write(62,*)x3,y3,z3

 10       continue
          stop
          end
```

contour.m

This package plots contours of a function on any two-dimensional surface. It is usually convenient to write a short Mathematica program to define the function. Two such programs, used to draw figures 4.8(a) and 5.3(a), are presented later.

```
(* : Title : ContourPlotOnSurface*)(* : LAST CHANGE : 30 Dec 1998*)(*
  : Author : Allan Hayes, hay@haystack.demon.co.uk*)(*
  : Summary :
      ContourLines3D has two functions :
          \n ParametricPlot3DContoured and Plot3DContoured,
  that allow contour lines to be drawn on 3D plots.
      \n There are three special options : ContourLift,
  ContourColorFunction and Surface.Graphics3D[
        Graphics3DContoured[ ...]] gives a Graphics3D object.*)(*
  : Context : haypacks`Graphics`ContourPlotOnSurface `*)(*
  : Package Version : 1.2*)(* : Copyright : Copyright 1994, 1996, 1997,
  1998 Allan Hayes.*)(* : History : Version 1.4 by Allan Hayes,
```

```
  Nov 1998 Defined Plot3DContoured in terms of ParametricPlot3DContoured \
instead of coding separately (may slow computation a bit but simplifies \
code).Allowed for empty list of contour lines (caused by the contour values
\
being outside the height range).Version 1.3 by Allan Hayes,
  March 1997 Contour lines of function f[s, t] on surface {x[s, t], y[s, t],
      z[s, t]} added.Version 1.2 by Allan Hayes,
  Nov 1994 ContourLines3DInfo added Version 1.2 by Allan Hayes,
  May 1994. Version 1.1 by Allan Hayes, March 1994.*)(*
  : Warning :
      Show is extended to deal with the object that is returned by the \
function PlotContoured.Color directives given in ContourStyles are usually \
not operative;
  they must usually be given separately by the option ContourColorFunction \
(but see the entry for ContourColorFunction).*)(* : Keywords : Contour*)(*
  : Mathematica Version : 2.2*)(*
  : Limitation :
      The Graphics3DContoured object that is output is not yet combining
with \
other graphics and does not respond to FullOptions and FullGraphics*)
  BeginPackage["haypacks`Graphics`ContourLines3D`",
    "Utilities`FilterOptions`"];
Unprotect["`*"]; ClearAll["`*"];
(**Usage messages**)
ContourLines3DInfo::usage =
    "ContourLines3D is a package with two functions,\n
Plot3DContoured,gives a Plot3D surface with contour lines added,\n
ParametricPlot3DContoured, gives a ParametricPlot3D surface with contour\n
lines of a function of the parameters added;\n
extensive options allow variations to be made.\n
\nPlease see the separate entries for more information and examples.
";
ParametricPlot3DContoured::usage =
    "ParametricPlot3DContoured[{x,y,z,w},{u,umin,umax},{v,vmin,vmax}, opts],
for expressions x,y,z,w in u,v, gives the contour lines of w on the surface
\
given by ParametricPlot3D[{x,y,z},{u,umin,umax},{v,vmin,vmax}, opts].\n
ParametricPlot3DContoured[{x,y,z},{u,umin,umax},{v,vmin,vmax}, opts] gives \
```

```
the same as
ParametricPlot3D[{x,y,z,z},{u,umin,umax},{v,vmin,vmax}, opts].\n
The contour styles are controlled by the options ContourStyles (as for \
ContourPlot) and a new option, ContourColorFunction except that color \
directives must usually be given separately by the option \
ContourColorFunction (but see the entry for ContourColorFunction). The
amount \
by which contours are moved towards the viewpoint to avoid parts of them \
being hidden by the surface is controlled by the option ContourLift.
.\n\n

Options:\n
ParametricPlot3DContoured has the union of the options of ParametricPlot3D,
\
and ContourPlot as options, together with three new options  ContourLift, \
ContourColorFunction and Surface.\n\n

Examples:\n
ParametricPlot3DContoured[{t Sin[s] Cos[t], t Cos[s] Cos[t], Sin[t]},
{s,0,2Pi},{t,-Pi/2, Pi/2}
]\n\n

ParametricPlot3DContoured[{t Sin[s] Cos[t], t Cos[s] Cos[t], Sin[t],s+t},
{s,0,2Pi},{t,-Pi/2, Pi/2}
]\n\n
For more examples please enter ?ParametricPlot3DContouredExamples.
";
Plot3DContoured::usage =
    "Plot3DContoured[{z,w},{u,umin,umax},{v,vmin,vmax}, opts], for \
expressions z, w in u,v, gives the contour lines of w on the surface given
by \
Plot3D[z,{u,umin,umax},{v,vmin,vmax}, opts].\n
Plot3DContoured[z,{u,umin,umax},{v,vmin,vmax}, opts] gives the same as \
Plot3DContoured[{z,z},{u,umin,umax},{v,vmin,vmax}, opts].\n

Options:\n
Plot3DContoured has the union of the options of Plot3D and ContourPlot as \
options, together with three new options  ContourLift, ContourColorFunction
```

```
\
and Surface.\n
The contour styles are controlled by the options ContourStyles (as for \
ContourPlot) except that color directives must usually be given separately
by \
the new option ContourColorFunction (but see the entry for \
ContourColorFunction). The amount by which contours are moved towards the \
viewpoint to avoid parts of them being hidden by the surface is controlled
by \
the option ContourLift.\n\n

Examples:\n
Plot3DContoured[2x^4 - y^4, {x,-1,1},{y,-1,1},Axes -> True]\n\n
Plot3DContoured[{2x^4 - y^4, x y}, {x,-1,1},{y,-1,1},Axes -> True]\n\n
For more examples please enter ?Plot3DContouredExamples.
";
ContourLift::usage =
    "ContourLift is an option for Plot3DContoured, ParametricPlot3DContoured
\
and Graphics3DContoured.\n
For a number r, ContourLift ->r, causes each contour to be moved towards the
\
viewpoint by r times the length of the bounding box in the direction of the
\
view point. This is used to avoid some parts being covered by the surface.\n
The default is ContourLift ->Automatic.
";
ContourColorFunction::usage =
    "ContourColorFunction is an option for Plot3DContoured, \
ParametricPlot3DContoured and Graphics3DContoured. \n
ContourColorFunction ->cf, causes each contour to assigned the color \
cf[scaledz] where scaledz runs from 0 at the lower end of the range of \
plotted values of z up to 1 at the top of the range.\n
The default is ContourColorFunction ->Hue.\n\n
NOTE:\n
Directives set by ContourColorFunction will shadow any coresponding ones set
\
by ContourStyles, but ContourColorFunction -> ({}&) will allow all \
```

```
ContourStyles set directives to function.
ContourColorFunction can be used to modify more than the color of the
contour \
lines. ContourColorFunction -> (Thickness[#/100]&) will set the thickness;
ContourColorFunction -> ((Sequence@@{Hue[#], Thickness[#/100]})&) will set \
both color and thickness in.\n
ColorFunction -> Transparent gives a wire frame picture.
";
Surface::usage =
    "Surface is an option for Plot3DContoured, ParametricPlot3DContoured and
\
Graphics3DContoured.\n
With Surface -> True, the surface on which the contours are to be
drawn is displayed; with Surface -> False the surface is not displayed (the
\
edges of the surface patches are not shown) ;
with Surface -> Transparent a wire frame version is displayed (the style of
\
the mesh is then controlled by the option ColorFunction).\n
The default is Surface -> True.
";
Graphics3DContoured::usage =
    "Graphics3DContoured[primitives list, options] is the kind of graphic \
object returned by ParametricPlot3DContoured and Plot3DContoured\n\n
Options:\n
Graphics3DContoured has the union of the options of ContourGraphics, \
SurfaceGraphics and Graphics3D as options, together with three new options
\
ContourLift, ContourColorFunction and Surface.
";
Transparent::usage = "Transparent is a setting for the option Surface in
ContourLines3D which specifies that a wire frame version be displayed.";
ParametricPlot3DContouredExamples::usage = "

ParametricPlot3DContoured[{t Sin[s] Cos[t], t Cos[s] Cos[t], Sin[t]},
{s,0,2Pi},{t,-Pi/2, Pi/2}];\n\n

ppc =
```

```
ParametricPlot3DContoured[{t Sin[s] Cos[t], t Cos[s] Cos[t], Sin[t], s+t},
{s,0,2Pi},{t,-Pi/2, Pi/2}];\n\n
Show[ppc,
PlotRange -> {All, {-.2,1.1},All},
ViewPoint->{1.393, -2.988, -0.764}
];\n\n
Show[ppc, Lighting -> False, ColorFunction -> GrayLevel];\n\n
Show[ppc,
Surface -> False,
Contours -> 36,
ContourColorFunction -> (Hue[1-#]&)
];\n\n

Show[ppc,
Surface->Transparent,
ColorFunction -> Hue,
(*controls mesh color when Surface->Transparent is set*)
Boxed -> False,
Axes -> False
];\n\n
Show[ppc,
ContourStyle -> Thickness[.007],
ContourColorFunction->(GrayLevel[0]&),
Mesh -> True,
MeshStyle -> GrayLevel[.5],
Shading -> False
];\n\n
transparentball =
ParametricPlot3DContoured[
{Sin[s] Cos[t], Cos[s] Cos[t], Sin[t]},
{s,0,2Pi},{t,-Pi/2, Pi/2},
ContourLift -> .7,
AmbientLight -> GrayLevel[.2],
Boxed -> False,
Axes -> False
];\n\n
(*this shows how the illusion is created*)\n
Show[Graphics3D[transparentball], ViewPoint->{3.265, 0.888, 0.042}];
```

```
";
Plot3DContouredExamples::usage = "
(***\n
You can evaluate these examples by converting the cell in which they are
generated to an input cell and then evaluatiing the cell.\n
***)\n
Plot3DContoured[2x^4 - y^4, {x,-1,1},{y,-1,1},Axes -> True];\n\n
Show[pc,
PlotRange -> {All, {-.2,1.1},All},
ViewPoint->{1.393, -2.988, -0.764}
];\n\n
pc =
Plot3DContoured[{2x^4 - y^4, x y}, {x,-1,1},{y,-1,1},Axes -> True];\n\n
Show[pc,
PlotRange -> {All, {-.2,1.1},All},
ViewPoint->{1.393, -2.988, -0.764}
];\n\n
Show[pc, Lighting -> False, ColorFunction -> GrayLevel];\n\n
Show[pc,
Surface -> False,
ContourColorFunction -> (Hue[1-#]&)
];\n\n
Show[pc,
Surface->Transparent,
ColorFunction -> (GrayLevel[.8] &),\n
(*controls mesh color when Surface->Transparent is set*)
ContourStyle -> Thickness[.015],
Boxed -> False,
Axes -> False,
PlotRange -> All\n
(*stops clipping of polygons -- compare earlier pictures*)
];\n\n
Show[pc,
ContourStyle -> Thickness[.007],
ContourColorFunction->(GrayLevel[0]&),
Mesh -> True,
MeshStyle -> GrayLevel[.5],
Shading -> False
```

```
];
";
(**Private Code**)
Begin["`Private`"];
Clear["`*"];
Format[Graphics3DContoured[x___]] := "-Graphics3DContoured-";
(*In defining the options I have used Union to avoid the duplication that \
would result if I used Join.*)
Options[Graphics3DContoured] =
    Union @@ ({Options[ContourGraphics], Options[SurfaceGraphics],
            Options[Graphics3D],
            {ContourLift -> Automatic, ContourColorFunction -> Hue,
              Surface -> True}} /.
          {(AspectRatio -> _) -> (AspectRatio -> Automatic),
            (AmbientLight -> _) -> (AmbientLight -> GrayLevel[0.]),
            (Axes -> _) -> (Axes -> True),
            (BoxRatios -> _) -> (BoxRatios -> Automatic),
            (ColorFunction -> _) -> (ColorFunction -> Automatic),
            (ContourShading -> _) -> (ContourShading -> False),
            (ContourSmoothing -> _) -> (ContourSmoothing -> None),
            (ContourStyle -> _) -> (ContourStyle -> {}),
            (Mesh -> _) -> (Mesh -> False),
            (MeshStyle -> _) -> (MeshStyle -> GrayLevel[0])});
Options[ParametricPlot3DContoured] =
    Union[{Compiled -> True, PlotPoints -> 25},
      Options[Graphics3DContoured]];
Options[Plot3DContoured] =
    Options[ParametricPlot3DContoured] /.
      (BoxRatios -> _) -> (BoxRatios -> {1, 1, 0.4});
(*UVP, below, converts the viewpoint, vp,
  from viewpoint coordinates to user coordinates.VP converts from user \
coordinates to viewpoint coordinates*)
UVP[vp_, br_, pr_] := pr.{1, 1}/2 + pr.{-1, 1} Max[br]/br vp;
VP[uvp_, br_, pr_] := (uvp - pr.{1, 1}/2)br/Max[br]/pr.{-1, 1};
zscaler = Compile[{n1, n2, n3, n4, m, h}, ((n1 + n2 + n3 + n4)/4 - m)/h];
ParametricPlot3DContoured[{x_, y_, z_}, {u_, umin_, umax_},
      {v_, vmin_, vmax_}, opts___?OptionQ] :=
    ParametricPlot3DContoured[{x, y, z, z}, {u, umin, umax}, {v, vmin,
```

```
vmax},
      opts];
(*define Plot3DContoured in terms of ParametricPlot3DContoured*)
Plot3DContoured[{z_, w_}, {u_, umin_, umax_}, {v_, vmin_, vmax_},
    opts___?OptionQ] :=
  ParametricPlot3DContoured[{u, v, z, w}, {u, umin, umax}, {v, vmin, vmax},
    opts]

ParametricPlot3DContoured[{x_, y_, z_, w_}, {u_, umin_, umax_},
      {v_, vmin_, vmax_}, opts___?OptionQ] :=
    Module[{px, py, pz, pw, defopts, ppts, polydat, zdat, mr,
        graphicsobject},(**
          STEP1 : construct the basic data that depends only on the the \
parametric formulas x, y, z,
        the u and v ranges and the "plot" option PlotPoints.This will be \
passed on unchanged through any uses of Show.**)(*Find the current default \
options-- to allow control by the SetOptions function.*)defopts =
        Sequence @@ Options[ParametricPlot3DContoured];
      ppts = PlotPoints /. {opts} /. {defopts};
      (*Make compiled or pure functions {px, py, pz, pw} out of {x, y, z, w}
          : these are convenient for passing.*){px, py, pz, pw} =
        If[Compiled /. {opts, defopts},
          Thread[comp[{u, v}, {x, y, z, w}], List, -1] /. comp -> Compile,
          Function /@
            ({x, y, z, w} /. {u :> #1, v :> #2})];  (*Find the polygons,
        polydat,
        for surface on which the contours will be drawn.The extra brackets \
are to conform to the pattern when directives are added.*)polydat =
        {List /@
            (ParametricPlot3D[{x, y, z}, {u, umin, umax}, {v, vmin, vmax},
                  DisplayFunction -> Identity, PlotPoints -> ppts][[1]])};
      (*Find matrix of heights, wdat, as a function of u, v-- the x,
        y coordinates will be adjusted later.We also need the meshrange mr
so \
that the original values of u and v can be reconstructed.*)wdat =
        Plot3D[w, {u, umin, umax}, {v, vmin, vmax},
            DisplayFunction -> Identity, PlotPoints -> ppts][[1]];
      zdat =
```

```
          Plot3D[z, {u, umin, umax}, {v, vmin, vmax},
              DisplayFunction -> Identity, PlotPoints -> ppts][[1]];
        mr = {{umin, umax}, {vmin, vmax}};
        (*Pass data on to makegraphics to make a Graphics3DContoured object
The \
{}'s holds places data that depends on Graphics3DContoured options to be \
added metdat will be the value of {Boxratios,
            PlotRange} that have actually been used in a plot.These will be
\
obtained using the function FullOptions and need not be the values assigned
\
by the options (because, for example,
              PlotRange ->
                Automatic is a default setting).cdat will be the data from \
which the contour lines will be constructed once their number and other \
properties have been specified.*)(**STEP2 : Use the function makegraphics,
        defined separately,
        to construct a graphics object with new head
Graphics3DContoured.This \
contains all the data, including all the options given,
        from which to display the result by means of a suitably extended \
version of the function Show.**)graphicsobject =
        makegraphics[
          {{px, py, pz, pw}, zdat, wdat, polydat, {}(*for metdat*),
            {}(*for cdat*)},
          FilterOptions[Graphics3DContoured, MeshRange -> mr, opts,
            defopts]];
        (*Show the graphics just constructed.*)(**
          STEP3 : display the result by means of a suitably extended version
\
of the function Show, defined separately.**)Show[graphicsobject]];
(*The function makegraphics, defined below,
  gives a ContouredSurfaceGraphics object.A principle aim in designing the \
code has been to keep recomputation as close as sensible to the minimum \
required by new option settings introduced by when using Show.*)
makegraphics[
      {{px_, py_, pz_, pw_}, zdat_, wdat_, oldpolydat_, oldmetdat_,
oldcdat_,
```

```
        oldopts___}, newopts___] :=
    Module[{optsset, opts, vp, br, cl, ccf, pcf, clnsQ, edgfm, msh, mshs,
cs,
        sur, ppts, lftrat, pr, cln, cplot, cplot2D, uvp, center, ucp, maxs,
        tmin, thbx, zpr, zmin, hbx, newcdat, clines, us, vs, zav, xyz, vecs,
        unitvecs, cyclestyles, csc, clip, nearpt, lift, lftpt, dpr, dvp,
        gr1},(*Find the list of options that are set in newopts*)optsset =
        First /@ {newopts}; (*Join newopts and oldopts for
convenience.*)opts
        = Sequence[newopts,
          oldopts];  (*Find the settings of some of the options.*)
        {br, ccf, cl, clnsQ, cs, mshQ, mshs, pcf, vp} =
        {BoxRatios, ContourColorFunction, ContourLift, ContourLines,
            ContourStyle, Mesh, MeshStyle, ColorFunction, ViewPoint} /.
          {opts};   edgfm = If[! mshQ, EdgeForm[], EdgeForm[mshs]];
      newpolydat =
        {edgfm, Last[
            oldpolydat]}; (*If newopts change plotrange or box ratios find \
their new values.*)If[MemberQ[optsset, BoxRatios | PlotRange],
        {newfbr, newfpr} =
          FullOptions[
            Graphics3D[newpolydat, FilterOptions[Graphics3D, opts]],
            {BoxRatios, PlotRange}],
        {newfbr, newfpr} = oldmetdat];   (*Find the thickness of the box,
        thbx, (in user coordinates) along the line through the center and
the \
viewpoint.*)uvp = UVP[vp, newfbr, newfpr]; (*Viewpoint in user
coordinates.*)
        center = newfpr.{1, 1}/2;
      ucp = uvp - center;
      maxs = Max /@ newfpr;
      Off[Power::infy];  tmin = Min[Abs[(maxs - center)/ucp]];
      On[Power::infy];
      thbx = 2 tmin Sqrt[ucp.ucp] //
          N; (*Find the ratio lftrat of the thickness of the box in the \
direction of the view point by which the contours will be lifted*)ppts =
        Dimensions[wdat];
      lftrat := If[cl === Automatic, 0.5/(Plus @@ ppts), cl];
```

```
      (*Find a display plotrange, dpr,
        which will include the lifted contours.Calculate the corresponding \
display box ratio dbr and display ViewPoint, dvp,
        the position of the latter in user coordinates relative to br and
dpr \
is still uvp (this will keep the lifted contours in line with the unlifted \
ones as seen from the view point used in the display).*)clip[x_, {a_, b_}]
:=
        Which[x < a, a, x > b, b, True, x];
      nearpt[uvp_, newfpr_] := Thread[clip[uvp, newfpr]];
      lift[uvp_, pr_, d_] := Module[{np}, np = nearpt[uvp, pr];
          (np + d #/Sqrt[#.#]) &[uvp - np]];
      lftpt = lift[uvp, newfpr, lftrat thbx];
      dpr = {Min[#], Max[#]} & /@ MapThread[List, {lftpt, newfpr}];
      dbr = If[br === Automatic, dpr.{-1, 1}, br];   dvp = VP[uvp, dbr,
dpr];
      (*Find the height, hbx, of the box in user coordinates,
        needed to find the scaled height used for
ContourColorFunction.*)wmin
        = Min[wdat];
      wmax = Max[wdat];
      wrange = wmax - wmin;  znewfpr = newfpr[[-1]]; zmin = Min[znewfpr];
      zmax = Max[znewfpr];
      hbx = zmax - zmin;
      (*Find the 2D contour lines from wdat by using ContourGraphics and \
converting to a Graphics object.The heights will be added later and the u,
        v coordinates will be mapped to the corresponding x,
        y values.The split into styles and lines is for efficiency in making
\
changes by options.*){styles, lines} =
        If[(gr1 =
                Graphics[
                      ContourGraphics[wdat, ContourShading -> False,
                        FilterOptions[ContourGraphics,
                          PlotRange ->
                            {wmin, wmax} (*newfpr[[-1]]*),(*Not newfpr,
                            which is in terms of x, y and z*)opts]]][[1]] /.
                  {dirs__, ln_Line} -> {{dirs}, ln}) === {}, {{}, {}},
```

```
            Transpose[gr1]];
        (*Do those calculations for lifting the contours that depend on the \
"metric" options BoxRatios, Contours, PlotRange, ViewPoint,
          ContourSmoothing.Store the data as newcdat.The full code for the \
contour lines is constructed later from newcdat and styles.*)If[
          clnsQ &&
            MemberQ[optsset,
              BoxRatios | ViewPoint | PlotRange | Contours |
ContourSmoothing],
          newcdat =
            If[lines === {}, {},
              lines /. Line[ps_] :> ({us, vs} = Transpose[ps];

                      wav = Inner[pw, us, vs]/Length[ps];(*av of w on
contour*)ws
                        = Table[wav, {Length[ps]}];
                      xyz = {MapThread[px, {us, vs}], MapThread[py, {us, vs}],
                          MapThread[pz, {us, vs}]};
                      vecs = Transpose[uvp - xyz];
                      unitvecs =
                        Block[{Dot},
                          vecs/Sqrt[
                              Thread[
                                Dot[vecs,
                                  vecs]]]]; (*unit vecs in direction of
viewpoint*)
                        {(*(zav - zmin)/hbx,*)(wav - wmin)/wrange,
                        Transpose[xyz], thbx unitvecs})],(*else -
              if no changes are needed to cdat.*)newcdat = oldcdat];
        (*Insert the directives for the polygons*)If[
          pcf =!= Automatic && MemberQ[optsset, ColorFunction],
          newpolydat =
            newpolydat /.
              {___, poly : Polygon[pts_]} :>
                {pcf[zscaler[Sequence @@ (Last /@ pts), zmin, hbx]],
                  poly}]; (*Complete the code for the contour lines using \
lftrat (derived from the option ContourLift) and ccf (from \
ContourColourFunction).*)clines =
```

```
        If[clnsQ,
          Apply[{Sequence @@ Flatten[{##4}], ccf[#1], Line[#2 + lftrat #3]}
              &, MapThread[Join, {newcdat, styles}], {1}], {}];
      (*Return the data and options as a Graphics3DContoured object.*)
        Graphics3DContoured[
        {{px, py, pz, pw}, zdat, wdat, newpolydat, {newfbr, newfpr},
newcdat,
          clines, {dpr, dvp}}, opts]];
(*Extend Show to deal with Graphics3DContoured objects.*)
Graphics3DContoured /:
    Show[Graphics3DContoured[
        {fn_, zdat_, wdat_, polydat_, {fbr_, fpr_}, cdat_, clines_,
          {dpr_, dvp_}}, oldopts___?OptionQ], newopts___?OptionQ] :=
    If[MemberQ[First /@ {newopts},
        BoxRatios | ColorFunction | ContourColorFunction | ContourLift |
          Contours | ContourLines | ContourSmoothing | ContourStyle | Mesh |
          MeshStyle | PlotRange | Surface | ViewPoint],
      Show[makegraphics[{fn, zdat, wdat, polydat, {fbr, fpr}, cdat,
oldopts},
          newopts]],
      Show[Graphics3D[
          {Switch[Surface /. {newopts, oldopts}, True, polydat, Transparent,
              polydat /. Polygon[z_] :> Line[Append[z, First[z]]], _, {}],
            If[ContourLines /. {newopts, oldopts}, clines, {}]}],
        PlotRange -> dpr, ViewPoint -> dvp,
        FilterOptions[Graphics3D, newopts, oldopts]];
      Graphics3DContoured[
        {fn, zdat, wdat, polydat, {fbr, fpr}, cdat, clines, {dpr, dvp}},
        newopts, oldopts]];
(*Provide for conversion of Graphics3DContoured objects to Graphics3D
objects*)


Graphics3DContoured /:
    Graphics3D[
      Graphics3DContoured[
        {fn_, zdat_, wdat_,(*wdat_ added Nov12 98*)polydat_, {fbr_, fpr_},
          cdat_, clines_, {dpr_, dvp_}}, oldopts___?OptionQ],
```

```
    newopts___?OptionQ] :=
   Graphics3D[
    {Switch[Surface /. {newopts, oldopts}, True, polydat, Transparent,
        polydat /. Polygon[z_] :> Line[Append[z, First[z]]], _, {}],
      If[ContourLines /. {newopts, oldopts}, clines, {}]},
    PlotRange -> dpr, ViewPoint -> dvp,
    FilterOptions[Graphics3D, newopts, oldopts]];
End[];
Protect["`*"];
EndPackage[]
```

plot1.m

This Mathematica program was used to plot figure 4.8(a). For this. first *contour.m* is input into Mathematica followed by this program. A Mathematica session showing the sequence of instructions is included at the end.

```
g1 = .2; g2 = .02; g3 = -1

th1 = 70 Pi/180; phi1 = 0 Pi/180
th2 = 30 Pi/180; phi2 = 180 Pi/180
th3 = 90 Pi/180; phi3 = 0 Pi/180

x1 = Sin[th1] Cos[phi1]
y1 = Sin[th1] Sin[phi1]
z1 = Cos[th1]
x2 = Sin[th2] Cos[phi2]
y2 = Sin[th2] Sin[phi2]
z2 = Cos[th2]
x3 = Sin[th3] Cos[phi3]
y3 = Sin[th3] Sin[phi3]
z3 = Cos[th3]
x = Sin[th] Cos[phi]
y = Sin[th] Sin[phi]
z = Cos[th]


mu = 0
```

```
thet1 = 78.4814 Pi/180;ph1 = 180 Pi/180; thet2 =36.4466  Pi/180 ;
ph2 = 180 Pi/180; thet3 = 64.9281  Pi/180; ph3 = 0 Pi/180

w=(((x-x1)^2 + (y-y1)^2 + (z-z1)^2)^ g1) *  (((x-x2)^2 + (y-y2)^2 + (z-z2)^2)^
 g2) * (((x-x3)^2 + (y-y3)^2 + (z-z3)^2)^ g3) * Exp[mu (1+z)/2]

c1 = ((Sin[thet1] Cos[ph1] -x1)^2 + (Sin[thet1] Sin[ph1] -y1)^2 + (Cos[thet1]
-z1)^2)^ g1 *  ((Sin[thet1] Cos[ph1]-x2)^2 + (Sin[thet1] Sin[ph1]-y2)^2 +
(Cos[thet1]-z2)^2)^ g2 * ((Sin[thet1] Cos[ph1]-x3)^2 + (Sin[thet1] Sin[ph1]-
y3)^2 + (Cos[thet1]-z3)^2)^ g3 * Exp[mu (1+Cos[thet1])/2]

c2 = ((Sin[thet2] Cos[ph2] -x1)^2 + (Sin[thet2] Sin[ph2] -y1)^2 + (Cos[thet2]
-z1)^2)^ g1 *  ((Sin[thet2] Cos[ph2]-x2)^2 + (Sin[thet2] Sin[ph2]-y2)^2 +
(Cos[thet2]-z2)^2)^ g2 * ((Sin[thet2] Cos[ph2]-x3)^2 + (Sin[thet2] Sin[ph2]
-y3)^2 + (Cos[thet2]-z3)^2)^ g3 * Exp[mu (1+Cos[thet2])/2]

c3 = ((Sin[thet3] Cos[ph3] -x1)^2 + (Sin[thet3] Sin[ph3] -y1)^2 + (Cos[thet3]
-z1)^2)^ g1 *  ((Sin[thet3] Cos[ph3]-x2)^2 + (Sin[thet3] Sin[ph3]-y2)^2 + (Cos
[thet3]-z2)^2)^ g2 * ((Sin[thet3] Cos[ph3]-x3)^2 + (Sin[thet3] Sin[ph3]-y3)^2
+ (Cos[thet3]-z3)^2)^ g3 * Exp[mu (1+ Cos[thet3])/2]


ppc=ParametricPlot3DContoured[{x,y,z,w},{th,0, Pi},{phi,0, 2 Pi},Contours->{
c1,c2,c3},PlotPoints->100,ContourSmoothing->True,ContourShading->False,
ContourStyle -> Thickness[0.005],ContourColorFunction->(GrayLevel[0]&),
Boxed->False,Axes->False]
```

sector.m

This program, along with *contour.m*, was used to draw figure 5.3(a).

```
x = Sin[th] Cos[phi]
y = Sin[th] Sin[phi]
z = Cos[th]

m = 2

th0 = Pi/2
phi0 = Pi/2
```

```
thv = Pi/4
phiv =  Pi/3

rv = Tan[thv/2]
r = Tan[th/2]

psip = (r^(2 m) + rv^(2 m) - 2 r^m rv^m Cos[m(phi-phiv)]) (r^(2 m) rv^(2 m) +
1 - 2 r^m rv^m Cos[m(phi+phiv)]) /( (r^(2 m) + rv^(2 m) - 2 r^m rv^m Cos[m(phi
+phiv)])  (r^(2 m) rv^(2 m) + 1 - 2 r^m rv^m Cos[m(phi-phiv)]) )

f =
If[(0<=th<=th0)&&(0<=phi<=phi0),psip,1]

th1 = Pi/4; phi1 = 0; th2 = Pi/4; phi2 = Pi/6; th3 = Pi/3; phi3 = 80 Pi/180
th4 = 80 Pi/180; phi4 = Pi/18; th5 = Pi/2; phi5 = Pi/2

r1 = Tan[th1/2]; r2 =Tan[th2/2]; r3 = Tan[th3/2]; r4 = Tan[th4/2]; r5 = Tan[
th5/2]

c1 =  (r1^(2 m) + rv^(2 m) - 2 r1^m rv^m Cos[m(phi1-phiv)]) /  (r1^(2 m) +
rv^(2 m) - 2 r1^m rv^m Cos[m(phi1+phiv)])

c2 =  (r2^(2 m) + rv^(2 m) - 2 r2^m rv^m Cos[m(phi2-phiv)]) /  (r2^(2 m) +
rv^(2 m) - 2 r2^m rv^m Cos[m(phi2+phiv)])

c3 = (r3^(2 m) + rv^(2 m) - 2 r3^m rv^m Cos[m(phi3-phiv)]) /  (r3^(2 m) +
rv^(2 m) - 2 r3^m rv^m Cos[m(phi3+phiv)])

c4 =  (r4^(2 m) + rv^(2 m) - 2 r4^m rv^m Cos[m(phi4-phiv)]) /  (r4^(2 m) +
rv^(2 m) - 2 r4^m rv^m Cos[m(phi4+phiv)])

c5 =  (r5^(2 m) + rv^(2 m) - 2 r5^m rv^m Cos[m(phi5-phiv)]) /  (r5^(2 m) +
rv^(2 m) - 2 r5^m rv^m Cos[m(phi5+phiv)])


ppc = ParametricPlot3DContoured[{x,y,z,f},{th,Pi/720, Pi},{phi,0, 2 Pi},
Contours->{c2,c3,c4},PlotPoints->100,ContourSmoothing->True,ContourShading->
```

```
False,ContourStyle -> Thickness[0.005],ContourColorFunction->(GrayLevel[0]&),
Boxed->False,Axes->False,ViewPoint->{3.5,2.5,.7}]
```

A typical Mathematica session, used in constructing the contours on a sphere, is presented below.

```
In[1]:= <<contour.m

In[2]:= <<plot1.m

Out[2]= -Graphics3DContoured-

In[3]:= Graphics3D[%]

Out[3]= -Graphics3D-

In[4]:= Display["file1.eps",%,"EPS"]

Out[4]= -Graphics3D-

In[5]:= <<sector.m

Out[5]= -Graphics3DContoured-

In[6]:= Graphics3D[%]

Out[6]= -Graphics3D-

In[7]:= Display["file2.eps",%,"EPS"]

Out[7]= -Graphics3D-
```

Reference List

[1] M. Abramowitz, I.A. Stegun, **Handbook of Mathematical Functions**, Dover, New York, 1965.

[2] J.Adem, 'A series solution for the barotropic vorticity equation and its application in the study of atmospheric vortices' . Tellus 8, 364 - 372.

[3] A.A. Andronov, E.A. Leontovich, I.I. Gordon, A.G. Maier, **Qualitative Theory of Second Order Dynamical Systems**, J. Wiley, New York, 1973.

[4] R.A. Anthes, **Tropical Cyclones : Their Evolution, Structure and Effects.** American Meteorological Society, Boston , 1982.

[5] H. Aref, 'Motion of three vortices', Phys. of Fluids 22(3), 393-400, 1979.

[6] H. Aref, 'Integrable, chaotic and turbulent vortex motion in two-dimensional flows', Ann. Rev. Fluid Mech. 15, 345-389, 1983.

[7] H. Aref, M. Bröns, ' On stagnation points and streamline topology in vortex flows', J. Fluid Mech. 370, 1-27, 1998.

[8] H. Aref, N. Pomphrey, 'Integrable and chaotic motion of four vortices,I. The case of identical vortices', Proc. Roy. Soc. Lond. A380, 359-387, 1982.

[9] H. Aref, N. Rott, H. Thomann, 'Gröbli's solution of the 3 vortex problem: A case study of graduate work in the 1870's', Ann. Rev. Fluid Mech. 24, 1992

[10] H. Aref, '3 vortex motion with zero total circulation- addendum', J. App. Math. Phys. (ZAMP) 40, 495-500, 1989.

[11] V.I. Arnold, B.A. Khesin, **Topological Methods in Hydrodynamics**, Springer-Verlag, AMS 125, 1998.

[12] A.A. Bagrets, D.A. Bagrets, 'Nonintegrability of two problems in vortex dynamics', Chaos, Vol 7., No. 9, 1997.

[13] J. Bjerknes, J. Holmboe, 'On the theory of cyclones', J. Meteorol., 1, 1944, pp. 1 - 22.

[14] V.A. Bogomolov, 'Dynamics of vorticity at a sphere'. Fluid Dynamics. No. 6, 863-870. 1977.

[15] V.A. Bogomolov, 'Two dimensional fluid dynamics on a sphere'. Izv. Atmos. Oc. Phys., Vol. 15, No. 1, 18-22, 1979.

[16] V.A. Bogomolov,'On the motion of a vortex on a rotating sphere'. Izv. Atmos. Oc. Phys., Vol. 21, No. 4, 298-302, 1985.

[17] G.F. Carnevale, R.C. Kloosterziel, 'Emergence and evolution of triangular vortices'. J. Fluid Mech. 259, 305-331, 1994.

[18] G.F. Carnevale, R.C. Kloosterziel, G.J.F. van Heijst, 'Propagation of barotropic vortices over topography in a rotating tank'. J. Fluid Mech. 233, 119 - 139, 1991.

[19] G.F. Carnevale, G.K. Vallis, R. Purini, M. Briscolini, 'Propagation of barotropic modons over topography', Geophys. Astrophys. Fluid Dyn., 41, 45 - 101, 1988.

[20] J.C.L. Chan, R.T. Williams, 'Analytical and numerical studies of the beta - effect in tropical cyclone motion. Part I : zero mean flow' , J. Atmos. Sci. 44, 1257 - 1265, 1987.

[21] B. Cushman - Roisin. **Introduction to Geophysical Fluid Dynamics.** Prentice Hall, 1994.

[22] U. Dallman, 'Topological structures of three-dimensional vortex flow separation'. AIAA-83-1735, 1983.

[23] M.K. Davey, R.G.A. Hurst, E.R. Johnson, 'Topographic eddies in multi - layer flow'. Dyn. Atmos. Oceans 18, 1 - 27, 1993.

[24] P.J. Davis, **The Schwarz Function and its Applications**, Math. Ass. of America, Washington, 1974.

[25] M.T. DiBattista, L.M. Polvani, 'Barotropic vortex pairs on a rotating sphere' , J.Fluid Mech. 358, 107-133, 1998.

[26] D.G. Dritschel, 'Contour dynamics/surgery on the sphere', J. Comp. Phys. 79, 477-483, 1988.

[27] D.G. Dritschel, L.M. Polvani, 'The roll-up of vorticity strips on the surface of a sphere', J. Fluid Mech. 234, 47-69, 1992.

[28] D.G. Dritschel, 'Vortex properties of 2-D turbulence' , Phys. Fluids A 5(4), 984 - 997, 1993.

[29] D.G. Dritschel, N.J. Zabusky, 'On the nature of vortex interactions and models in unforced nearly inviscid two-dimensional turbulence' , Phys. Fluids A 8(5), 1252-1256, 1996.

[30] D.G. Dritschel. ' The stability and energetics of co-rotating uniform vortices'. J. Fluid Mech. 157, 95-134, 1985.

[31] B. Eckhardt,'Integrable four vortex motion', Phys. Fluids, A 31, 2796-2801. 1988.

[32] E. Firing, R.C. Beardsley, 'The behavior of a barotropic eddy on a beta - plane'. J. Phys. Oceanog. 6, 57-65, 1976.

[33] G.R. Flierl, 'On the instability of geostrophic vortices', J. Fluid Mech. 197, 349-388, 1988.

[34] G.R. Flierl, ' The application of linear quasi - geostrophic dynamics to Gulf - Stream rings', J. Phys. Oceanog. 7, 365-379, 1977.

[35] G.R. Flierl, 'Isolated eddy models in geophysics'. Ann. Rev. Fluid Mech. 19, 493-530, 1987.

[36] A.T. Fomenko, T.Z. Nguyen, 'Topological classification of integrable non-degenerate Hamiltonians on isoenergy three- dimensionanl spheres', in **Advances in Soviet Math. Vol. 6**, ed. A.T. Fomenko, 267-296, American Mathematical Society, Providence, 1991.

[37] A.T. Fomenko, 'Topological classification of all integrable Hamiltonian differential equations of general type with two degrees of freedom', in **The Geometry of Hamiltonian Systems**, ed. T. Ratiu, MSRI Publications. Vol. 22, 131-340, 1991, Springer-Verlag, New York.

[38] S. Friedlander, 'Interaction of vortices in a fluid on the surface of a rotating sphere', Tellus, XXVII, 15-24, 1975.

[39] R.W. Ghrist, P.J. Holmes, M.C. Sullivan, **Knots and Links in Three-Dimensional Flows**, Springer Lecture Notes in Mathematics, Vol. 1654, Springer-Verlag, New York, 1997.

[40] A.E. Gill, **Atmosphere-Ocean Dynamics**, International Geophysics Series, Volume 30, Academic Press, New York, 1982.

[41] R.W. Griffiths, E.J. Hopfinger, 'Experiments with baroclinic vortex pairs in a rotating fluid', J. Fluid Mech. 173, 501-518, 1986.

[42] R.H.J. Grimshaw, D. Broutman, X. He, P. Sun, 'Analytical and numerical study of a barotropic eddy on a topographic slope' , J. Phys. Oceanog. 24, 1587-1607, 1994.

[43] W. Gröbli, 'Specielle probleme über die bewegung geradliniger paralleler wirbelfäden', Zürich: Zürich und Furrer, 1877.

[44] V.M.Gryanik, 'Dynamics of singular geostrophic vortices in a two - level model of the atmosphere (or ocean)', Isv. Atmos. and Oceanic Phys., Vol 19, no 3, 1983.

[45] D. Hally, 'Stability of streets of vortices on surfaces of revolution with a reflection symmetry', J. Math. Phys. 21, 211-217, 1980.

[46] E.J. Hopfinger, F.K. Browand, Y.Gagne, 'Turbulence and waves in a rotating tank', J. Fluid Mech. 125, 505-534, 1982.

[47] E.J. Hopfinger, G.J.F. van Heijst, 'Vortices in rotating fluids', Ann. Rev. Fluid Mech. 25, 241-289, 1993.

[48] N.G. Hogg and H.M. Stommel , 'The heton, an elementary interaction between discrete baroclinic geostrophic vortices, and its implications concerning heat flow', Proc. R. Soc. London Ser. A 397, 1 - 20, 1985.

[49] M. Jamaloodeen, P.K. Newton, Private Communication.

[50] A. Kasahara, G.W. Platzman, 'Interaction of a hurricane with the steering flow and its effect upon the hurricane trajectory', Tellus 15, 321-325, 1963.

[51] J.B. Keller, 'The scope of the image method', Commn. in Pure App. Math., Vol. VI, 505-512, 1953.

[52] Y. Kimura, H.Okamoto, 'Vortex motion on a sphere', J. Phys. Soc. Japan, Vol. 56, No.12, 4203-4206, 1987.

[53] R.C. Kloosterziel, G.J.F. van Heijst, 'An experimental study of unstable barotropic vortices in a rotating fluid', J. Fluid Mech. 223, 1-24, 1991.

[54] K.V. Klyatskin, G.M. Reznik, 'Point vortices on a rotating sphere', Oceanology, Vol. 29, No. 1, 12-16, 1989.

[55] G.K. Korotaev, A.B. Fedotov, 'Dynamics of an isolated barotropic vortex on a beta - plane', J. Fluid Mech. 264, 277-301, 1994.

[56] I.A. Kunin, F. Hussain, X. Zhou, 'Dynamics of a pair of vortices in a rectangle', Int. J. Engng Sci., Vol. 32, No. 11, 1835-1844, 1994.

[57] B. Legras, P. Santangelo, R. Benzi, 'High - resolution numerical experiments for forced 2-D turbulence', Europhys. Lett. 5, 37 - 42, 1988.

[58] C. Marchioro, M. Pulvirenti, **Mathematical Theory of Incompressible Nonviscous Fluids**, App. Math. Sci. 96, Springer-Verlag, 1994.

[59] P.S. Marcus, 'Jupiter's Great Red Spot and other vortices', Ann. Rev. Astron. Astrophys. 31, 523-573, 1993.

[60] J.E. Marsden, T.S. Ratiu, **Introduction to Mechanics and Symmetry**, TAM 17, Springer 1994.

[61] A. Masuda. K. Marubayashi, M. Ishibashi. 'A laboratory experiment and numerical simulation of an isolated barotropic eddy in a basin with topographic β'. J. Fluid Mech. 213, 641-655. 1989.

[62] T.Maxworthy, L.G. Redekopp, 'A solitary wave theory of the Great Red Spot and other observed features of the Jovian atmosphere', Icarus 29, 261-271.

[63] J.C. McWilliams, 'The emergence of isolated coherent structures in turbulent flow'. J. Fluid Mech. 146, 21-43, 1984.

[64] E. Meiburg, P.K. Newton, N. Raju. G. Ruetsch, 'Unsteady models for the nonlinear evolution of the mixing layer', Phys. Rev. E. Vol. 52. No. 2, Aug. 1995.

[65] MODE Group, ' The Mid - Ocean Dynamics Experiment', Deep-sea Res. 25, 859-910, 1978.

[66] H.K. Moffatt, 'The degree of knottedness of tangled vortex lines', J. Fluid Mech., Vol. 35, part 1, 117-129, 1969.

[67] G.K. Morikawa and E. Swenson, 'Interacting motion of rectilinear geostrophic vortices', Phys. Fluids 14(6), 1058-1073, 1971.

[68] T. Needham, **Visual Complex Analysis**, Clarendon Press. 1997.

[69] E.C. Neven, 'Modons in shear flow on a sphere'. Geophys. Astrophys. Fluid Dyn. 74, 51-71, 1994.

[70] E.C. Neven, 'Baroclinic modons on a sphere'. J. Atmos. Sci. 51, 1447-1464. 1994.

[71] E.C. Neven, 'Quadrupole modons on a sphere', Geophys. Astrophys. Fluid Dyn. 65, 105-126, 1992.

[72] D. Nof, 'Modons and monopoles in a γ - plane', Geophys. Astrophys. Fluid Dyn., 52(3), 171-188, 1990.

[73] E.A. Novikov, 'Dynamics and statistics of a system of vortices', Sov. Phys. JETP, 41, 937-943, 1975.

[74] E.A. Novikov, Y. Sedov, 'Stochastization of vortices', JETP Lett. 29, 677-679, 1979.

[75] E.A. Novikov,Y. Sedov, 'Vortex collapse', Sov. Phys. JETP, 50, 297-301, 1979.

[76] J. Nycander, G.G. Sutyrin, 'Steadily translating anticyclones on the β - plane', Dyn. Atmos. Oceans 16, 473-498, 1992.

[77] K.A. O'Neal, 'Stationary configurations of point vortices', Trans. AMS, Vol. 302, No. 2, Aug. 1987.

[78] E.A. Overman, N.J. Zabusky, 'Evolution and merger of isolated vortex structures' . Phys. Fluids 25. 1297-1305. 1982.

[79] S. Pekarsky, J. Marsden. 'Point vortices on a sphere: stability of relative equilibria'. J. Math. Phys. 39, 5894-5907. 1998.

[80] L. Perko, **Differential Equations and Dynamical Systems**, TAM 7, Springer-Verlag, 2nd Ed., 1996.

[81] A.E. Perry, M.S. Chong. 'A description of eddying motions and flow patterns using critical point concepts'. Ann. Rev. Fluid Mech. 19, 125-155. 1987.

[82] L.M. Polvani, D.G. Dritschel, 'Wave and vortex dynamics on the surface of a sphere'. J. Fluid Mech. 255, 35-64, 1993.

[83] L.M. Polvani, X.J. Carton. 'The tripole : a new coherent vortex structure of incompressible two - dimensional flow', Geophys. Astrophys. Fl. Dyn., 51, 87 - 102, 1989.

[84] G.M. Reznik, 'Dynamics of singular vortices on a beta - plane', J. Fluid Mech 240. 405-432, 1992.

[85] G.M. Reznik, W.K. Dewar, 'An analytical theory of distributed axisymmetric barotropic vortices on the *beta* - plane', J. Fluid Mech. 269, 301-321, 1994.

[86] C.G. Rossby, ' On displacements and intensity changes of atmospheric vortices'. J. Mar. Res. 7, 175-187, 1948.

[87] N. Rott,'Three vortex motion with zero total circulation', J. Appl. Math. Phys. (ZAMP), 40, 473-494, 1989.

[88] N. Rott,'Constrained 3 and 4 vortex problems', Phys. Fluids A2, 1477-1480, 1990.

[89] P.G. Saffman, **Vortex Dynamics**, Cambridge University Press, 1992.

[90] A.S. Schwarz, **Topology for Physicists**, Springer- Verlag, 1994.

[91] L.J. Shapiro, 'Hurricane vortex motion and evolution in a three layer model' , J. Atmos. Sci. 49, 140-153, 1992.

[92] L.J. Shapiro, K.V. Ooyama, 'Barotropic vortex evolution on a beta - plane', J. Atmos. Sci. 47, 170-187, 1990.

[93] Special focus issue, 'Large long - lived coherent structures out of chaos in planetary atmospheres and oceans', Chaos 4, 1994.

[94] R.K. Smith, W. Ulrich, 'An analytical theory of tropical cyclone motion using a barotropic model', J. Atmos. Sci. 47, 1973-1986, 1990.

[95] S.G.L. Smith, 'Vortices and Rossby - wave radiation on the beta - plane', Ph.D. Thesis, Univ. of Cambridge, July 1996.

[96] M. Stern, ' Minimal properties of planetary eddies', J. Mar. Res. 33, 1-13, 1975.

[97] G.G. Sutyrin, ' The beta - effect and the evolution of a localised vortex' , Sov. Phys. Dokl. 32 791-793, 1987.

[98] J.L. Synge, 'On the motion of three vortices', Can. J. Math. 1, 257-270, 1949.

[99] V. Szebehely, **Theory of Orbits**, Academic Press, New York, 1967.

[100] J.J. Tribbia, 'Modons in spherical geometry', Geophys. Astrophys. Fluid Dyn. 30, 131-168, 1984.

[101] J. Tzavantzis, L. Ting, 'The dynamics of 3 vortices revisited', Phys. Fluids 31(6), 1392-1409, 1988.

[102] G.J.F. van Heijst, R.C. Kloosterziel, C.W.M. Williams, 'Laboratory experiments on the tripolar vortex in a rotating fluid' , J. Fluid Mech. 225, 301-331, 1991.

[103] W.T.M. Verkley, 'The construction of barotropic modons on a sphere', J. Atmos. Sci. 41, 2492-2504, 1984.

[104] J.-I. Yano, G.R. Flierl, 'Isolated potential vorticity patches in quasi - geostrophic zonal shear flows', Dyn. Atmos. Oceans 16, 439-472, 1992.

[105] W.R. Young, ' Some interactions between small numbers of baroclinic, geostrophic vortices', Geophys. Astrophys. Fluid Dyn., 33, 35-61, 1985.

[106] N.J. Zabusky, J.C. McWilliams, 'A modulated point vortex model for geostrophic, beta - plane dynamics' , Phys. Fluids 25 , 2175-2182, 1982.

[107] L. Zannetti, P. Franzese, 'Advection by a point vortex in closed domains', Eur. J. Mech. B, 12, 43-67, 1993.

IMAGE EVALUATION TEST TARGET (QA-3)

150mm

6″

APPLIED IMAGE . Inc
1653 East Main Street
Rochester, NY 14609 USA
Phone: 716/482-0300
Fax: 716/288-5989